University of São Paulo
Institute of Astronomy, Geophysics and Atmospheric Sciences
Department of Geophysics

Lúcio Quadros de Souza

Ambient Noise and Earthquake Surface Wave Phase Velocity Tomography of the South American Lithosphere

São Paulo

2024

Lúcio Quadros de Souza

Ambient Noise and Earthquake Surface Wave Phase Velocity Tomography of the South American Lithosphere

Thesis to be presented at the Institute of Astronomy, Geophysics and Atmospheric Sciences of the University of São Paulo as a partial requirement for obtaining the title of Doctor of Sciences.

Area of concentration: Geophysics

Advisor: Prof. Dr. Marcelo Assumpção

São Paulo

2024

Acknowledgments

This study was financed by the *Coordenação de Aperfeiçoamento de Pessoal de Nível Superior* (CAPES) - Brazil by the grants from the *Programa de Excelência Acadêmica* (PROEX - 88887.464480/2019-00), *Programa Institucional de Internacionalização* (PrInt - 88887.694554/2022-00 - supervisor: Prof. Dr. Thomas Meier) and *Fundação de Apoio à Universidade de São Paulo* (FUSP project n° 3930). I would like to thank the Kiel University Computing Center[1] for supporting this study through high-performance computing resources.

I would also like to thank the extensive help provided both personally and professionally by Prof. Dr. Marcelo Assumpção, Prof. Dr. Thomas Meier, Prof. Dr. Amr El-Sharkawy, Felix Eckel, Dr. Lars Wiesenberg, Maté Timkó and Prof. Dr. Marcelo Bianchi without whom this work would not be possible.

[1] https://www.hiperf.rz.uni-kiel.de/caucluster/

Abstract

Rayleigh-wave phase velocities are automatically determined using earthquake records of 1,022 stations throughout South America, Antarctica and the Caribbean between 1990 and 2020 for 10,799 earthquakes resulting in 19,522 interstation measurements. Isotropic and anisotropic phase-velocity maps are presented for periods between 5 and 200 s. For depths between 0 and 300 km, the isotropic components were used to calculate a 3-D shear-wave velocity model for the continent based on a stochastic particle-swarm-optimization inversion technique. We also obtain a Moho map for South America that shows good agreement with the most recent crustal thickness map. Azimuthal anisotropy is observed in areas of previously poor coverage by SKS studies within the South American Platform, including the Amazonian Basin, Amazonian Craton, and Pantanal Basin. For periods above 60 s, we observed a NE-SW oriented fast direction of azimuthal anisotropy in the regions of the Pantanal and Chaco-Paraná sedimentary basins. This trend coincides with a low-velocity zone (-4% V_{SV} at 100 km) observed in this and other studies interpreted as thinned lithosphere. This result suggests that mantle flow is channeled by the lithospheric topography in this area. At crustal depths, beneath the Andes, azimuthal anisotropy is oriented parallel to the strike of the orogeny, which is consistent with the observed compression of the South American Plate from the subduction of the Nazca Slab. We also observe a systematic difference between the Guyana and Brazilian Shields at lithospheric depths. Our model shows that, on average, shear-wave velocities are approximately 3% lower in the Guyana Shield than in the Brazilian Shield which may result from a lithospheric reworking in the Central Atlantic Magmatic Province. Finally, thin crust and lithosphere is observed in the Tocantins Province in Brazil in accordance with previous seismic refraction and receiver function studies that might explain the high seismicity observed in this area.

Ambient noise dispersion curves were calculated similarly to the earthquake methodology. We used 138 seismic stations from 1998 to 2022 from the Brazilian Seismographic Net-

work and additional temporary deployments to compute 1,477 ambient noise phase-velocity dispersion curves. Rayleigh-wave isotropic and anisotropic maps, between periods of 2 and 200 s, were calculated by combining dispersion curves from the earthquake dataset with ambient noise. For the isotropic phase velocities, the results show good agreement with previous tomographies in the crust. At 2 s, higher phase velocities are observed to the west of the Pantanal Basin relative to the east. This result agrees with a joint inversion of Receiver Function, surface waves and H/V data and indicates that the basin's basement is shallower in the west. For the azimuthal anisotropies and crustal depths (5 to 20 s), we observed a NE-SW fast axis trend to the north of the Pantanal Basin and NW-SE to the south of it, well correlated with the Paraguay fold belt strike under the basin. At the same depths, N-S fast axis anisotropies were observed mainly inside the Paraná Basin and those could be associated with the collision of the Paranapanema, Rio Apa and Amazonian Cratons during the assemblage of west Gondwana during the Neoproterozoic as mentioned by a previous study. Fast axis anisotropies parallel to the passive margin in Mantiqueira Province were observed and correlated well with a Pms splitting study in this area. This result helps confirm the interpretation that crustal and lithospheric anisotropy in the Ribeira belt is due mainly to shear deformation during the Brasiliano orogeny.

Resumo

As velocidades de fase das ondas *Rayleigh* foram determinadas automaticamente utilizando registros de terremotos de 1.022 estações sismográficas em toda a América do Sul, Antártica e Caribe entre 1990 e 2020 para 10.799 terremotos, resultando em 19.522 curvas de dispersão. Mapas de velocidade de fase da componente isotrópica e anisotrópica são apresentados para períodos entre 5 e 200 s. Para profundidades entre 0 e 300 km, as componentes isotrópicas foram utilizadas para calcular um modelo 3D de velocidade da onda de cisalhamento para o continente, com base em uma técnica de inversão estocástica de otimização por enxame de partículas. Também obtivemos um mapa de espessura da Moho para a América do Sul, que mostra boa concordância com o mapa de espessura crustal mais recente para a região. Anisotropia azimutal foi observada em áreas com pouca cobertura em estudos anteriores de SKS na Plataforma Sul-Americana, incluindo a Bacia do Amazonas, Cráton Amazônico e Bacia do Pantanal. Para períodos acima de 60 s, observamos a direção rápida de anisotropia azimutal orientada NE-SO nas regiões das bacias sedimentares do Pantanal e Chaco-Paraná. Essa tendência coincide com uma zona de baixa velocidade (-4% V_{SV} a 100 km) observada neste e em outros estudos, interpretada como uma região de afinamento da litosfera. Este resultado sugere que o fluxo do manto é direcionado pela topografia litosférica nesta área. Em profundidades crustais nos Andes, a anisotropia azimutal é orientada paralelamente ao *strike* da orogenia, o que é consistente com a compressão observada da Placa Sul-Americana pela subducção da Placa de Nazca. Também observamos uma diferença sistemática entre os escudos da Guiana e do Brasil em profundidades litosféricas. Nosso modelo mostra que, em média, as velocidades das ondas de cisalhamento são aproximadamente 3% mais baixas no Escudo da Guiana do que no Escudo Brasileiro, o que pode resultar de um retrabalho da litosfera cratonica na região Província Magmática do Atlântico Central. Finalmente, observou-se baixa espessura crustal e litosférica na Província Tocantins, no Brasil, de acordo com estudos anteriores de refração sísmica e função do receptor, o que pode explicar a alta sismicidade observada nesta área.

Curvas de dispersão de ruído ambiental foram calculadas de forma semelhante à metodologia dos terremotos. Utilizamos 138 estações sismográficas de 1998 a 2022 da Rede Sismográfica Brasileira e instalações temporárias para calcular 1.477 curvas de dispersão de velocidade de fase da onda *Rayleigh*. Mapas isotrópicos e anisotrópicos de ondas Rayleigh, para períodos entre 2 e 200 s, foram calculados combinando as curvas de dispersão do conjunto de dados de terremotos com o ruído ambiental. Para as velocidades de fase isotrópicas, os resultados mostram boa concordância com tomografias anteriores na crosta. Em 2 s, anomalias altas de velocidade de fase são observadas a oeste da Bacia do Pantanal em relação ao leste. Este resultado concorda com uma inversão conjunta de Função do Receptor, ondas de superfície e dados H/V e indica que o embasamento da bacia é mais raso no Oeste. Para as anisotropias azimutais e profundidades crustais (5 a 20 segundos), observamos uma tendência NE-SO da direção rápida da anisotropia ao norte da Bacia do Pantanal e NO-SE ao sul dela, bem correlacionada com o *strike* do cinturão do Paraguai sob a bacia. Nas mesmas profundidades, a direção rápida N-S das anisotropias foram observadas principalmente dentro da Bacia do Paraná, o que pode estar associado à colisão dos crátons Paranapanema, Rio Apa e Amazônico durante que colidiram durante a formação do Gondwana Ocidental no Neoproterozoico, conforme mencionado por um estudo anterior. Direções rápidas de anisotropias paralelas à margem passiva na Província Mantiqueira foram observadas e bem correlacionadas com um estudo de *Pms splitting* nesta área. Este resultado ajuda a confirmar a interpretação de que a anisotropia crustal e litosférica na Faixa Ribeira é devido a principalmente deformações de cisalhamento devido a Orogênese Brasiliana.

Contents

List of Figures

List of Tables

1 Introduction

1.1 Thesis overview

This thesis contains phase-velocity and shear-wave velocity tomographies using Rayleigh-wave dispersion data from earthquakes..This first work was produced in cooperation with Prof. Dr. Thomas Meier and his group from the University of Kiel in Germany. The work was submitted to *Geophysical Journal International* on July 4th, 2024. A copy of the submitted paper is available in Appendix B (Sec. 11). The sections from 1.2 to 6 cover the same study but provide more details, especially concerning the methodology and parameterization of the inversions. This thesis also includes a second study regarding the use of ambient noise data together with the earthquake dataset from the first work to improve the characterization of the seismic phase velocities and azimuthal anisotropy determination in the crust of SSE Brazil. The sections from 7 to 8 cover this topic.

1.2 Geological framework

The South American Lithosphere can be divided into three main units: 1) The South American Platform (Almeida et al. 2000), a mostly stable region since Phanerozoic times that was not affected by the Andean and Caribbean orogenesis; 2) The Andean Phanerozoic Orogeny; and 3) The Patagonian microcontinent. The South American Platform is bounded west by the Andean Phanerozoic Orogeny, south by the Patagonian block, east by the Atlantic Ocean and north by the Caribbean (Fig. 1). The South American Platform is divided into cratonic blocks Archean and Proterozoic ages (blue text in Fig. 1) that are connected by Neoproterozoic mobile belts (green text in Fig. 1). Several Precambrian orogenic events were responsible for the formation of the lithosphere that ranged from 2.2 Ga to 0.5 Ga (Cordani and Sato 1999) through a series of episodes of agglutinations with posterior fragmentation (Almeida et al. 2000). The South American Platform can be divided into an Amazonian and an Atlantic domain based on their distinct tectonic evolution (Almeida et al. 1981): 1) Amazonian domain contains, more importantly, the Amazonian craton, whose origin is related to the paleocontinent Laurentia; 2) Atlantic domain whose origin is related to the western region of the Gondwana supercontinent and it contains the cratons of São Francisco, Paranapanema and Rio de la Plata. All the mentioned cratons have outcrops on the surface (blue and red lines are cratons and sedimentary basins in Fig. 1, respectively), except the Paranapanema craton (blue dashed line in Fig. 1) that is supposed to be underneath the Paraná Basin (Affonso et al. 2021; Mantovani et al. 2005; Ciardelli et al. 2022; Celli et al. 2020). Those domains are roughly divided by a 2,700 km continental-scale megashear zone called Transbrasiliano Lineament (Cordani and Sato 1999; Cordani et al. 2013) or TBL (purple dashed line in Fig. 1). A series of Phanerozoic intracratonic basins (red text in Fig. 1) covers most of the cratonic units of the platform.

A Mesozoic reactivation associated with the fragmentation of the Pangea Supercontinent (Deckart et al. 2005) and opening of the Atlantic Ocean (O'Connor and Duncan 1990) caused magmatism to occur throughout the South American Platform: 1) Central Atlantic Magmatic Province (CAMP) with its emplacement happening around 200 Ma (Deckart et al. 2005; Marzoli et al. 2018) with extensive basalt flooding in Amazon basin and NW-SE and NE-SW orientation dykes in the eastern and northern areas of the Guyana Shield (Deckart et al. 2005; Knight et al. 2004); 2) Paraná-Etendeka Large Igneous Province, with a major magmatism peak between 137-120 Ma, produced extensive basalt flooding affecting mostly the Paraná basin (Turner et al. 1994; Renne et al. 1996; Thiede and Vasconcelos 2010).

1.3 Previous works

1.3.1 Overview

At the end of the 20th century, regional tomographic studies observed lateral variations in the seismic velocities of the South American Lithosphere. The group-velocity tomography

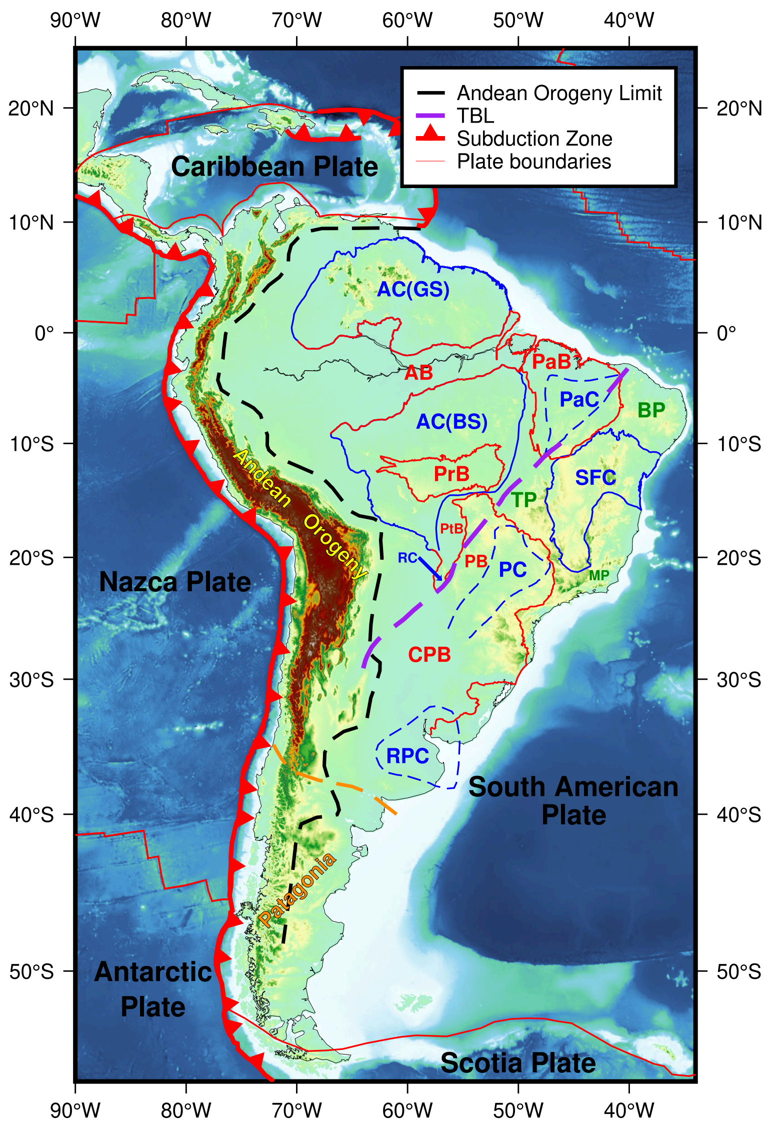

Fig. 1: Major tectonic units for South America. Plate boundaries are shown as a red lines while dented lines are for subductions (Hasterok et al. 2022). Blue outline are craton limits (dashed for cratonic blocks buried beneath sedimentary basins) and red are limits of sedimentary basins (Almeida et al. 1981; Cingolani and Salda 2000). Labels are blue for cratons, red for Phanerozoic sedimentary basins and green for Neoproterozoic orogenic belts. AC = Amazon Craton, composed of the Guyana Shield (GS) and Central Brazil Shield (BS), SFC = São Francisco Craton, RC = Rio Apa Craton, PaC = Parnaíba Cratonic block inferred from deep seismic reflection profiles (e.g. Daly et al. 2014), PC = Paranapanema Cratonic block inferred from gravity data (Mantovani et al. 2005) and the RPC = Rio de La Plata Craton. Fold belt provinces: Tocantins (TP), Borborema (BP) and Mantiqueira (MP). Phanerozoic sedimentary basins: Amazonian (AB), Parnaíba (PaB), Parecis (PrB), Pantanal (PtB), Paraná (PB) and Chaco-Paraná (CPB). The dashed purple line denotes the transcontinental Transbrasiliano Lineament, or TBL (Cordani et al. 2016). The black dashed line is the limit between the Andean orogenic belt (Cordani et al. 2016) and the stable platform (Almeida et al. 2000). Orange dashed line is the limit of the Patagonia Paleozoic terrain (Ramos 2008).

from Vdovin et al. (1999) observed strong lateral heterogeneity within the South American Lithosphere. They observed low-velocity anomalies associated with the presence of sediments in the Paraná and Chaco-Paraná basins, variations in crustal thickness in the Andes and the Brazilian Highlands and the cratonic roots of the Amazon and São Francisco cratons. A surface-wave inversion using phase velocity with Receiver Function and P-wave regional travel-time data constraints by Snoke and James (1997) showed considerable upper mantle low S velocity (around 4.2 km/s) and shallow Moho (32 km depth) under Chaco-Paraná basin, increasing to about 4.3 km/s at 150 km depth. Snoke and James (1997) also observed a high S velocity anomaly (around 4.6-4.7 km/s) beneath Paraná basin until about 200 km depth associated with cratonic lithosphere. The teleseismic travel-time inversion of VanDecar et al. (1995) imagined a fossil plume in the upper mantle beneath Paraná basin. A cylindrical and 300 km across anomaly was associated with low P ($\sim$-0.8%) and S ($\sim$-1.2%) velocity anomalies going vertically from 200- to 600 km. VanDecar et al. (1995) interpreted this anomaly primarily as a fossil conduit by which the Tristan da Cunha plume head traveled to cause the Paraná-Etendeka flood basalts.

The P and S travel-time inversion of Schimmel et al. (2003) confirmed the observation of the fossil upper mantle plume beneath Paraná basin as previously observed by VanDecar et al. (1995). They also observed high P and S wave velocities beneath the southern tip of the São Francisco craton at 200 to 250 km depth associated with its cratonic root.

The S velocity inversion in the upper mantle from Lee et al. (2001) imaged a highly heterogeneous upper mantle of the South American Lithosphere. A high-velocity lithosphere (about +3 to +4% S velocity at 100 km) was observed in the western region of Guyana and Brazil shields, indicating that both shields are underlain by cratonic lithosphere. Moreover, the model shows a high-velocity lithosphere under Amazon basin despite the Mesozoic rifting in the region (Cordani and Bruto Neves 1982). Low-velocity anomalies (around -3% S velocity at 100 km) were observed beneath the Pantanal, Chaco-Paraná and Paraná basins. Strong low-velocity anomalies (around -7% S velocity anomaly at 100 km) were observed along the

Andes associated with the mantle wedge in the region. However, the poor distribution of sources and stations limited the resolved anomalies to the west and central South American Lithosphere.

Feng et al. (2004) produced a group-velocity inversion for South America using Rayleigh and Love waves. Feng et al. (2004) also used the regionalized dispersion curves to invert a lithospheric S-velocity model. Down to 150 km, high-velocity anomalies were found beneath the Amazon and São Francisco cratons. In the Amazon craton at 150 km, the high-velocity anomalies were found more prominently in its eastern region, indicating that the lithosphere would be thicker. This is consistent with the hypothesis that the Amazon craton could be formed by crustal accretion during different orogenic cycles (Santos et al. 2000; Santos et al. 2006), where the oldest units are to the east. This result was consistently observed in other studies as well (e.g. Feng et al. 2004; Feng et al. 2007; Heit et al. 2007; Ciardelli et al. 2022; Celli et al. 2020; Nascimento et al. 2022; Nascimento et al. 2024). The authors observed a correlation between the trend of the TBL with a low-velocity zone alongside it in upper mantle depths.

The Rayleigh-wave waveform inversion from Heit et al. (2007) for South America produced an Sv velocity model that observed, at 100 km, that the high velocity in the Amazon craton was separated in two parts associated with the Brazil and Guyana shields, suggesting that the Mesozoic rifting was responsible for the formation of the Amazon basin. They observed a high-velocity anomaly (around +7-8% Sv velocity) down to 200 km depth inside the Paraná basin that was associated with a cratonic lithosphere. Below 200 km beneath the Paraná basin, a low-velocity anomaly (around -3-4% Sv velocity) was observed in the region of the Ponta Grossa arc. This low-velocity anomaly was interpreted as a fossil plume located 900 km south of the low-velocity anomaly from VanDecar et al. (1995) and Schimmel et al. (2003). This observation led Heit et al. (2007) to conclude that both anomalies could be related to the Tristan da Cunha plume and, most likely, different diachronous plumes hit the base of the lithosphere in the Paraná basin region.

The joint inversion of waveforms and Rayleigh-wave group velocities by Feng et al. (2007) also observed a reduction in the high-velocity anomalies beneath the Amazon basin at depths around 100 to 150 km, similar to Heit et al. (2007). Feng et al. (2007) also reproduced the observation from their previous work (Feng et al. 2004) of a low-velocity belt along the TBL at 100 to 200 km depth.

Rocha et al. (2011) inverted tomographic maps of SE and Central Brazil using P and S-wave travel times from teleseismic earthquakes. At lithospheric depths, the authors also observed P and S-wave high-velocity anomalies (e.g. around +0.3% for P and around +0.9% for S at 150 km) beneath Paraná basin that was associated with a cratonic lithosphere in the region. In the Paraná basin, between 300 to 700 km depth, a strong low-velocity anomaly (-0.4% for P and -1.5% for S at 350 km) was associated with the fossil mantle plume observed previously by VanDecar et al. (1995) and Schimmel et al. (2003).

The waveform inversion of Celli et al. (2020) computed shear-wave velocity maps to image the South American and African Lithospheres. In South America, high Vs anomalies were observed beneath Paranapanema craton and Parnaíba basins. They did not observe a high-velocity anomaly beneath the Rio de la Plata craton. Between the Amazon and São Francisco cratons, a low-velocity anomaly (around -2% Vs) was observed corresponding roughly to the TBL at 260 km, similar to previous works (Feng et al. 2004; Feng et al. 2007; Rocha et al. 2016). At 260 km, a low-velocity anomaly (around -1.5% Vs) was also observed in the Guyana shield's western region, explaining the high topography of the Guyana Highlands.

The Adjoint Waveform Tomography of Ciardelli et al. (2022) was used to compute a shear-wave velocity model for the South American Lithosphere. Ciardelli et al. (2022) did not observe a high-velocity anomaly beneath the Rio de la Plata craton. This result is in agreement with previous tomographic models (Feng et al. 2007; Schaeffer and Lebedev 2013; Celli et al. 2020) with exception of the recent surface-wave inversion by Nascimento et al. (2024) that detected a high shear-wave velocity anomaly (around 4.7 km/s Vs at 150 km) roughly towards NW of the Rio de la Plata craton surface limits (Fig. 1). The highly resistive anomaly (around 2,000 Ωm) observed from the magnetotelluric study by Bologna et al. (2019) would indicate the existence of a cratonic keel.

Ciardelli et al. (2022) also computed a Lithosphere-Asthenosphere Boundary (LAB) map that showed thick lithosphere beneath eastern Brazil Shield (around 160 km thick) and thinner LAB (around 100 km) beneath Pantanal and Chaco-Paraná basins. This area of thin lithosphere also coincides with a low-velocity zone for P and S velocity found in several studies (e.g. Ciardelli et al. 2022; Nascimento et al. 2022; Celli et al. 2020; Rocha et al. 2019; Lee et al. 2001; Feng et al. 2004; Moura et al. 2024; Nascimento et al. 2024). Ciardelli et al. (2022) high-velocity anomalies (around +6% Vs) along the Paranapanema craton that were consistent with the gravimetric signature from Mantovani et al. (2005), consistent with positive P-wave anomalies (around +1% Vp) for the Paranapanema craton from 100 to 300 km depth (Affonso et al. 2021; Rocha et al. 2011) and the waveform inversion from Celli et al. (2020).

At crustal depths, we observe low shear-wave velocity (around 3.4 to 3.7 km/s Vs) in the areas of sedimentary basins from both surface-wave studies (e.g. Feng et al. 2004; Nascimento et al. 2022; Nascimento et al. 2024; Moura et al. 2024) and ambient noise (Shirzad et al. 2020), except for the Pantanal basin, that has a very thin (500 m) sedimentary layer (Catto 1975; Weyler 1962).

1.3.2 Anisotropy

The anisotropy of South America is mostly regionally studied using Shear Wave Splitting, SWS (e.g. Melo et al. 2018; Assumpcao et al. 2011; Heintz et al. 2003; Assumpção et al. 2006; Russo and Silver 1994; James and Assumpção 1996; Polet et al. 2000; Krüger et al. 2002; Anderson et al. 2004; Piñero-Feliciangeli and Kendall 2008; Growdon et al. 2009; Masy et al. 2009; Poveda et al. 2023), geodynamic models (Hu et al. 2017), azimuthal anisotropy (Poveda et al. 2023; Shirzad et al. 2024) and *Pms* splitting analysis (Feng et al. 2024). For the asthenospheric upper mantle, the anisotropy is thought to be primarily attributed to subduction-induced mantle flow (Hu et al. 2017) or to have some additional contribution from it being deflected by the cratonic roots (Melo et al. 2018; Assumpcao et al. 2011; Assumpção et al. 2006). The Amazon and Paranapanema cratons were observed to cause this deflection in SWS studies (Melo et al. 2018; Assumpcao et al. 2011; Assumpção et al. 2006). In the South American Platform, those studies are usually limited to the southeastern region of the continent and along the Andes.

Shirzad et al. (2024) computed azimuthal anisotropy for the crust and upper mantle using Ambient Noise data between 4 and 70 s for SE Brazil. At short periods (e.g. 8 s), Shirzad et al. (2024) found that the anisotropies fast directions are parallel to the fold belt deformation. At longer periods (e.g. 70 s), Shirzad et al. (2024) found N-S fast direction anisotropy that was associated with compressional deformation of the lithospheric lid and it is consistent with the same N-S fast direction from the global model of Debayle et al. (2016). Shirzad et al. (2024) infer that this deformation could result from of the final Neoproterozoic collision between the Amazon, Rio Apa and Paranapanema cratons.

The *Pms* splitting study by Feng et al. (2024) resolved crustal anisotropies for the South American Platform with splitting times varying from 0 to 0.5 s. Feng et al. (2024) observed roughly NNE-SSW fast polarization directions approximately parallel to the strike of the TBL. Because the anisotropy orientation is inconsistent with present-day stress fields (Heidbach et al. 2016), Feng et al. (2024) conclude that the anisotropy orientation is more likely to be related to crustal deformation during the formation of the TBL. Weak anisotropies (around 0.1 s) parallel to the passive continental margin were observed in the east and northeast, implying a fossil extensional deformation from the rifting of West Gondwana during the Mesozoic. Strong and roughly WSW-ENE anisotropies fast direction were found in the Paraná basin that the authors interpreted as being associated with mantle anisotropy from SKS studies (e.g. Melo et al. 2018; Assumpcao et al. 2011; Assumpção et al. 2006). This would indicate a coupled crust-mantle deformation during the breakup of west Gondwana.

2 Interstation Measurement Method and Data

2.1 Overview

Studying the South American Lithosphere seismic structure has always been challenging, given the sparse station coverage, especially in the stable platform. Methods such as SWS are especially affected by the lack of station coverage. However, two-station methods (e.g. Meier et al. 2004; Kästle et al. 2016; Soomro et al. 2016) can be used to provide accurate surface-wave dispersion data that can be used to derive isotropic and anisotropic anomalies along the whole ray path between a pair of stations. Two-station measurements have an advantage over single-station measurements by not being affected by source mechanism and localization errors (e.g. Muyzert and Snieder 1996; Levshin et al. 1999). Beyond that, the bandwidth for Rayleigh-wave two-station measurements is generally broader than single-station, especially for high frequencies (Lebedev et al. 2006). For the previously mentioned earthquake-based surface-wave studies in the South American Platform (Feng et al. 2004; Rosa et al. 2016; Lee et al. 2001; Heintz et al. 2005; Feng et al. 2007; Nascimento et al. 2022; Nascimento et al. 2024), all of them use single-station measurements. We used the two-station method to compute a simultaneous inversion for isotropic and anisotropic anomalies using Rayleigh-wave phase velocities in South America.

2.2 Phase-velocity curve measurement

The two-station method (e.g. Meier et al. 2004; Kästle et al. 2016; Soomro et al. 2016) is a way to measure surface-wave group and phase velocities using earthquakes closely aligned with a pair of stations. The phase velocity can be derived from the phase term of the cross-correlation function between the earthquake waveforms recorded on each station. Fig. 2 gives a general idea of this procedure for the 7.9 Mw Cantwell Alaska Earthquake.

As explained by Soomro et al. 2016, the cross-correlation has the advantage of being

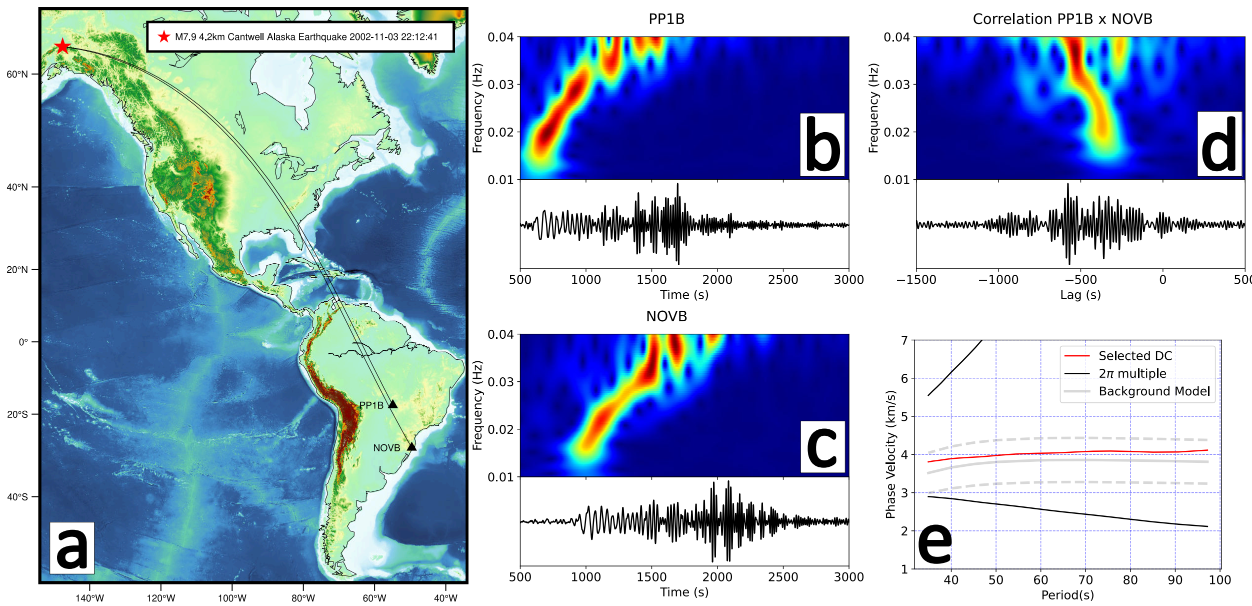

Fig. 2: Example of the two-station method measurement for the 7.9 Mw Cantwell Alaska Earthquake. a) The maps show the event's location and selected receivers for two stations inside Brazil (PP1B and NOVB). The curves show the great circle path connecting the event and each station. b) and c) 2-hour-long seismograms and frequency-time diagrams for PP1B and NOVB stations. d) cross-correlation function and respective frequency-time representation; and e) computed Rayleigh-wave phase-velocity dispersion curve from the cross-correlation function. 2π multiples are shown in black. The background model used to select the correct multiple is shown as a gray line with an associated 15% threshold (dashed gray line). The final selected dispersion curve is shown as a red line..

less affected by uncorrelated noise and the contribution of the fundamental mode is enhanced by the product of the amplitude spectra. We can understand the signal components of the Fourier transform of a time series, $u(t)$, as

$$U(\omega) = U_0(\omega) + \sum_j U_j(\omega) + N(\omega) \tag{1}$$

where $U_0(\omega)$ is the fundamental mode, $\sum_j U_j(\omega)$ are the higher modes and $N(\omega)$ is the noise. To accurately calculate phase velocities, it is necessary to isolate the fundamental mode contribution in Eq. 1.

To extract the fundamental mode, a frequency-time analysis is applied (Levshin et al. 1989; Kulesh et al. 2005; Laske et al. 2011), where the higher modes and noise signals are filtered out. A cleaned frequency-time representation of time series $u(t)$ would contain only the contribution of the fundamental mode and some noise as follows $u_\omega(\omega_n, t) \approx u_0(\omega_n, t) + n(\omega_n, t)$. For this step, we used the implementation by Soomro et al. 2016 where Gaussian filters are applied according to

$$F(\omega, \omega_n) = exp\left(-\alpha_f\left(\frac{\omega}{\omega_n} - 1\right)^2\right) \tag{2}$$

where the width of the Gaussian filter is $\alpha_f = \gamma_f^2 \omega_n \Delta t$ is chosen to optimize the frequency-time resolution with γ_f being an empirical parameter usually between 12 and 20 (we chose 16 following Soomro et al. 2016). Δt is the sampling interval in the time domain.

Second, the fundamental mode signal can be enhanced by applying a down-weighting time window to reduce higher modes and noise signals (Meier et al. 2004). Again, we used the implementation by Soomro et al. 2016, where Gaussian windows $w(t)$ are applied in the time domain as follows

$$w(t) = exp\left(\frac{-\omega_n^2 (t - t_{max})^2}{4\alpha_\omega}\right) \tag{3}$$

where t_{max} is the time of maximum amplitude of the cross-correlation and the width of the Gaussian window is implemented similarly to the previous step as $\alpha_\omega = \gamma_\omega^2 \omega_n \Delta t$. Soomro et al. 2016 note that because the dispersion is stronger for longer interstation paths, the empirical parameter γ_ω must increase linearly. We varied γ_ω between 20 and 70 for interstation distances between 400 and 3000 km, respectively.

Based on Soomro et al. 2016 notation, if the cleaned frequency-time spectra representations for stations 1 and 2 are $U_{\omega 1}(\omega_n)$ and $U_{\omega 2}(\omega_n)$, respectively. The average phase velocity, $c(\omega_n)$, can be calculated by taking the phase $\phi(\omega_n)$ from the ratio between $U_{\omega 1}(\omega_n)$ and $U_{\omega 2}(\omega_n)$

$$\frac{U_{\omega 1}(\omega_n)}{U_{\omega 2}(\omega_n)} = \frac{|U_{\omega 1}(\omega_n)|}{|U_{\omega 2}(\omega_n)|} exp(i\phi(\omega_n)) \tag{4}$$

where

$$\phi(\omega_n) = \phi_1(\omega_n) - \phi_2(\omega_n) \approx k(\omega_n)(\Delta_2 - \Delta_1) \tag{5}$$

and

$$c(\omega_n) \approx \frac{\omega_n(\Delta_2 - \Delta_1)}{\phi(\omega_n) + 2n\pi} \tag{6}$$

where $\phi_1(\omega_n)$ and $\phi_2(\omega_n)$ are the fundamental mode phase spectra for stations 1 and 2, while Δ_1 and Δ_2 are the epicentral distances for the stations. Soomro et al. (2016) point out that the use of epicentral distances instead of interstation distances is important because interstation distances can induce bias if the event is slightly off the great-circle path. The phase difference $\phi(\omega_n)$ (Eq. 5) can be approximated by taking the phase from a filtered and weighted cross-correlation function:

$$\phi_{CCF} \approx \phi_1(\omega_n) - \phi_2(\omega_n) \tag{7}$$

An example of this procedure can be seen in Fig. 2. Fig. 2b and c show the 2-hour long record of the vertical component of two stations and their respective frequency-time representation. The high amplitude shown in this figure is the Rayleigh wave fundamental mode and it can be seen clearly until about 0.04 Hz. For higher frequencies (>0.03 Hz), we observe very high contamination of the fundamental mode that is probably related to crustal heterogeneities along the propagation path. The cross-correlation (Fig. 2d) reduces this contamination strongly. The extracted phase-velocities multiples can be seen in Fig. 2e, where is necessary to compare it to a background model (gray dashed line) as a way to pick the correct branch. The acceptable dispersion curve segment (red line) is selected based on its proximity to the background model.

2.3 Selection of phase-velocity curves

To select realistic 1-D phase-velocity curves, we follow the automatic selection procedure from Soomro et al. (2016). The authors point out that due to the fundamental mode depth sensitivity kernels having a very broad range of depth and changing very gradually with frequency, any realistic 1-D earth dispersion curve should be smooth. Based on that premise, their model aims to select or reject parts of an observed dispersion curve based on roughness criteria.

The first criterion is the background model. In order to select the correct 2π multiple and its segments with reasonable phase-velocity values, a proximity measurement between the observed dispersion curve and background model is done as follows:

$$\left|\frac{c(\omega_i) - c_0(\omega_i)}{c_0(\omega_i)}\right| \times 100 < th_{\Delta C} \tag{8}$$

where $c(\omega_i)$ is the observed dispersion curve, $c_0(\omega_i)$ is the background model and $th_{\Delta C}$ is the maximum difference allowed, in percent (we used 15%).

The second criterion is smoothness. The curve roughness is quantified by taking the first derivative of the phase velocity with respect to frequency, $c'(\omega)$, and comparing it with the equivalent roughness of the background model, $c_0'(\omega)$, and it is calculated as

$$S(\omega_i) = \sum_{\omega_j=\omega_i-d(\omega_i)}^{\omega_j+d(\omega_i)} \left| \frac{c'(\omega_j) - c_0'(\omega_j)}{c_0(\omega_j)} \right| < th_S \tag{9}$$

where th_S is a constant empirical threshold usually defined as 150 s (Soomro et al. 2016), we kept the same value for our study. The authors perform the summation in Eq. 9 over a moving window of increasing length as a function of frequency, $2d(\omega_i)$, as a way to implement a frequency-independent threshold.

Finally, the last criterion is length. Usually, very short segments are determined with less confidence and of little use. Therefore, to avoid that the authors implement a criterion where the length of a segment must be greater than a frequency-dependent threshold, $th_{\Delta\omega}$, described below:

$$th_{\Delta\omega} = max\{a \times log(\omega_m) + b, min(threshold\, value)\} \tag{10}$$

where ω_m is the central frequency of the segment. The values we determined empirically are $a = 0.0035$, $b = 0.023$ and the $min(threshold\, value) = 1/200\, Hz$.

An example of applying those selection steps is shown in Fig. 3. Fig.3A the multi-colored phase-velocity curve is the selected 2π branch (thin black lines) based on proximity to the background model (gray solid line). Additionally, the blue segment of the accepted curve is rejected because it exceeds the maximum deviation thresholds (dashed gray lines). Some samples before the violating segment are removed to account for finite resolution in the frequency domain. The green segment violates the smoothness criterion (Fig. 3B) by exceeding the threshold of 150 s. Lastly, the yellow segment violates the length criterion by being smaller (the yellow circle shows segment size) than the minimum value allowed for its central frequency (dashed gray line). The red segment is accepted.

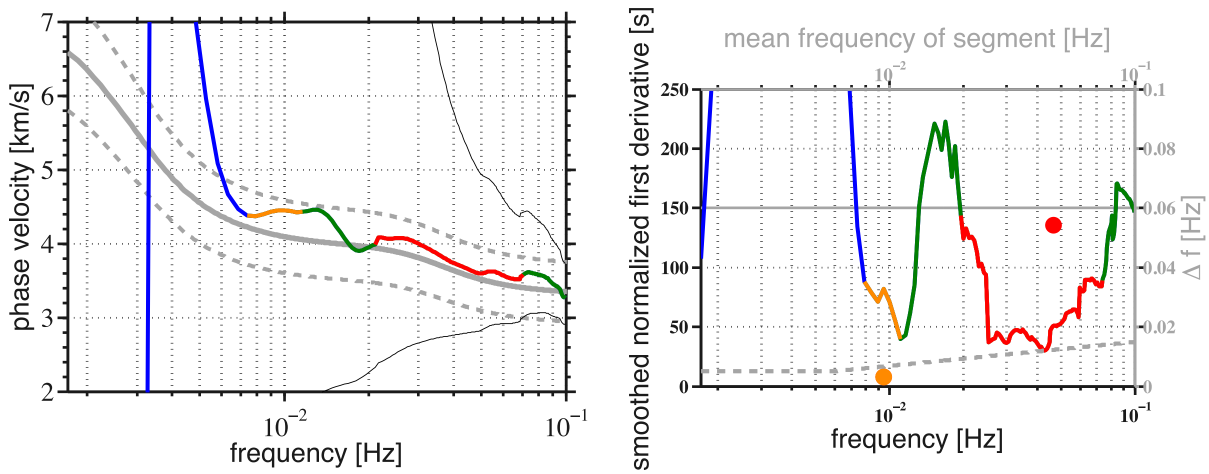

(a) Background model criterion

(b) Smoothness and length criterion

Fig. 3: Example of the automated selection criteria by Soomro et al. 2016. A) Background model criterion: The gray solid line is the background model with dashed lines around it representing the maximum deviation thresholds (15%). The thinner black lines are the multiples (2π ambiguity). The multi-colored line in A represents the selected branch by background model criterion. B) The left and black y-axis is the smoothness criterion (with a threshold of 150 s), while the right and gray y-axis is the length criterion threshold (defined by the gray dashed line). The multi-colored curve in B is a smoothness curve, while the dots represent the length of the same colored segments. Taking all criteria into consideration, the blue segment is rejected because it violates the background model criterion, the green segment is rejected because it violates the smoothness criterion by being over 150 s in B and the yellow segment is rejected because it violates the length criterion (yellow circle below the gray dashed line). The only accepted segment is the red curve. Figure from Soomro et al. 2016.

2.4 Averaging phase-velocity curves

Because the phase-velocity curve calculated for each event for a pair of stations can have some variability, especially for different propagation directions (Fig. 4b). It is necessary to apply further quality control before taking the final average. We followed Soomro et al. 2016 implementation:

1. outlier rejection (we rejected 15% of the outermost values);
2. a minimum number of measurements are required for each frequency (we used 5);
3. a mean phase-velocity curve and the standard deviation are calculated for each direction ($std1$, $std2$), if the difference between those two directions is over a certain threshold, th_{std}, the measurement is rejected. This threshold is defined as $th_{std} = 5 \times max(std1, std2)$;
4. the standard deviation of all measurements should be lower than 3%;
5. the length criterion of section 2.3 is applied again;
6. averaging of all phase-velocity curves for each interstation path.

Fig. 4 shows an example of this procedure for a pair of stations IPMB and JANB in Brazil. Fig. 4a shows all the calculated dispersion curves for each propagation path (gray and black lines), where it is clear that there are inconsistencies between the curves in both directions (Fig. 4b). The dashed blue line in Fig. 4b shows the phase-velocity interval of the dispersion curve (DC) segments that passed the selection criteria. Fig. 4c shows the final average as a solid blue line. After its application, the curves in both directions are highly in agreement.

2.5 Data

We downloaded broadband earthquake records from 1,022 stations in South America, Antarctica and the Caribbean, as seen in Fig. 5, between 1990 and 2020, from the IRIS data

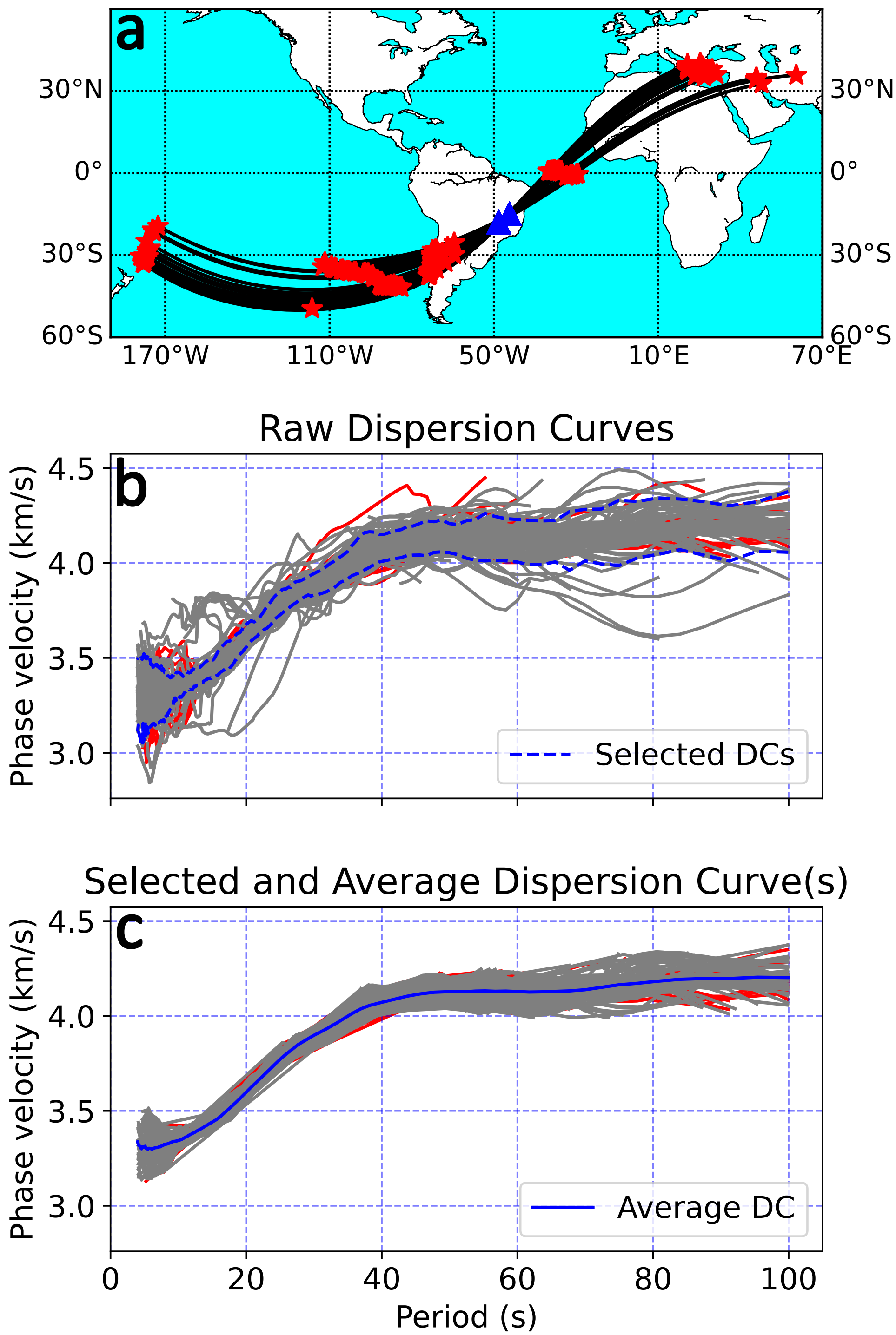

Fig. 4: Averaging of the phase-velocity curves for a pair of stations IPMB and JANB in Brazil. The black and red curves are measurements in opposite propagation directions. The dashed blue line shows the phase-velocity interval of the dispersion curve (DC) segments that passed the selection criteria described in Sec. 2.4. The final phase-velocity dispersion curve average for this path is shown as a blue line.

center and the Brazilian Seismographic Network, RSBR (Bianchi et al. 2018). Table 1 in the Appendix C shows a compilation of all used networks. A total of 10,799 earthquakes were selected based on the following criteria: (1) Events aligned within 10° of the great circle path between a pair of stations; (2) A linearly increasing minimum magnitude between 4 and 6 Mw as a function of the epicentral distance; (3) Epicentral distances between 2.5° and 130°.

Fig. 5 shows our station distribution (a) and the coverage of the 76,038 ray paths (b). The colors indicate the number of events used for each station and interstation path for Fig. 5a and b, respectively. The stations in the Caribbean, Andes and some of the permanent Brazilian seismographic stations provide most of our data.

Following the phase-velocity dispersion curve processes shown in Sec. 2.3, we obtained 19,522 Rayleigh-wave dispersion measurements between 4 and 315 s (around 26% of the initial dataset). Fig. 6 shows a hitcount plot for all the average dispersion curves. Most of our data is below 200 s, which can roughly indicate we can investigate, at most, 300 km depth. We also observe two branches for periods higher than 15 s. The bottom one is related to the high crustal thickness below the Andes and the top one is related to the cratonic areas inside the South American Platform (Fig. 1). The measurements' average standard deviation is approximately 1.5% for all periods (Fig. 8). Fig. 7 shows five examples of average dispersion curves throughout mostly the cratonic area of the South American Platform. Fig. 7a shows the color-coded location of the interstation paths and Fig. 7b shows all the dispersion curves. Fig. 7b shows the Civiero et al. (2024) global average cratonic dispersion curve in gray and a shaded area corresponding to this reference curve ± 0.1 km/s. The shaded area corresponds, roughly, to the distribution of dispersion curves around the mean from Civiero et al. (2024). Our dispersions agree with the reference model, starting to deviate only below 15 s. The dispersion that goes through a non-cratonic area (green curve) shows considerably lower phase velocities between 40 and 110 s. In the same period range, we can also observe a systematic difference between the red and brown curves going through the east and west of the Amazon

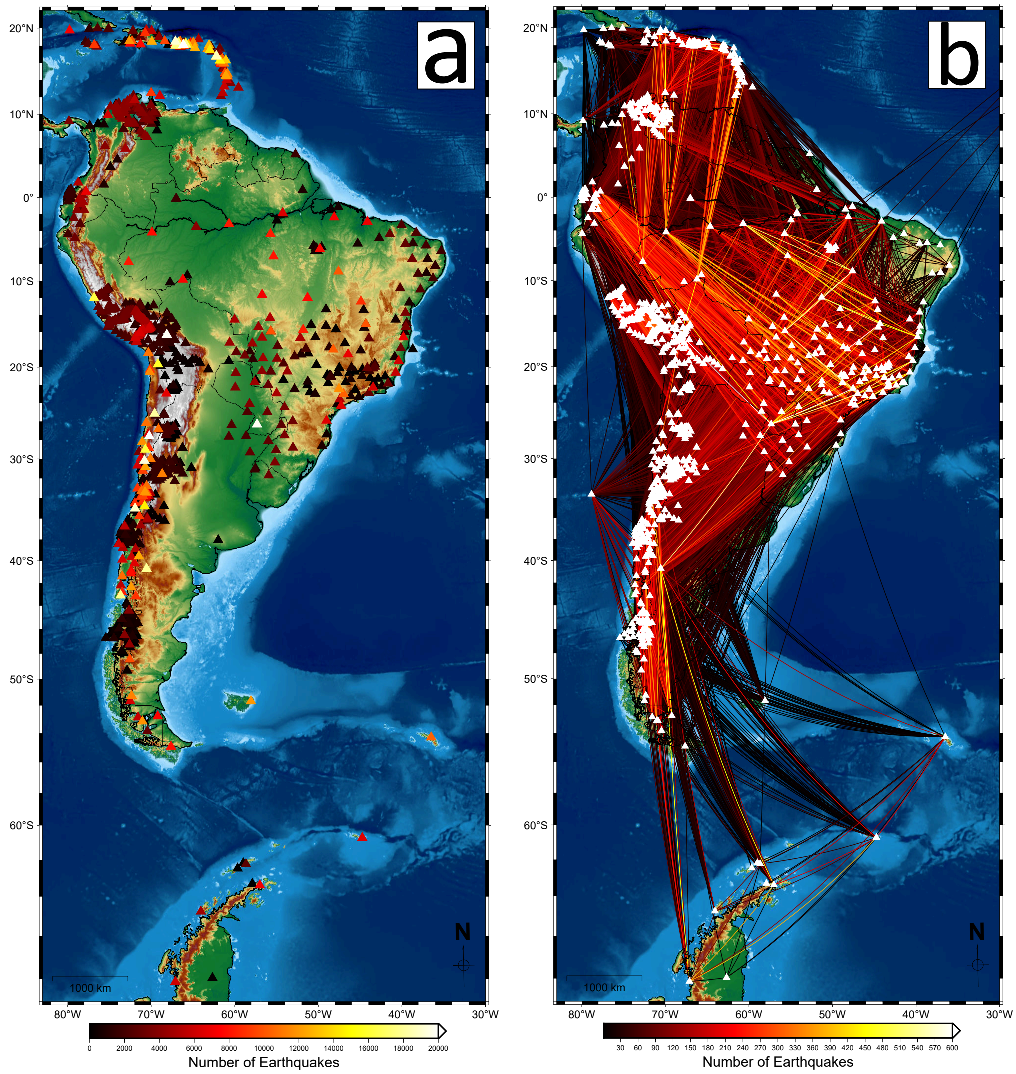

Fig. 5: Color-coded number of earthquake records between 1990 and 2020 used for each station (a) and each station pair along the great-circle path (b). A total of 1,022 stations recorded 10,799 earthquakes distributed over 76,038 interstation paths to calculate Rayleigh-wave phase-velocity maps for South America. The paths going northeastward in (b) are from stations on Madeira Island, Portugal.

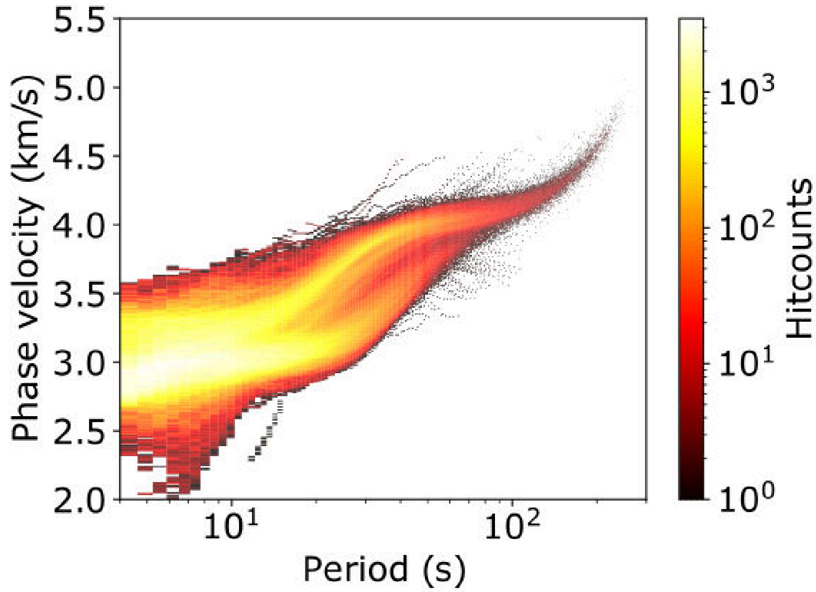

Fig. 6: Hitcount for the final selected dispersion curves. The bottom branch, after 15 s, shows mainly the lower velocities from the Andean thick crust, while the top branch shows higher velocities related to velocities in the upper mantle below the stable continental region.

craton, respectively. The eastern portion of the Amazon craton is the oldest province of the craton (Santos et al. 2000) and several studies identify a high-velocity anomaly in this region (e.g. Feng et al. 2004; Feng et al. 2007; Heit et al. 2007; Ciardelli et al. 2022; Celli et al. 2020; Nascimento et al. 2022).

3 Isotropic and Anisotropic Phase-velocity Inversion

3.1 Theory

We conducted a simultaneous isotropic and anisotropic phase-velocity inversion for Rayleigh waves following the work of Deschamps et al. (2008). We accounted for the 2ψ and 4ψ anisotropic contributions as described by Smith and Dahlen (1973) that show the dependence of Rayleigh and Love waves propagation velocity in an anisotropic medium. The contributions to the phase velocity anomaly, δC, for a latitude θ and longitude φ are as

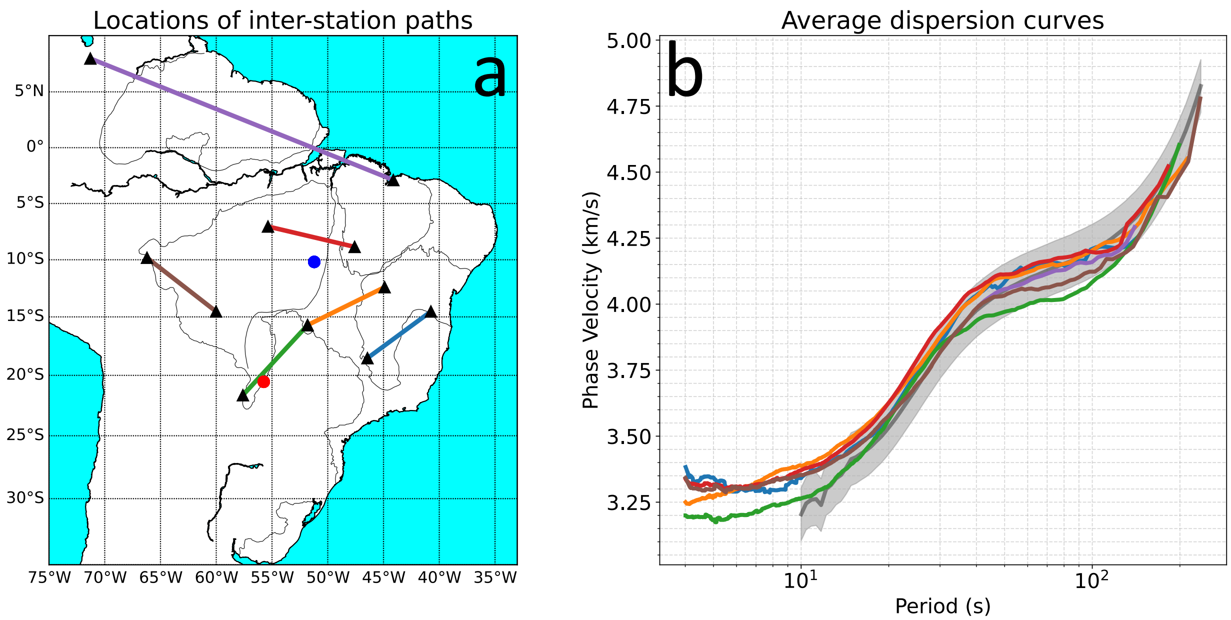

Fig. 7: Example of six average Rayleigh-wave phase-velocity dispersion curves for different tectonic areas. (a) location of each interstation path. The blue and red dots are the locations of shear-wave velocity inversion profiles in Fig. 21 for the Amazonian Craton and Pantanal Basin, respectively. (b) plot of all six dispersion curves. In (b), the global average dispersion for cratons (Civiero et al. 2024) is shown as a dark gray line and the shaded area corresponds to the reference curve $\pm 0.1\,km/s$.

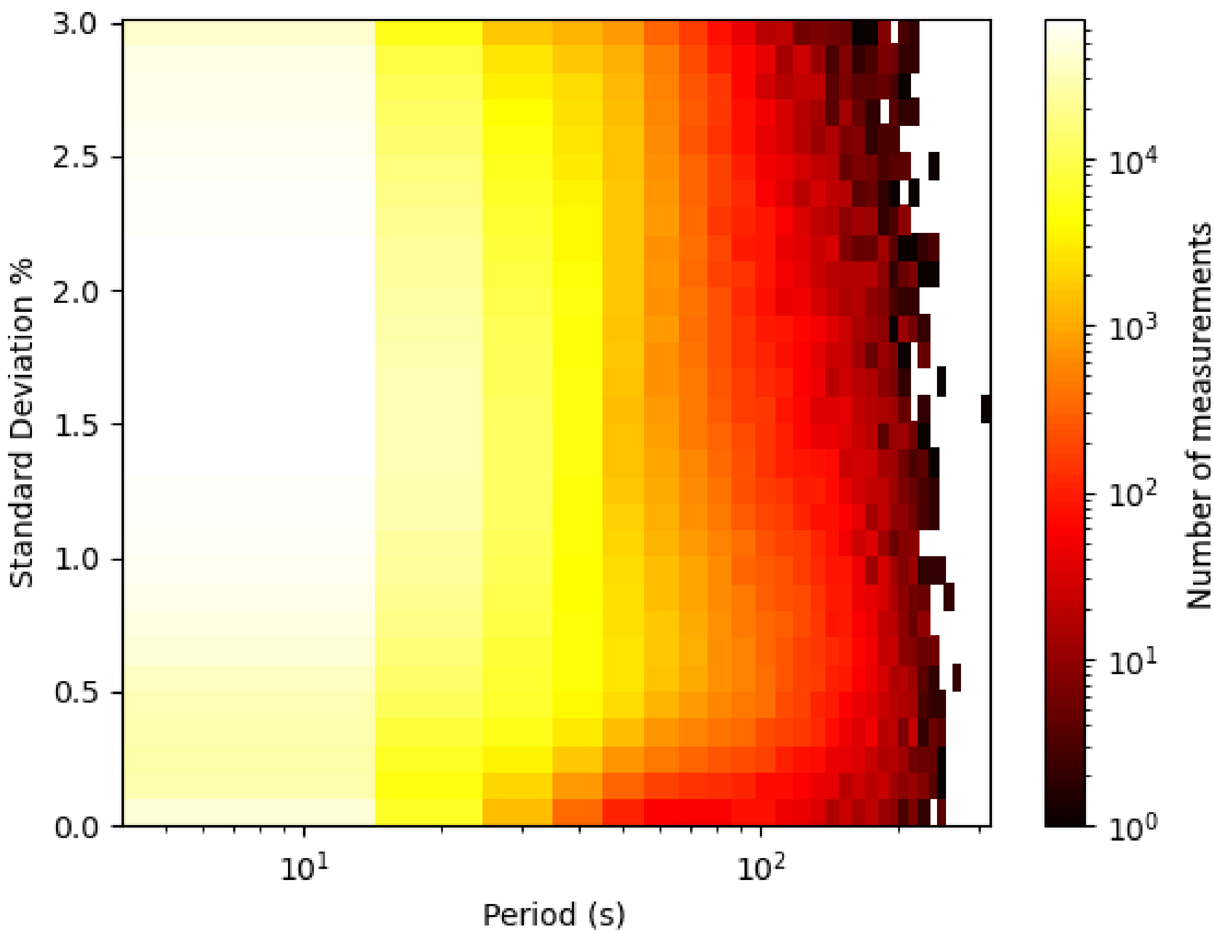

Fig. 8: Hitcount graph for the standard deviation (percentile) as a function of the period (s) for all the observed dispersion curves.

follows using the notation by Deschamps et al. (2008):

$$\delta C(\varphi,\theta) = \delta C_{iso}(\varphi,\theta) + \delta C_{2\psi}(\varphi,\theta) + \delta C_{4\psi}(\varphi,\theta) \tag{11}$$

where $\delta C_{iso}(\varphi,\theta)$ is the isotropic anomaly and $\delta C_{2\psi}(\varphi,\theta)$ and $\delta C_{4\psi}(\varphi,\theta)$ are the 2ψ and 4ψ anisotropic anomalies that are defined as

$$\delta C_{2\psi}(\varphi,\theta) = A_{2\psi}cos(2\psi) + B_{2\psi}sin(2\psi) \tag{12}$$

and

$$\delta C_{4\psi}(\varphi,\theta) = A_{4\psi}cos(4\psi) + B_{4\psi}sin(4\psi) \tag{13}$$

where ψ is the local azimuth of the ray. The four anisotropic coefficients are defined for each θ and φ as $A_{2\psi}$, $B_{2\psi}$, $A_{4\psi}$ and $B_{4\psi}$. The amplitudes of anisotropic anomalies, $\Lambda_{2\psi}$ and $\Lambda_{4\psi}$, are defined as

$$\begin{cases} \Lambda_{2\psi} = \sqrt{A_{2\psi}^2 + B_{2\psi}^2} \\ \Lambda_{4\psi} = \sqrt{A_{4\psi}^2 + B_{4\psi}^2} \end{cases} \tag{14}$$

while the direction of fast propagation, $\Theta_{2\psi}$ and $\Theta_{4\psi}$, are defined as

$$\begin{cases} \Theta_{2\psi} = \frac{1}{2}arctan\left(\frac{B_{2\psi}}{A_{2\psi}}\right) \\ \Theta_{4\psi} = \frac{1}{4}arctan\left(\frac{B_{4\psi}}{A_{4\psi}}\right) \end{cases} \tag{15}$$

Deschamps et al. (2008) method is parameterized on a triangular grid where we used a knot spacing of 30 km. The authors calculate the average phase-velocity anomaly for a certain path i *as*

$$\overline{\delta C_i} = \int_\varphi \int_\theta K_i(\varphi,\theta)\, \delta C(\varphi,\theta)\, d\theta\, d\varphi \tag{16}$$

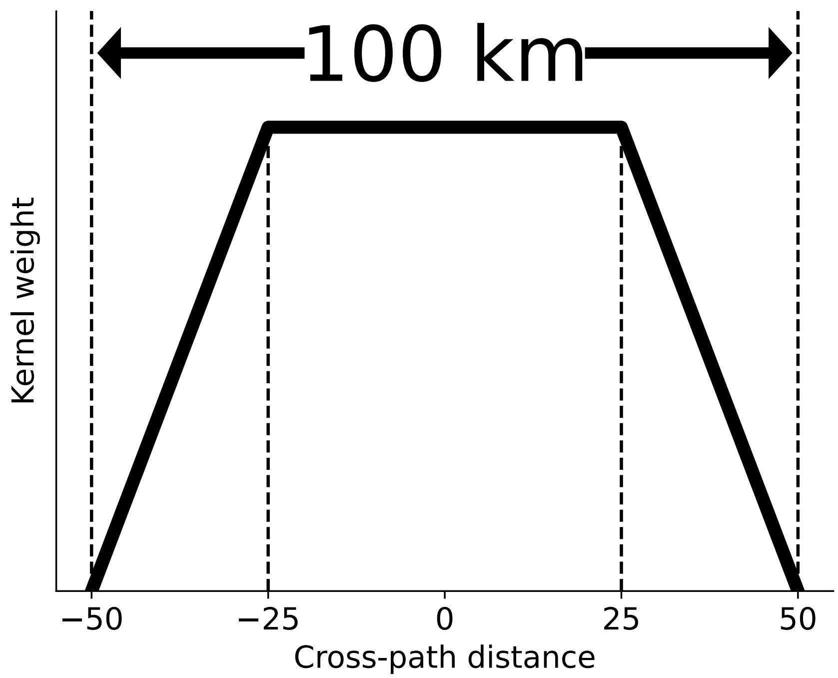

Fig. 9: Cross-section perpendicular to the path i of a sensitivity kernel $K_i(\varphi, \theta)$ (Eq. 11) for a fixed width approximation from Deschamps et al. (2008) used in the isotropic and anisotropic phase-velocity inversion.

where $\delta C(\varphi, \theta)$ is calculated from Eq. 11 and $K_i(\varphi, \theta)$ are the sensitivity kernels and contain the weight of each knot for each path and are approximated by Deschamps et al. (2008) using paths of finite width. Fig. 9 shows an example of a fixed-width kernel approximation. Deschamps et al. (2008) did not observe a significant difference in the obtained solutions for widths between 10 and 300 km. We chose 100 km for our inversion.

For each period, Deschamps et al. (2008) solve the inversion problem by building a discrete system of linear equations for each path:

$$\mathbf{d} = G\mathbf{m} \tag{17}$$

where $\mathbf{d}$ is the data vector containing the dispersion curve Rayleigh-wave average phase-velocities (Sec. 2.4) at a particular period and each path N:

$$\mathbf{d}^T = (\overline{\delta C_1} \cdots \overline{\delta C_N}) \tag{18}$$

The vector $\mathbf{m}$ (Eq. 17) is the model and includes the five terms $\delta C_{iso}(\varphi, \theta)$, $A_{2\psi}$, $B_{2\psi}$, $A_{4\psi}$ and $B_{4\psi}$ for each knot of the grid M:

$$\mathbf{m} = \begin{pmatrix} \delta C_{iso,1} & A_{2\psi,1} & B_{2\psi,1} & A_{4\psi,1} & B_{4\psi,1} \\ \dots & \dots & \dots & \dots & \dots \\ \delta C_{iso,M} & A_{2\psi,M} & B_{2\psi,M} & A_{4\psi,M} & B_{4\psi,M} \end{pmatrix} \tag{19}$$

The generalized matrix is composed of five submatrices:

$$G = (G_{iso} \;\; G_{C2\psi} \;\; G_{S2\psi} \;\; G_{C4\psi} \;\; G_{S4\psi}) \tag{20}$$

where

$$G_{iso} = \begin{pmatrix} K_{1,1} & \dots & K_{1,M} \\ \dots & \dots & \dots \\ K_{N,1} & \dots & K_{N,M} \end{pmatrix} \tag{21}$$

$$G_{C2\psi} = \begin{pmatrix} a_1 K_{1,1} & \dots & a_1 K_{1,M} \\ \dots & \dots & \dots \\ a_N K_{N,1} & \dots & a_N K_{N,M} \end{pmatrix} \tag{22}$$

$$G_{S2\psi} = \begin{pmatrix} b_1 K_{1,1} & \dots & b_1 K_{1,M} \\ \dots & \dots & \dots \\ b_N K_{N,1} & \dots & b_N K_{N,M} \end{pmatrix} \tag{23}$$

$$G_{C4\psi} = \begin{pmatrix} c_1 K_{1,1} & \dots & c_1 K_{1,M} \\ \dots & \dots & \dots \\ c_N K_{N,1} & \dots & c_N K_{N,M} \end{pmatrix} \tag{24}$$

$$G_{S4\psi} = \begin{pmatrix} d_1 K_{1,1} & \dots & d_1 K_{1,M} \\ \dots & \dots & \dots \\ d_N K_{N,1} & \dots & d_N K_{N,M} \end{pmatrix} \tag{25}$$

where $K_{i,j}$ are the weights for each path i and knot j, the azimuthal dependence is defined by the constants $a_i = cos(2\psi_i)$, $b_i = sin(2\psi_i)$, $c_i = cos(4\psi_i)$ and $d_i = sin(4\psi_i)$ with ψ_i being the azimuth for a path i. The authors solved this linear system by following the implementation of the LSQR method (Paige and Saunders 1982).

The isotropic and anisotropic terms are regularized independently by Deschamps et al. (2008) using lateral smoothing and norm damping. The choice of the regularization values is always subjective. We opted to base the regularization of this work roughly on the best regularization values found in El-Sharkawy et al. (2020) Rayleigh-wave phase-velocity model for the Mediterranean region. El-Sharkawy et al. (2020) used the exact same methodology shown for a similar continental-scale study of the lithosphere.

3.2 Checkerboard test

Checkerboard tests were made to verify the resolution of our phase-velocity model using different cell sizes for 30 and 100 s. We used checkers of sizes of 1.5°, 3° and 6° spaced by 2°, 2° and 4°, respectively. The test results are shown in Fig. 10.

For 1.5° and 30 s, the test shows well resolved anomalies in the central part of South America and the central Andes. We also can resolve some anomalies in the Southern Andes (along ~70°W). For 100 s, the coverage for this checker size is slightly worse, where the main well-resolved area is the cratonic area (mainly Brazil) to the east.

For 3° and 30 s, the coverage is largely similar to 1.5°, but we can resolve a larger region overall in the central part of South America. Also, we can further include a portion of the northern Andes (∼5°N ∼73°S) and east of the Caribbean plate. For 100 s, the test shows similar results to the 1.5° checkerboard test.

For 6°, both periods show we can recover anomalies throughout the model for large-scale features. However, we observe a slight attenuation of the recovered amplitudes for checkers north of 0° latitude and south of 30°S.

From those tests, our models have good resolution for most of central South America (mainly Brazil) but cover a larger area in the lower periods (e.g. 30 s) compared to the longer periods (e.g. 100 s). Outside this high-resolution area, we can recover the average tendencies of the medium for large-scale features.

3.3 Rotation test

We applied a two-step procedure to verify the anisotropy component's reliability. First, anisotropies with small amplitudes mostly indicate an isotropic medium. Therefore, they are of no use for the interpretation. We defined a low amplitude threshold, th_A, using the standard deviation of all anisotropy amplitudes, A_{std}, and its mean, A_{mean}, for each period. Then we defined a frequency-independent threshold as $th_A = mean(A_{mean} - A_{std})$ or 7.41 m/s (Fig. 11). Second, for the remaining curves, we applied the 90° rotation test (e.g. Zhang et al. 2009; Endrun et al. 2011; Schaeffer et al. 2016; Wiesenberg et al. 2022). In this test, we rotate the original 2ψ terms 90° while the 4ψ terms are set to zero due to them being much smaller than the 2ψ terms. Then, we remake the inversion with an initial model that combines the rotated anisotropy and the original isotropic component. The directions of the rotated anisotropy and the one retrieved from the test must be within 20° of each other to be considered a robust result. Fig. 12a shows a cropped region of our model in northern Brazil at 30 s. Azimuthal anisotropy fast direction is plotted over the isotropic model as red bars.

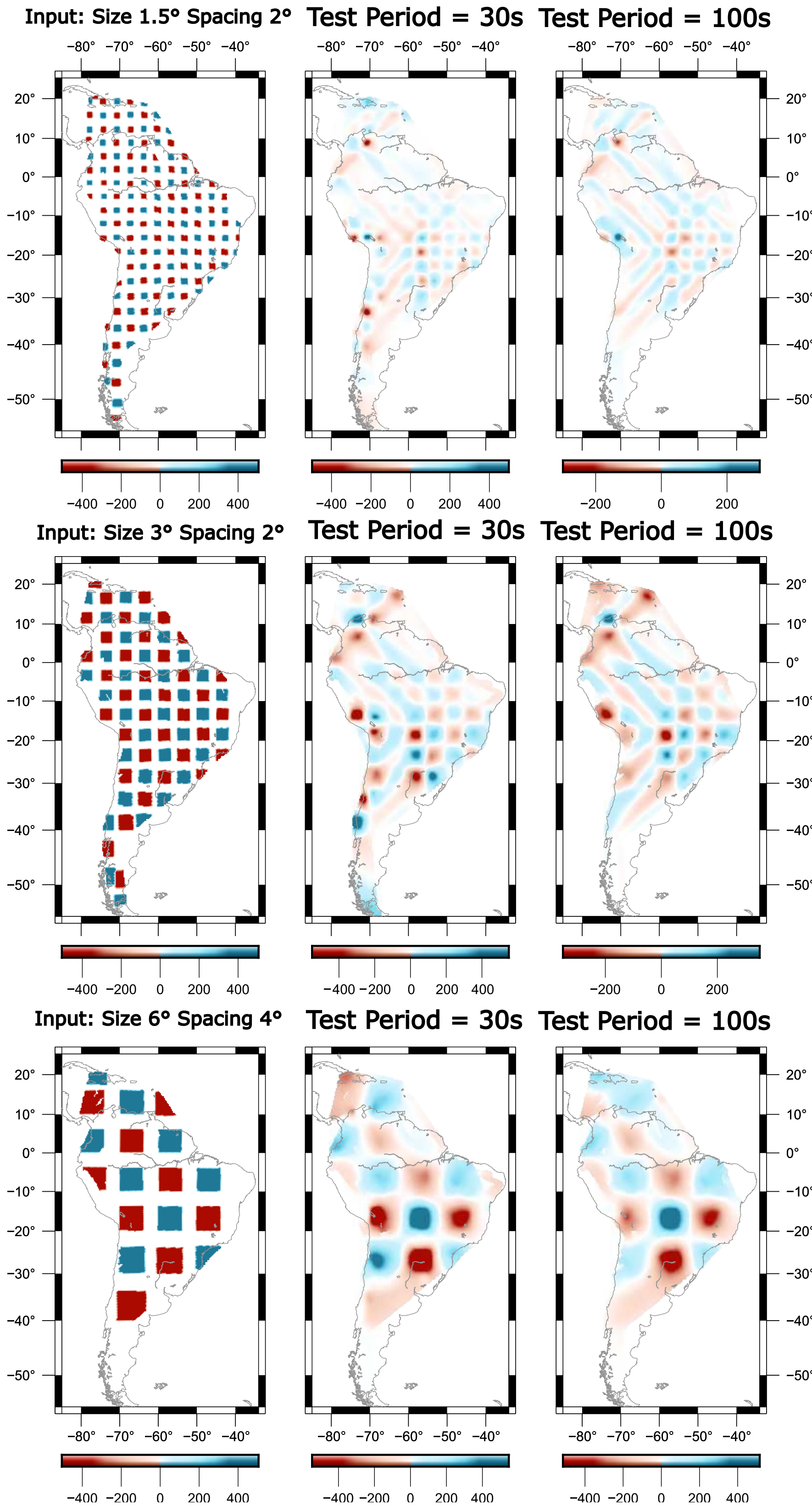

Fig. 10: Checkerboard tests for the isotropic component of the Rayleigh-wave phase-velocity map at 30 and 100 s. We tested checkers with sizes of 1.5°, 3° and 6° spaced by 2°, 2° and 4°, respectively. The anomaly scale is in m/s.

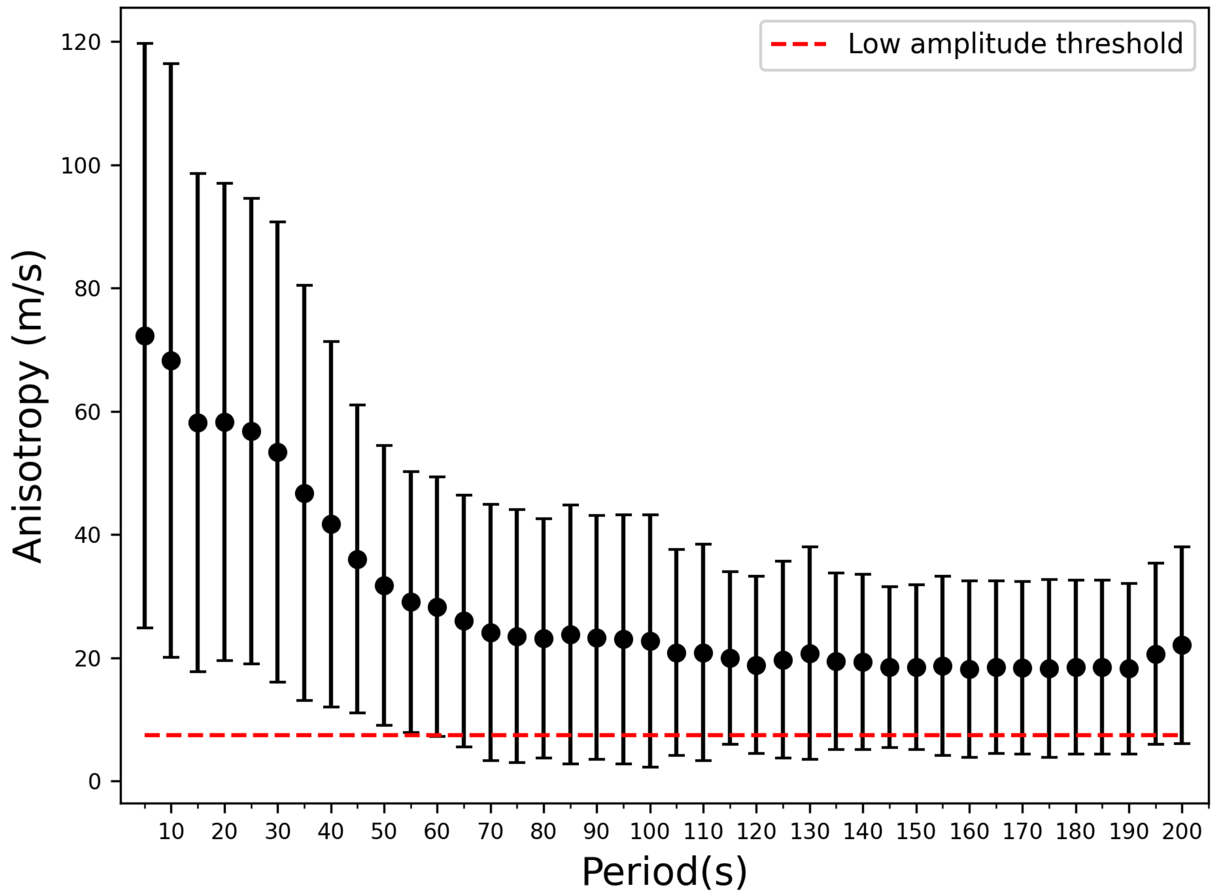

Fig. 11: Anisotropy average amplitude as a function of the period (black circles) with associated standard deviation (black bar). The low amplitude threshold, th_A, was defined as $th_A = mean(A_{mean} - A_{std})$ or the value of 7.41 m/s (dashed red line).

Those original amplitudes are rotated 90° with a fixed amplitude (white bars in Fig. 12b) and the recovered anisotropies after remaking the inversion are shown as black bars in Fig. 12b. Fig. 12c shows the cleaned results, where the nodes with amplitudes smaller than th_A are shown as red circles and the nodes where the direction differences were larger than 20° were removed. Fig. A2 shows further examples of the uncleaned phase-velocity maps for 15, 30, 60 and 100 s.

The final cleaned results can be seen in Fig. 13 for 15, 30, 60 and 100 s. The Guyana shield was the main area where nodes were removed by amplitude and rotation test. Beyond that, some low-amplitude nodes inside Brazil were also removed. The nodes with NE-SW

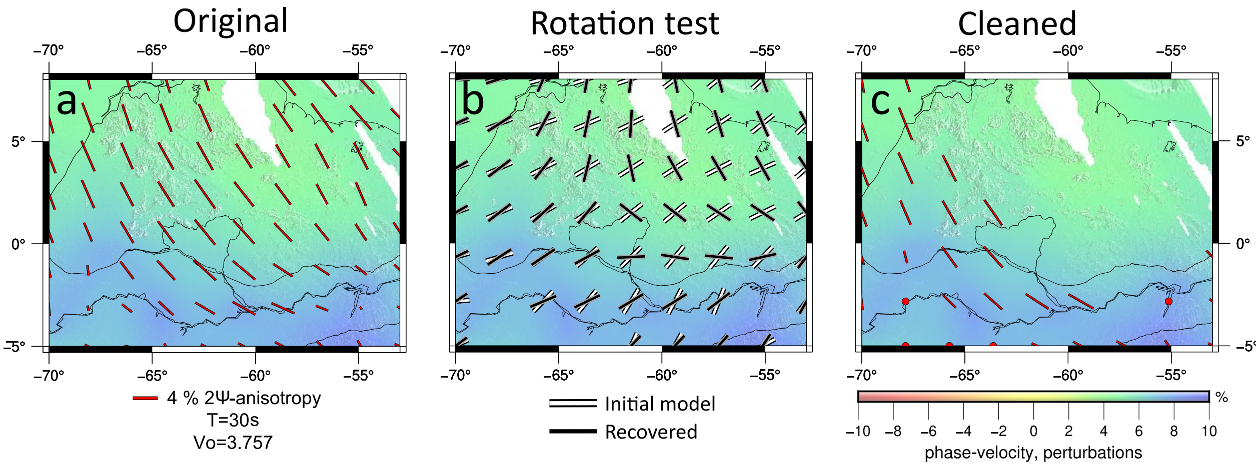

Fig. 12: Rotation test example for the azimuthal anisotropy for the Guyana Shield Craton for 30 s. (a) shows the originally calculated anisotropies as red bars. (b) shows the rotation test in two steps: (1) anisotropies with amplitudes smaller than an empirically defined threshold of 7.41 m/s are removed and (2) the remaining amplitudes are rotated by 90 (white bars) and used as synthetic input for the inversion (e.g. Zhang et al. 2009; Endrun et al. 2011; Schaeffer et al. 2016; Wiesenberg et al. 2022). The white bars are the original anisotropies rotated 90°. The black bars are the anisotropies recovered after the inversion. Measurements were accepted if the initial and recovered anisotropies are within 20° of each other. (c) shows the final cleaned results. The original anisotropies that passed both steps are shown as red bars and anisotropies smaller than the amplitude threshold are plotted as red dots.

orientations below the Pantanal basin and Andean nodes were kept after this test. The Fig. A1, in the appendix, shows the rotation test (equivalent to Fig. 12b) for the whole study area.

4 Local Dispersion Curves

Local phase-velocity dispersion curves were computed from the isotropic component of the inverted phase-velocity maps (Sec. 3) for each grid node. Vos et al. (2013) point out that, hypothetically, in total absence of lateral heterogeneity, the two-station method would produce exact results for a pure great circle path propagation. However, in the presence of the actual Earth 3-D heterogeneity and the finite frequency of the seismic waves, there can be bias in the accuracy of phase velocity measurements. A solution to extracting smooth local

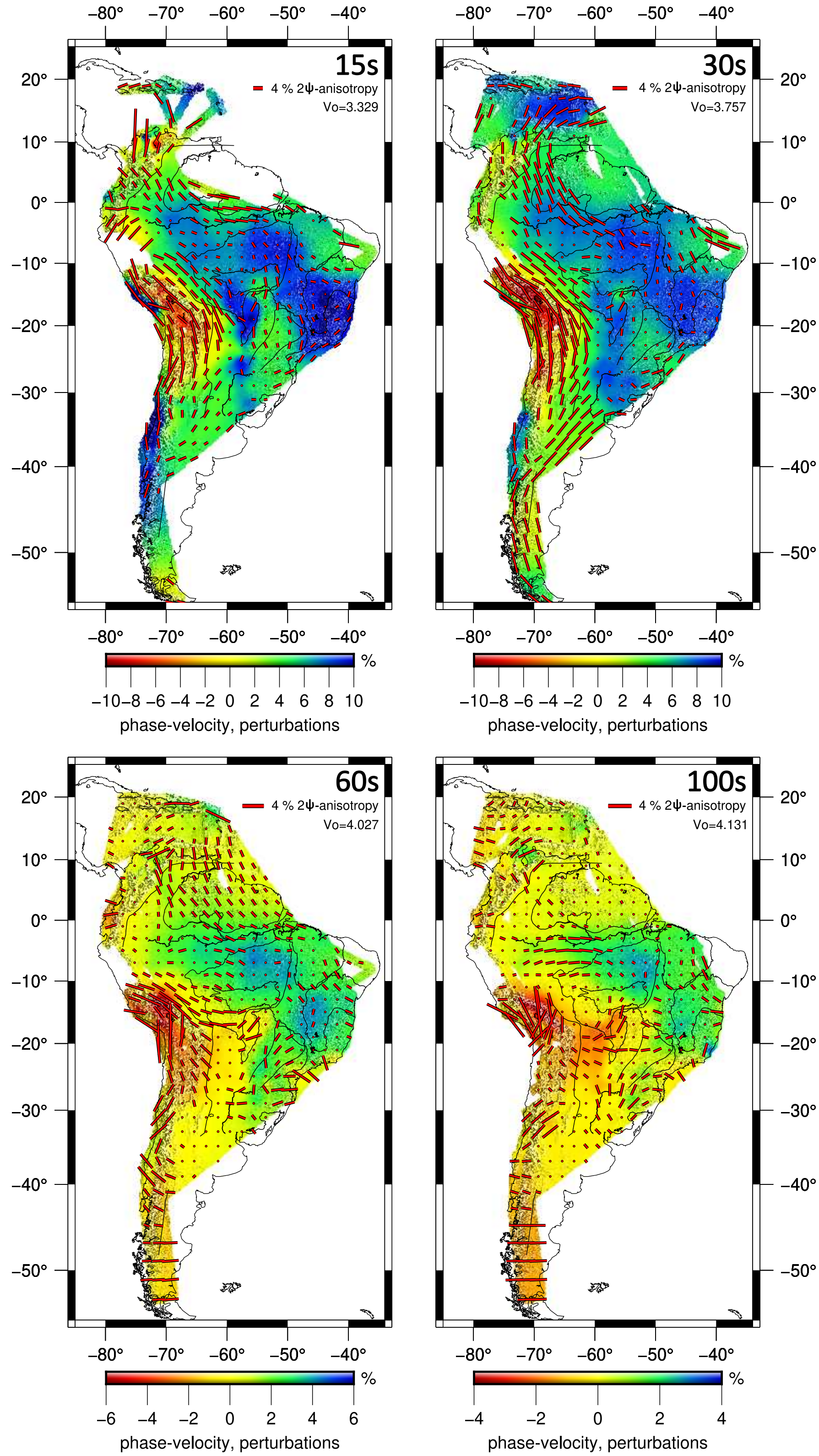

Fig. 13: Final Rayleigh-wave phase-velocity maps for periods 15, 30, 60 and 100s and fast azimuthal directions after removal of anisotropy nodes that failed the rotation tests. Red dots indicate nodes with anisotropy amplitudes below the minimum threshold (<7.41 m/s). The isotropic component remained unchanged.

phase-velocity dispersion curves was developed by Timkó et al. (2022), where the roughness of each dispersion curve is evaluated and the rough segments are removed. The calculation of the rough segments is made using a differentiation function for each frequency ω by taking the frequency-dependent first partial derivative of the measured local dispersion curve

$$C^{'}(\omega) = \frac{\delta C(\omega)}{\delta \omega} \tag{26}$$

and comparing it to the first derivative $C_0^{'}(\omega)$ of a synthetic dispersion curve from a reference model. For each knot of the inversion, synthetic phase-velocity dispersion curves were calculated based on a combination of CRUST1.0 (Laske et al. 2013) and Preliminary Reference Earth Model (Dziewonski and Anderson 1981) reference models. The differentiation function is implemented by Timkó et al. (2022) as

$$Y(\omega) = \frac{C^{'}(\omega) - C_0^{'}(\omega)}{C_0(\omega)} \tag{27}$$

The authors define the roughness $R(\omega)$ by integrating $Y(\omega)$ over a moving window $T(\omega)$

$$R(\omega) = \int_{\omega - T(\omega)}^{\omega + T(\omega)} Y(\omega) d\omega \tag{28}$$

where the window $T(\omega)$ is defined as

$$T(\omega) = a\omega + b \tag{29}$$

with a and b being empirically defined values. Following Timkó et al. (2022), we used 0.05 and 0.01 for a and b, respectively.

A discrete approximation of Eq. 28, R_a, was implemented as follows for each sample N

$$R(\omega) \simeq R_a(\omega) = \sum_{k=1}^{N} \frac{Y(\omega_{k-1}) + Y(\omega_k)}{2} \Delta\omega_k \tag{30}$$

where ω_k values are contained inside of the moving window interval $[\omega - T(\omega), \omega + T(\omega)]$ in steps of $\Delta\omega_k = \omega_k - \omega_{k-1}$. Fig. 15 shows the $R_a(\omega)$ values calculated using Eq. 30.

Timkó et al. (2022) define a threshold where an acceptable roughness at a frequency ω is

$$th_- \leq \frac{R_a(\omega)}{\bar{R}} \leq th_+ \tag{31}$$

where th_- and th_+ are empirically defined thresholds and $\bar{R}$ is the median of $R_a(\omega)$, or 9.464e-5, of all frequencies above an empirical threshold τ. th_-, th_+ and τ were chosen as -15, 5 and 40 s, following roughly Timkó et al. (2022).

Timkó et al. (2022) also implement a strategy to estimate the frequency-dependent standard deviation of the accepted segments, $S(\omega)$, as

$$S(\omega) = \left(\frac{R_a(\omega)}{\bar{R}}\right)^{\epsilon} E(\omega) \tag{32}$$

where $R_a(\omega)$ is the discrete approximation of the roughness function (Eq. 30), $\bar{R}$ median roughness above 40 s as defined for Eq. 31, ϵ is an empirical threshold to scale the influence of the roughness ratio to the uncertainty calculation and $E(\omega)$ is a Rayleigh-wave frequency-dependent *a priori* reference standard deviation. For $E(\omega)$, we used the standard deviation estimated from Rayleigh-wave dispersion curves from El-Sharkawy et al. (2020) for the Mediterranean, varying from $\sim$0.048 to $\sim$0.057 km/s for periods between 15 and 250 s (Fig. 14). ϵ is chosen as 0.15, following roughly Timkó et al. (2022) values.

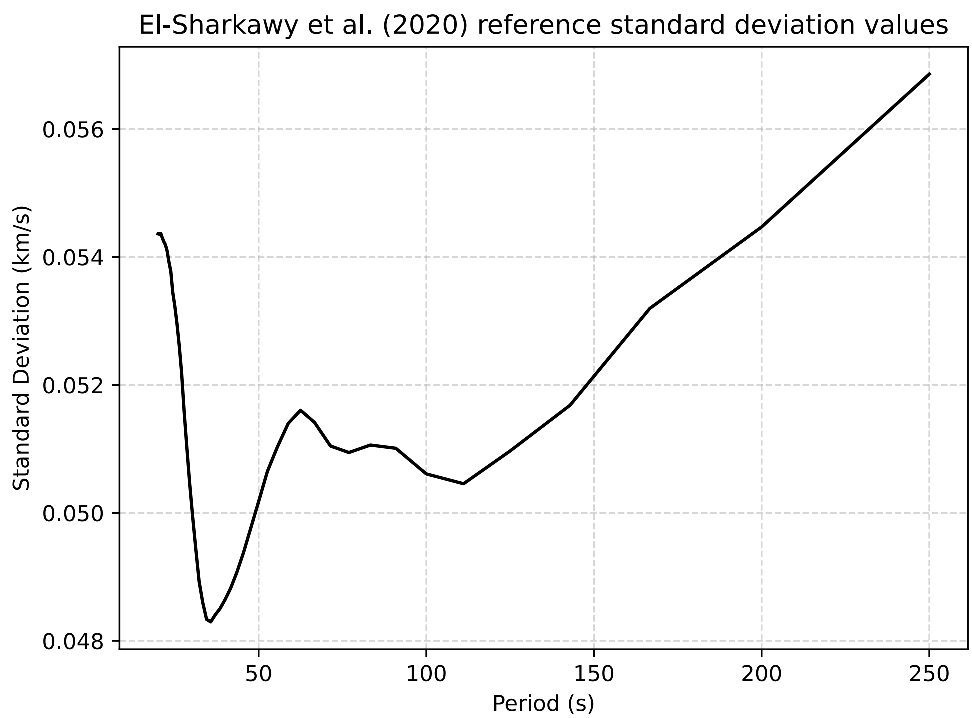

Fig. 14: El-Sharkawy et al. (2020) compilation of reference standard deviation values for the Mediterranean, $E(\omega)$, used in Eq. 32.

5 Depth (V_{SV}) Inversion

In the stable part of South America, S-wave 3D models have been obtained from surface wave tomography maps using mainly linearized inversion of local dispersion curves (e.g. Shirzad et al. 2020; Shirzad et al. 2024; Nascimento et al. 2024). Linearized inversion of group-velocity dispersion and receiver functions have also been used (e.g. Julià et al. 2008; Cedraz et al. 2020; Poveda et al. 2023). However, this type of inversion has complex nonlinearity and its linear approximation requires an initial model close enough to the true earth structure (Ammon et al. 1990; Julià et al. 2000). Stochastic methods, on the other hand, allow for a random iterative search over an acceptable model space to find the best solutions for this inverse problem. We used the isotropic component from the inverted phase-velocity maps to compute a 3-D shear-wave velocity model for the continent using a new stochastic inversion approach by El-Sharkawy et al. (2020).

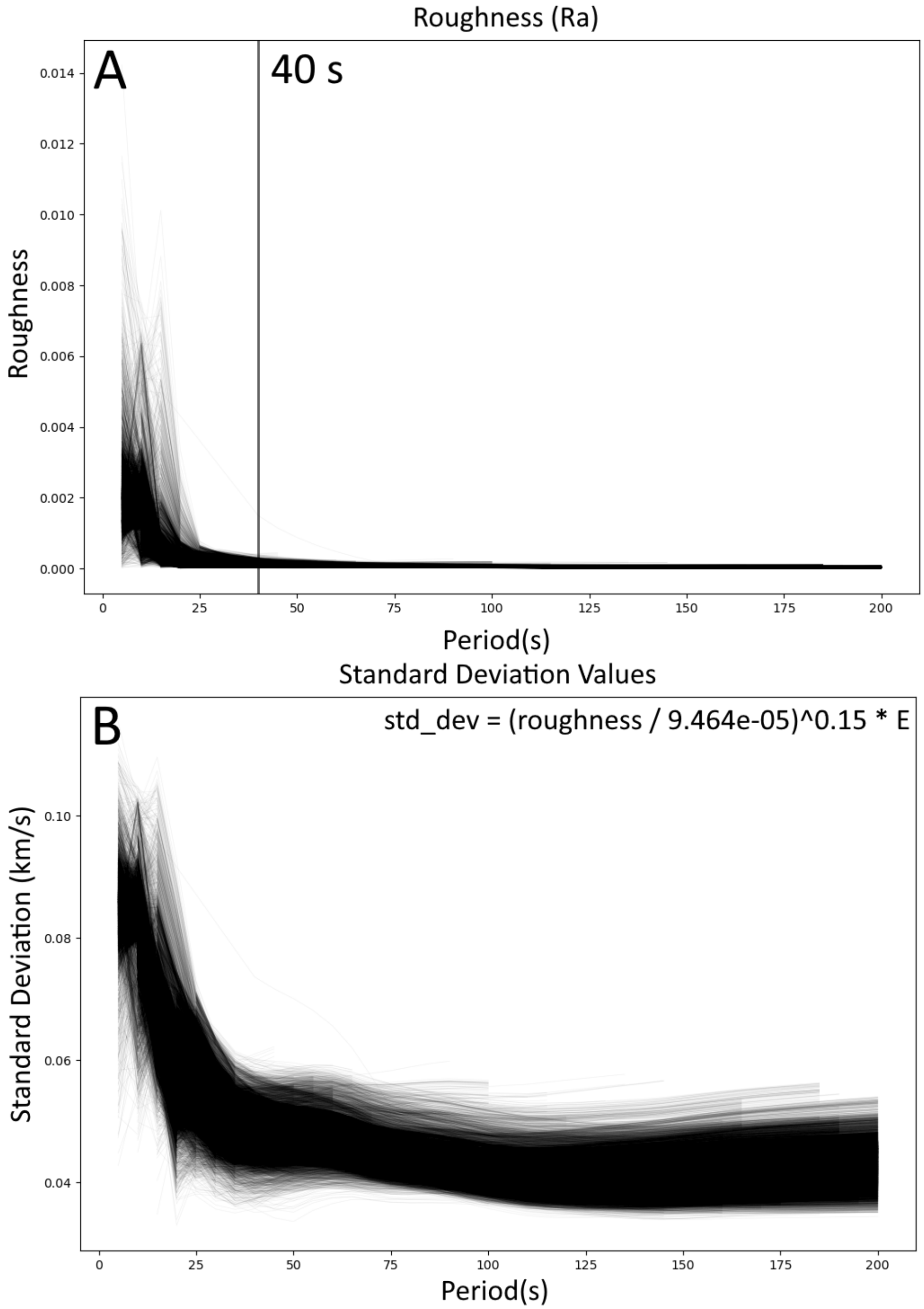

Fig. 15: Local dispersion curve roughness and standard deviation estimation. (a) Absolute roughness values, $|R_a(\omega)|$, as a function of the period. The 40 s vertical bar corresponds to the empirical threshold, τ, above which the median roughness, $\bar{R}$, is calculated. (b) Calculated standard deviation values (Eq. 32 shown in the top right), $S(\omega)$, as a function of the period.

In order to interpret those phase velocities in terms of shear-wave velocities as a function of depth, we used the implementation of El-Sharkawy et al. 2020 which is based on the particle-swarm-optimization (PSO) technique by Eberhart and Kennedy (1995) and Wilken and Rabbel (2012). This technique creates random background model perturbations for specified depth-dependent velocity ranges. We can calculate synthetic dispersion curves from those random models and compare the resulting misfit between the measured and synthetic dispersion curves. The initial background models were created for each node using CRUST1.0 (Laske et al. 2013) and an isotropic average of PREM (Dziewonski and Anderson 1981) for the upper mantle. A depth-dependent parameterization and regularization can be applied to velocity perturbations on each layer and to discontinuities (such as Moho depth). The model global convergence is sped up by resetting the search after a certain number of forward calculations. The synthetic phase-velocity dispersion curves are calculated using the Thomson-Haskell matrix implementation for a 1-D, isotropic and elastic model (Schwab and Knopoff 1972; Knopoff 1964).

5.1 Parameterization and regularization tests

We parameterized our models using 12 parameters with quadratic perturbations on the crust and cubic in the mantle from the Moho depth down to 410 km depth. Perturbations down to 660 km depth are linear. Furthermore, the Moho depth and the depth of the crust and upper mantle nodes are inversion parameters to ensure high parameterization flexibility. The upper crust nodes had a maximum perturbation of 1 km/s, allowing for sedimentary basin shear-wave velocities. All the others were set to 0.5 km/s maximum perturbation. The depth variable nodes for the lower crust, Moho, LAB and Lehmann discontinuity had a variability of depth of 5, 10, 20 and 30 km, respectively. Fig. 16 illustrates the parameterization used for a given background model down to 900 km. Fig. 16b and c show an example of a background model perturbation for a given iteration for a node inside the Amazon Craton (Fig. 7) for the first 300 km. The final models were calculated using 10,000 forward models.

To compensate for the lower resolution at short periods, we applied regularization to the shear-wave velocity differences for: 1) lower crust velocities with relation to the upper crust; and 2) Moho velocity with relation to the lower crust. The shear-wave velocity differences for each subsequent parameter are multiplied with the depth-dependent regularization value, η, and added to the objective function to punish the misfit of forward models with high-velocity gradients between the layers. We show the results for η equals to 0 (no regularization), 0.005, 0.01 and 0.03 for nodes in the Amazon Craton, Pantanal Basin and Andes in Fig. 17, 18, 19 and 20, respectively. In those tests, a better fit between local (black line) and synthetic dispersion curves (red line), as well as a better fit between the best (black line) and centroid (red line) shear-wave velocity models, indicate a more stable solution. For the Andes grid point, the centroid solution provides reasonable velocity and Moho depth for the centroid models. However, the agreements between the best and centroid models are significantly worse than for the other grid points, regardless of the η value used. This instability in the solution is related to a lack of resolution, especially at longer periods, as shown in the checkerboard tests (Fig. 10). For the remaining grid points, Amazon Craton and Pantanal Basin, the better fit happens when $\eta = 0.01$, so we decided to use this value for our final models.

5.2 Final V_{SV} models

Two final models were calculated: (1) the global model with the lowest misfit; and (2) the centroid model. In most cases, we observed that the best-fit model tends to be similar to the centroid model. However, it can sometimes produce final models that do not correspond to an area's expected geological characteristics because the best-fit models represent a local minimum instead of the main features of models around the minimum. We found that the centroid model correlates more closely to the expected features, so we used it instead.

We show an isotropic Rayleigh-wave depth inversion for a node in the Amazon craton

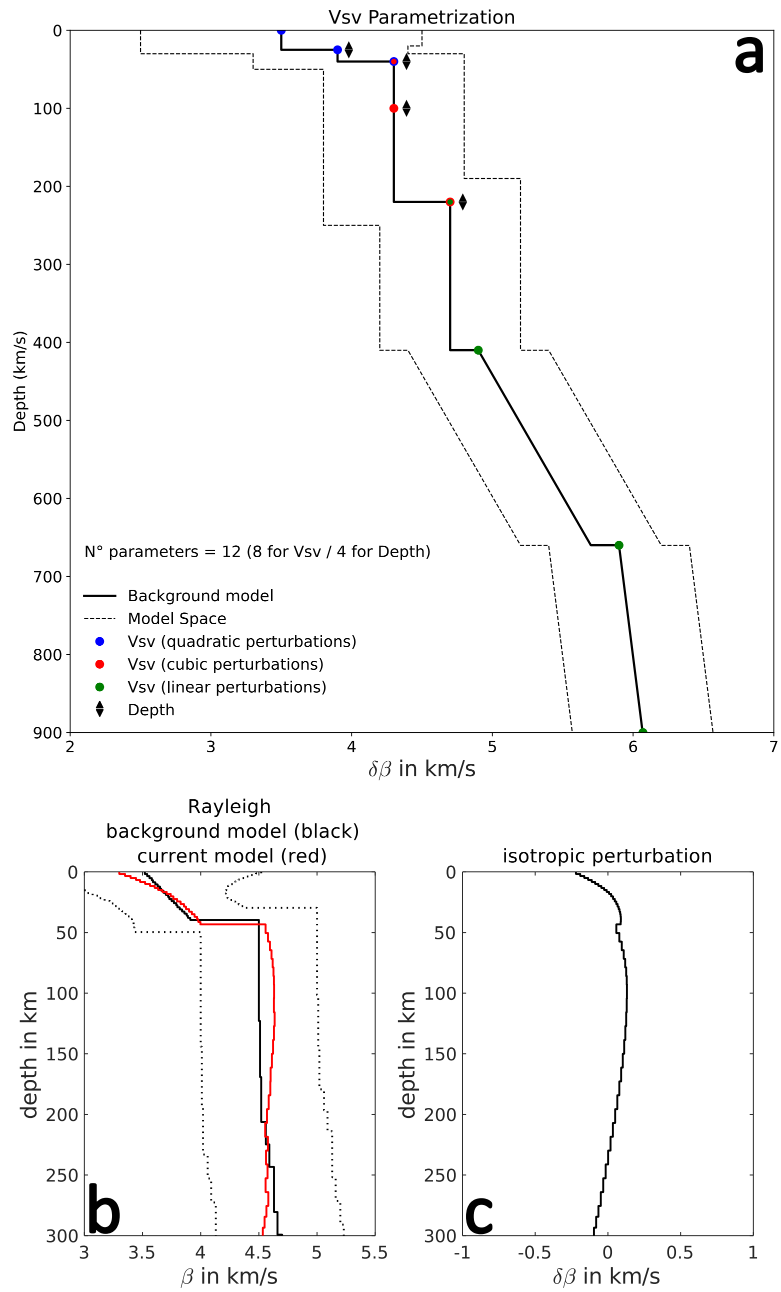

Fig. 16: Background model parameterization example. a) An arbitrary background model is shown as a black line. The model space (dashed black line) is defined as ± 1 km/s for the upper crust and ± 0.5 km/s for the lower crust. 12 inversion parameters are defined as a function of depth as perturbations of the background model, as follows: circles are V_{SV} velocity perturbations; inverted triangles are depth perturbations. The depth perturbations are set between the upper and lower crust and the Moho, LAB and Lehmann discontinuities, which are 5, 10, 20 and 30 km, respectively. b) example of a background model perturbation for a node in the Amazon Craton (blue circle in Fig. 7) for the first 300 km. The background model is shown as a black line, and the model space is shown as a dashed line. The calculated forward model for an arbitrary iteration is shown as a red line. c) random perturbation applied to the background model.

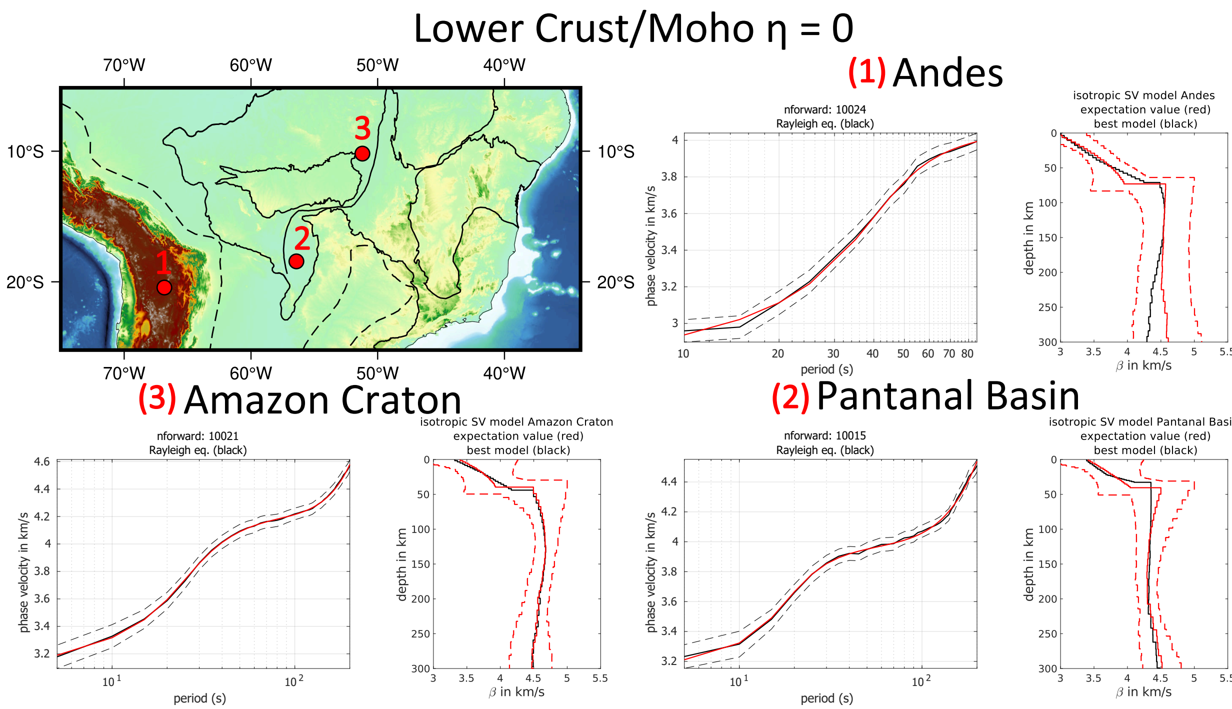

Fig. 17: Regularization test for the V_{SV} inversion for $\eta = 0$ (no regularization) for grid points inside Amazon craton, Pantanal basin and Andes (Fig. 1). The top left figure shows the location of the three test grid points. The remaining figures show, on the left, the local dispersion curve (black curve) with their associated standard deviation (dashed line) and synthetic dispersion curve of the best forward model (red curve. On the right, it shows the best shear-wave velocity model (black line), centroid model (red line) and the models used for calculating the centroid (dashed red line).

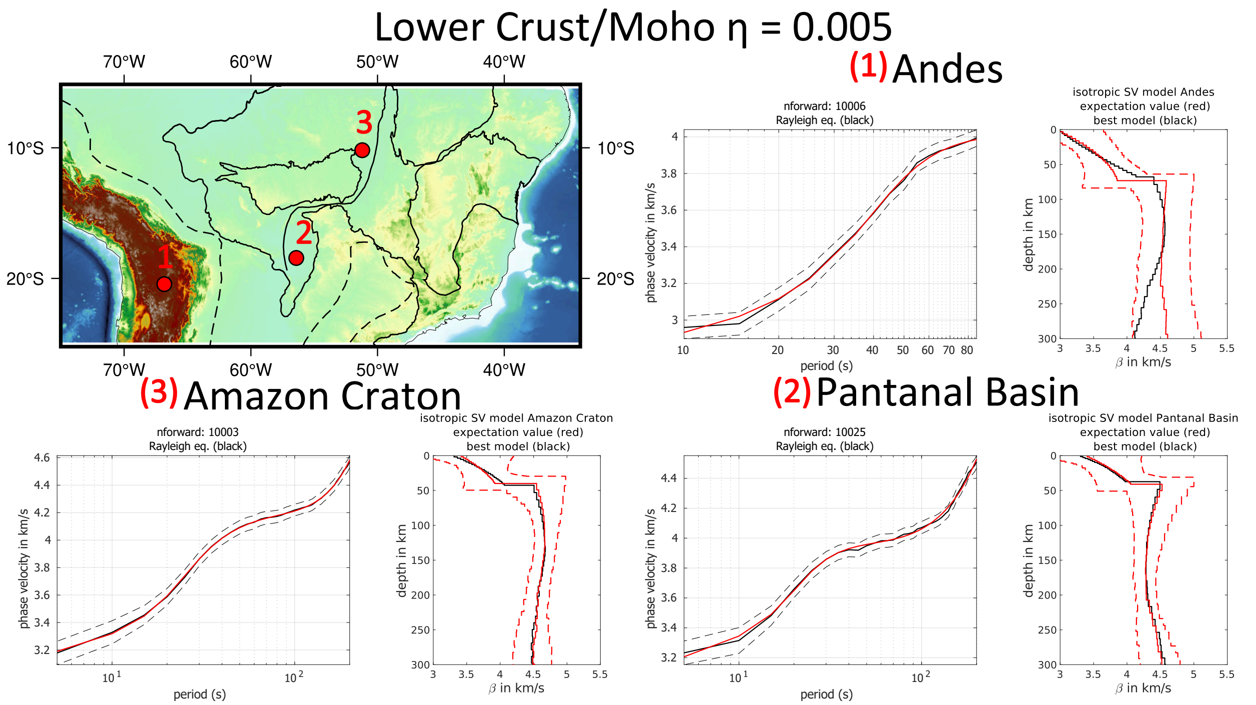

Fig. 18: Regularization test for the V_{SV} inversion for $\eta = 0.005$ for grid points inside Amazon craton, Pantanal basin and Andes (Fig. 1). Same as Fig. 17.

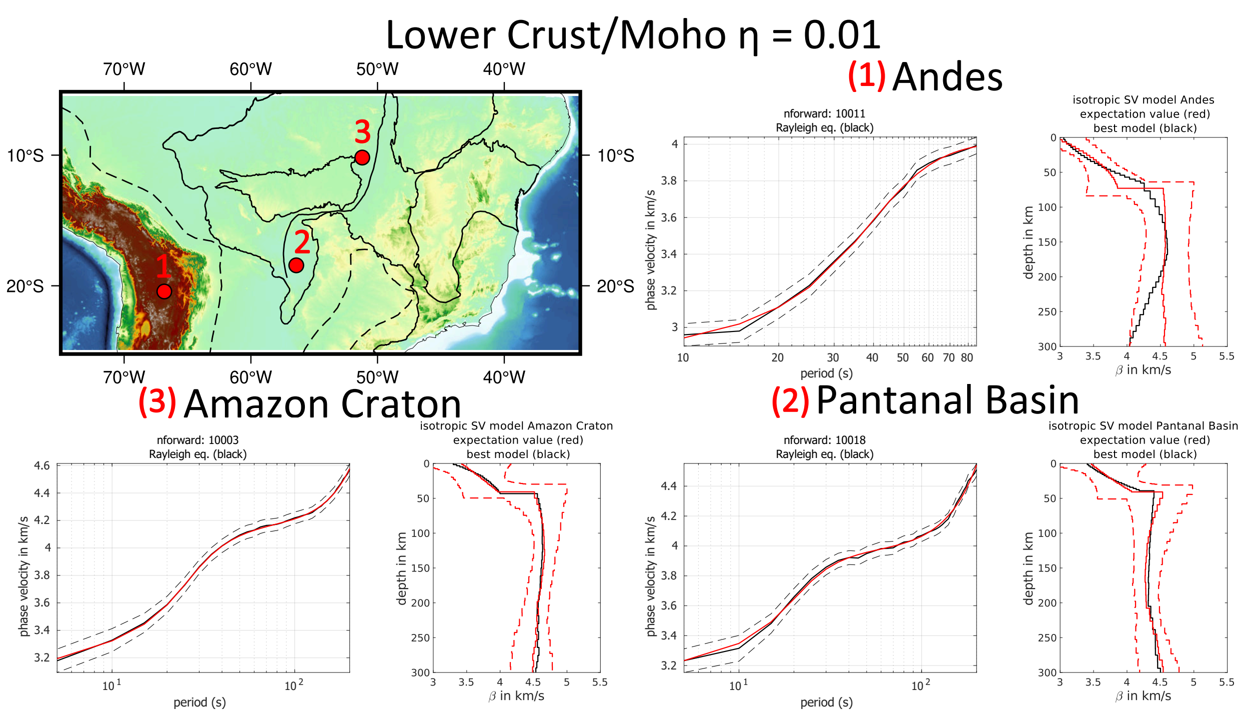

Fig. 19: Regularization test for the V_{SV} inversion for $\eta = 0.01$ for grid points inside Amazon craton, Pantanal basin and Andes (Fig. 1). Same as Fig. 17.

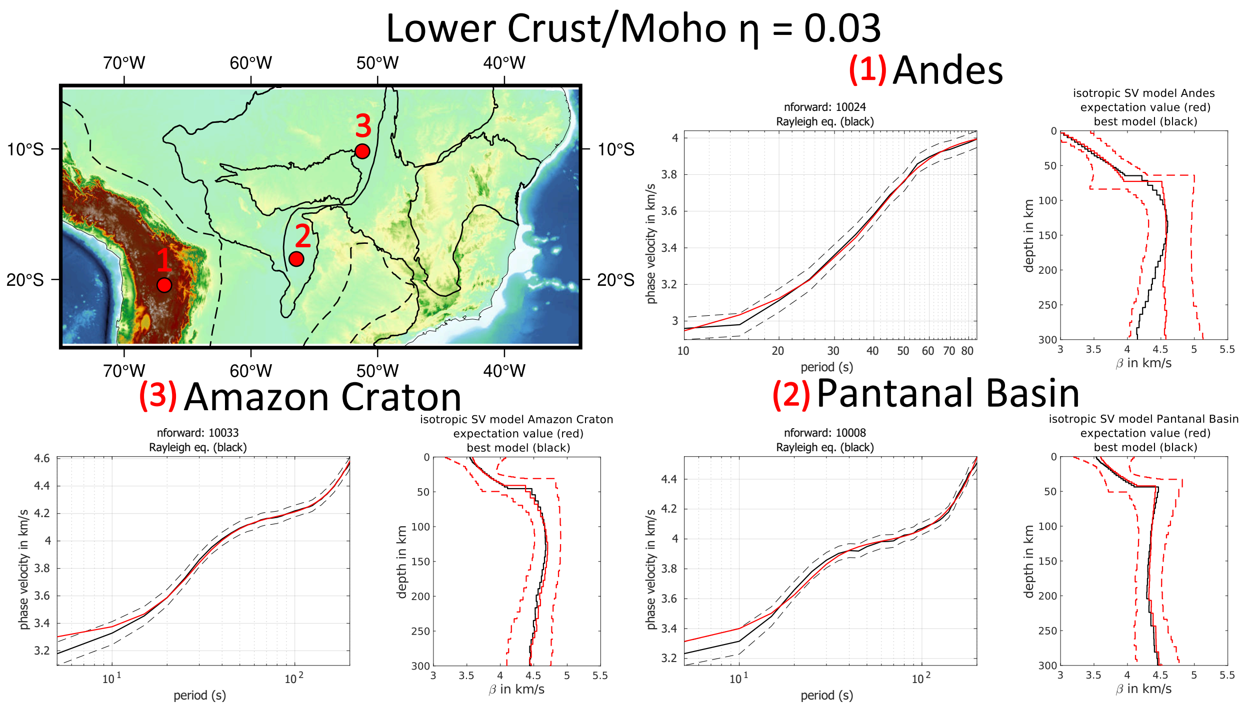

Fig. 20: Regularization test for the V_{SV} inversion for $\eta = 0.03$ for grid points inside Amazon craton, Pantanal basin and Andes (Fig. 1). Same as Fig. 17.

and the Pantanal basin (additional figures are shown in Fig. A3 and A4). Those models' locations are given in Fig. 21. The observed and best model dispersion curves are shown in Fig. 21(a,d) as black and red lines, respectively. The dashed line in Fig. 21(a,d) is the observed curve standard deviation. Fig. 21(b,e) shows the best (black line) and centroid (red line) profiles. The red dashed line in 21(b,e) represents the profiles within 0.5 over the global minimum. Those profiles were used to calculate the centroid model, following El-Sharkawy et al. 2020. Fig. 21(c,f) shows the sampled model space. The profiles are sorted from worst (gray) to best (blue) global misfits. The centroid model is shown as a coarse dashed line.

For the Amazon Craton node (Fig. 21 blue outline). According to the centroid model (red curve Fig. 21B), we observe a pronounced increase in the shear wave velocities around 100 to 200 km, indicating a high lithospheric thickness. Our results for the centroid model agree with the expected thicker lithosphere from Ciardelli et al. (2022) and Priestley et al. (2018) of around 180 km from both studies. Based on the previous crustal thickness map by Rivadeneyra-Vera et al. (2019), we expected a ∼40 km Moho depth for this area that agrees

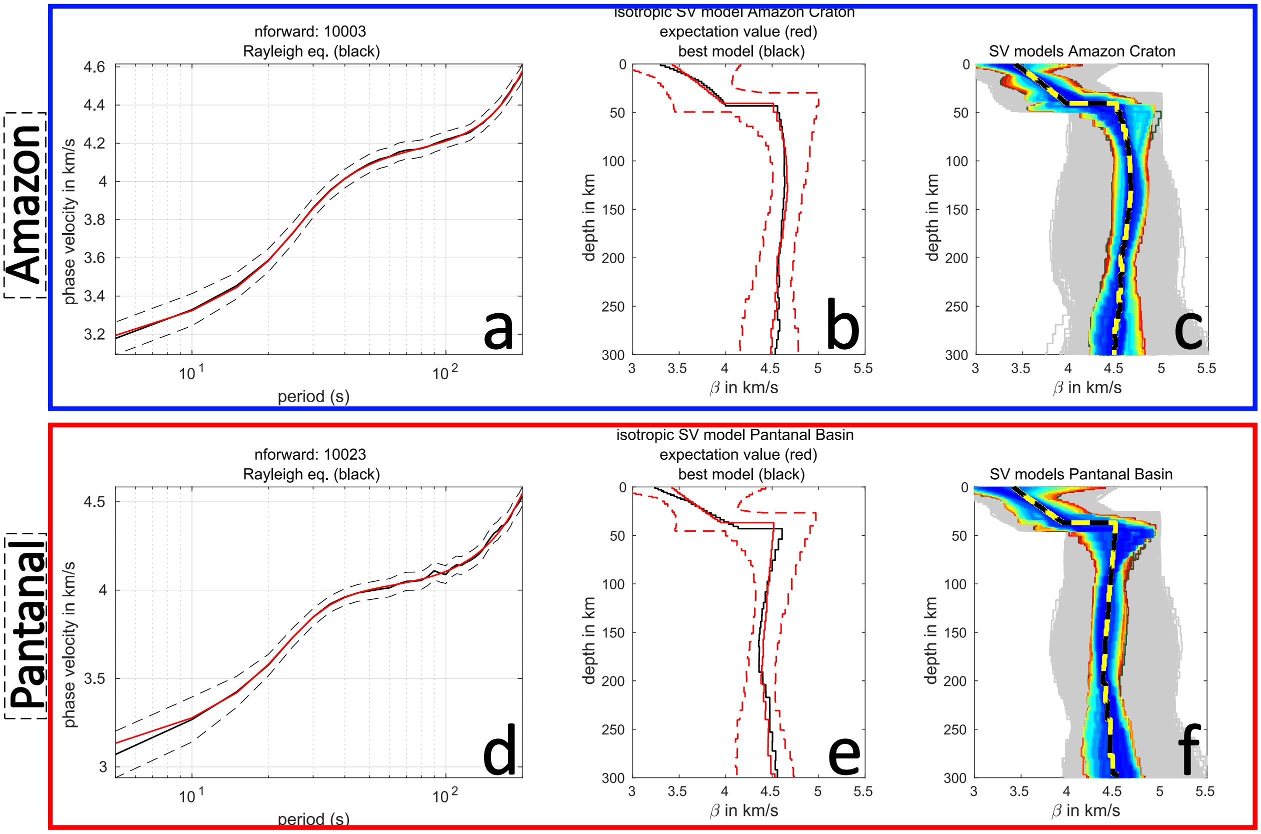

Fig. 21: V_{SV} inversion example for nodes inside the Amazon Craton (blue outline) and Pantanal Basin (red outline) node locations shown in Fig 7. (a,d) Observed local dispersion curve (black line) and its standard deviation (dashed). The red line is the best-inverted dispersion curve. (b,e) 1-D shear-wave velocity profile. Black and red lines are the best-fitting and centroid models, respectively. Red dashed lines show the range of models used to calculate the centroid. (c,f) Gray-shaded areas show the sampled model space, colored models are sorted according to their misfit values. The coarse dashed line is the centroid model.

with the 40 km moho found.

For the Pantanal Basin node (Fig. 21 red outline). The centroid model (red curve Fig. 21B) has a pronounced decrease in shear wave velocities from 100 to 200 km, indicating a shallow lithosphere. This result agrees with Ciardelli et al. (2022) and Priestley et al. (2018). The centroid model also shows a thinner crust (∼37 km) corresponding with the thin crustal thickness found in previous works (Rivadeneyra-Vera et al. 2019; Cedraz et al. 2020).

5.3 Horizontal Slices, Moho Map and Vertical Cross-sections

Using the centroid models, we made a V_{SV} velocity anomaly map for the region between 15 and 300 km. We show results for depth slices at 15, 60, 100 and 300 km (Fig. 22). All the depths can be seen in the appendix (Fig. A5). The anomalies are plotted in relation to average velocities for each depth and reference values are shown at the top right of each figure. We present a Moho thickness map in Fig. 23. We also did nine vertical cross-sections of the model across South America (Fig. A6), with the more important ones for discussion in Fig. 24. To improve the visualization of the crustal structure, we separated the crustal and mantle profiles along the inverted Moho depths and used different vertical scales for both of them. To enhance the visualization of the lateral variations, we plotted the V_{SV} velocities relative to an empirically defined depth-dependent linear gradient (Fig. 24) with different values for the crust and mantle, following Timkó et al. (2022). To identify the top of the Nazca slab, we plotted the ISC-EHB (ISC 2023; Engdahl et al. 2020; Weston et al. 2018; Engdahl et al. 1998) seismicity on the profile. The ISC-EHB is a dataset of teleseismically well-constrained events and is well-suited to visualize subduction zones.

6 Discussion - Paper I

6.1 Phase-velocity maps

The isotropic phase velocity maps at periods of 15 and 30 s (Fig. 13) indicate around 8% high-velocity perturbations in the regions of: (1) cratonic blocks of the South American Platform (Brazil Shield, São Francisco and Rio Apa cratons); and (2) under the Pantanal basin, possibly related to a high-velocity lower crust. We also observed between -8 to -4% low-velocity perturbations in the Andean Mountain range root below the Bolivian Altiplano

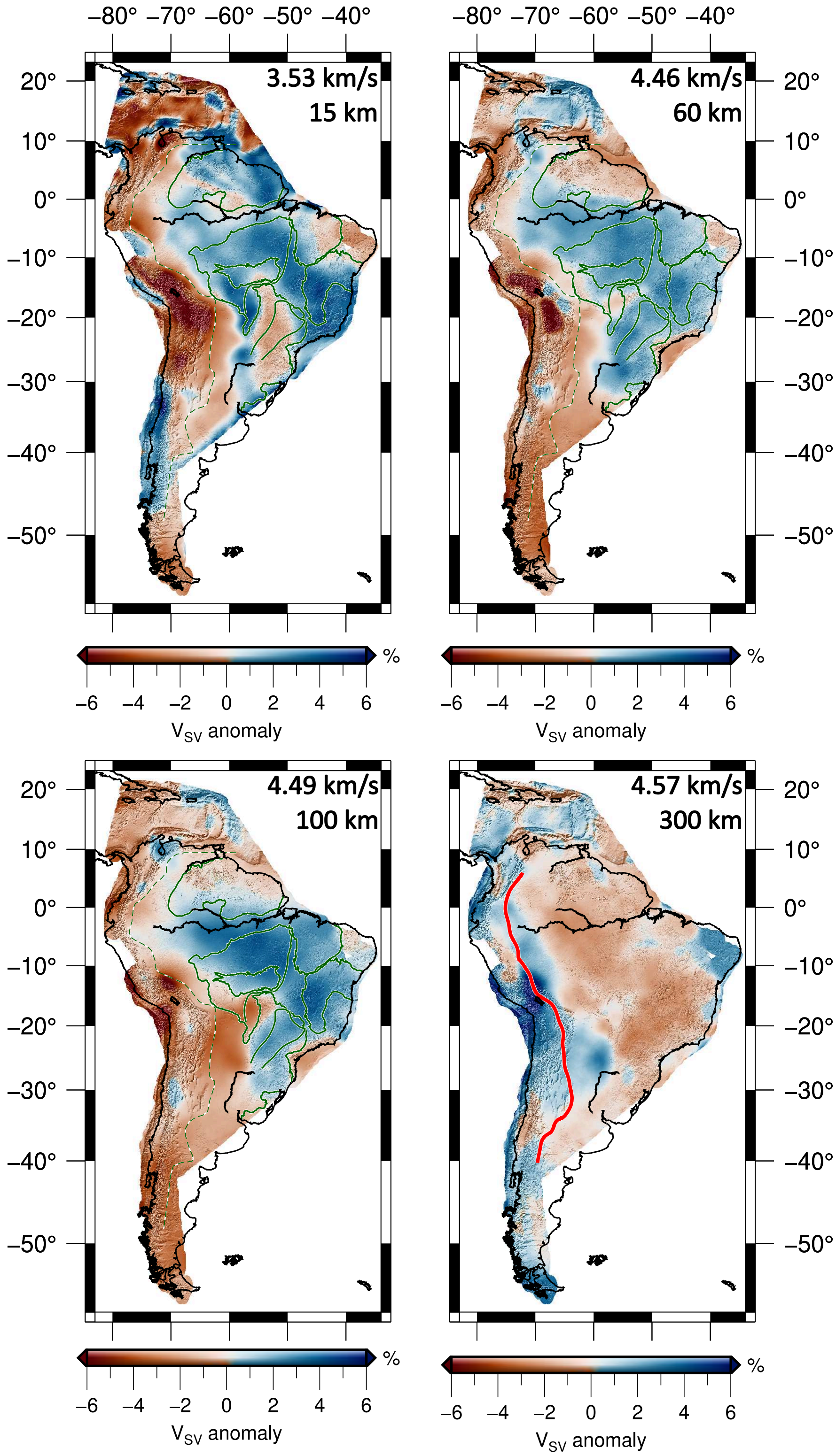

Fig. 22: 3D shear wave velocities for South America at 15, 60, 100 and 300 km. V_{SV} anomalies are shown in relation to the regional average for each depth (top right velocity in each map). For 15, 60 and 100 km, the green outlines are the main tectonic units of South America shown in Fig. 1. For 300 km, the red outline is the Nazca Plate Slab2 model for the same depth (Hayes et al. 2018).

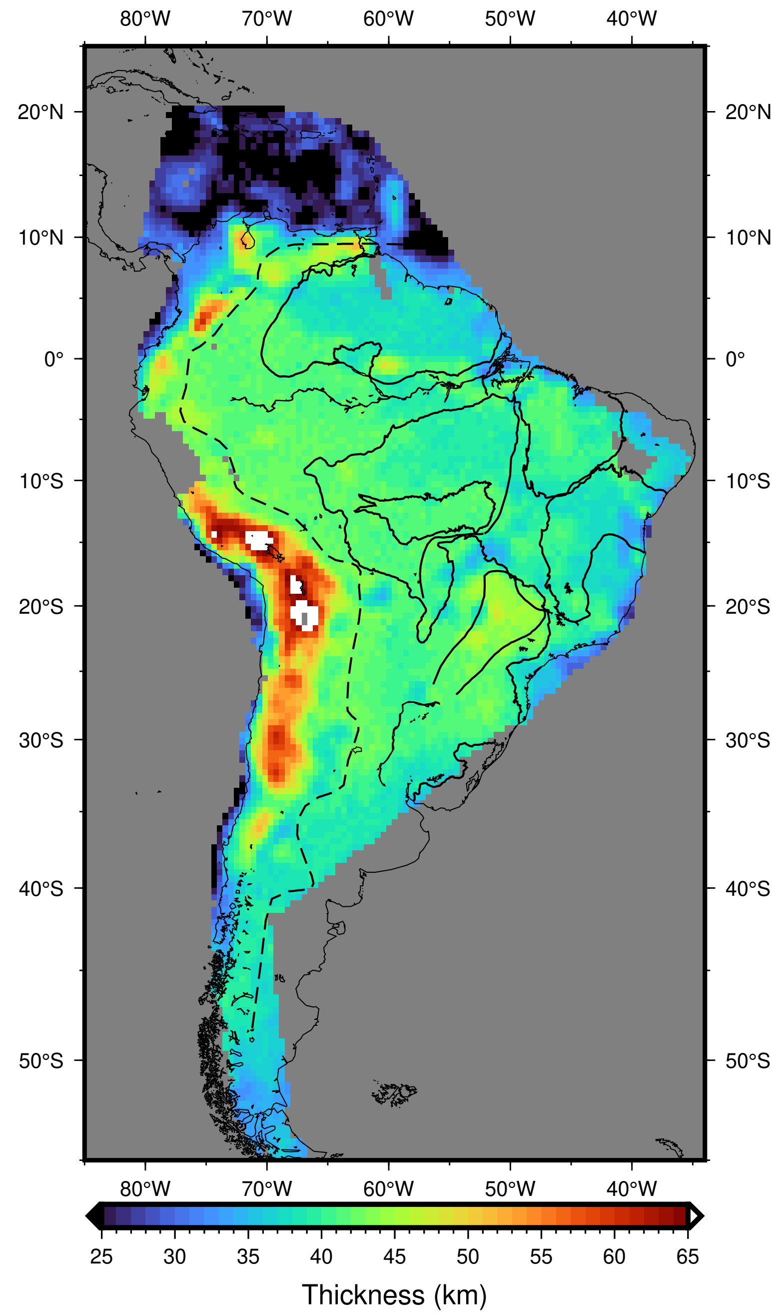

Fig. 23: Crustal thickness map for South America derived from the V_{SV} inversion. Black lines are the main tectonic units of South America, as in Fig. 1.

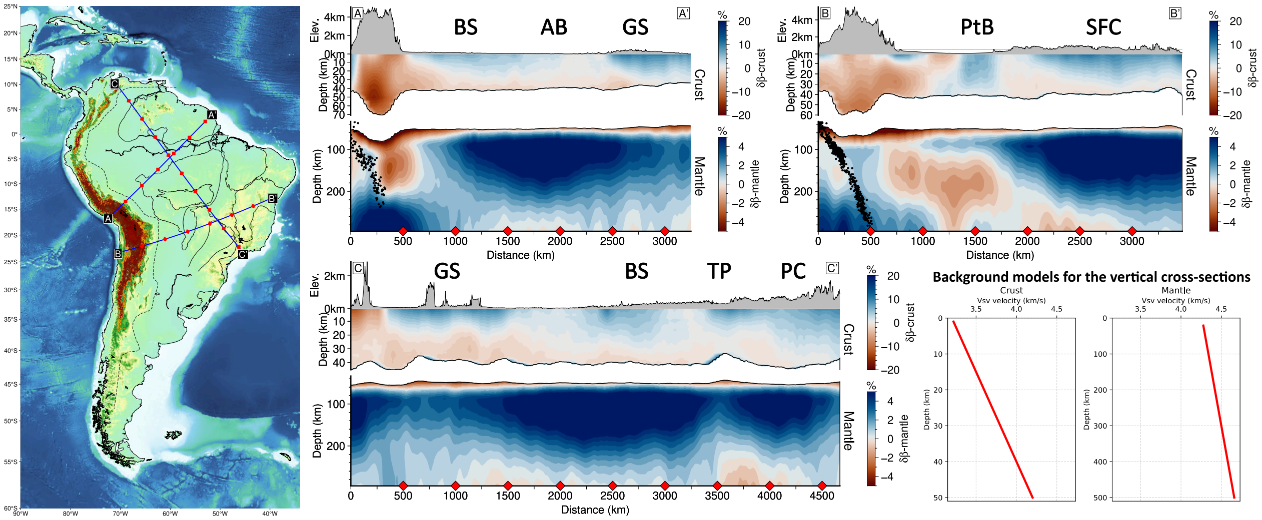

Fig. 24: Vertical cross-sections (A, B and C) through the shear wave velocity model, with red diamonds plotted every 500 km along the profiles. The shear wave anomalies are plotted in relation to a 1D gradient velocity model for the crust and mantle. Topography is plotted above each cross-section. BS = Brazilian Shield, GS = Guyana Shield, SFC = São Francisco Craton, AB = Amazonian Basin, PtB = Pantanal Basin and TP = Tocantins Province, as shown in Fig. 1. The ISC-EHB seismicity (ISC 2023; Engdahl et al. 2020; Weston et al. 2018; Engdahl et al. 1998) is shown as black dots.

(Central Andes). The Paraná, Chaco-Paraná and Parecis intracratonic basins also have lower velocities relative to the neighboring cratonic areas. Those maps also show, in the Central Andes, anisotropy fast directions parallel to the continent coast consistent with the known compression of the South American Plate from the subduction of the Nazca slab (e.g. Assumpção et al. 2016).

The 60 and 100 s (Fig. 13) maps are mostly sensitive to the lithosphere. The high velocities ($\sim 3\%$) in the South American Platform's eastern portion correlate well with the deep roots of the oldest region of the Amazon and the São Francisco cratons. Lower velocities ($\sim -2\%$) can be seen below the Pantanal basin area and are well correlated with the shallower depths of the LAB from continental scale tomography (Ciardelli et al. 2022) and global model (Priestley et al. 2018). Overall, we do not observe the anisotropy direction changes around the cratonic roots of the Paranapanema and Amazon cratons (Melo et al. 2018; Assumpcao et al. 2011; Assumpção et al. 2006). However, we observe a roughly NE-SW fast direction below the Pantanal basin that coincides with the area of low-velocity and thin LAB.

For 30, 60 and 100 s (Fig. 13), we observe that the Guyana shield has lower velocities than the Brazil Shield. This result can be seen similarly in the surface-wave group velocity tomographies of Rosa et al. (2016) and Nascimento et al. (2022). However, Celli et al. (2020) and Ciardelli et al. (2022) do not see systematic differences between the shields.

6.2 Depth inversion

At 15 km depth (Fig. 22), we see a good correlation with known crustal tectonic units of South America. High velocities (∼2 to 4% V_{SV}) in the crust inside the Amazon craton (Brazil Shield and Guyana Shield), São Francisco craton, Pantanal basin's basement and Rio Apa craton (small-scale high to the south of the Pantanal basin). We also see lower velocities (∼-2 to -6% V_{SV}) in the Paraná and Parecis sedimentary basins and the Andes. In the Caribbean, we see a spotted pattern that is expected, given the thinner oceanic crust. We observe a high-velocity anomaly between the Paraná and Chaco-Paraná basins (∼1% V_{SV}). The surface-wave Ambient Noise Tomography of Shirzad et al. (2020) V_{SV} inversion also shows a high-velocity anomaly in the Pantanal basin and a low-velocity anomaly in the Paraná basin at 20 km. The authors also observe a high-velocity anomaly in the transition between the Paraná and Chaco-Paraná basins at 30 km.

At 60 km depth, we mainly see the contrast between the high velocities of the cratonic South American Platform and the low velocities of the crustal roots of the Andes. For the cratonic area, the main characteristic is the difference between the average velocity in the northern and southern parts of the Amazon craton (profile B-B' in Fig. 24). The northern shield (Guyana Shield) seems to have lower average velocities than the south (Brazil Shield) and this difference is consistent with depth in our inversions (Fig. A5 and Fig. 24 A-A'). Therefore, structural differences could exist between the northern and southern Amazonian cratons, which will be discussed in more detail below.

At 100 km depth, we mostly observe lithospheric features and the distinction between the cratonic South American Platform, on the East, and the Andean and subandean regions, on the West. An important characteristic is the lower shear velocities (~-4% V_{SV}) beneath the Pantanal and Chaco-Paraná basins. This low-velocity zone is well delineated in our model and correlates well with the shallow LAB in Priestley et al. (2018) and Ciardelli et al. (2022) . It will be discussed in more detail below. We observe high-velocity anomalies (~5% V_{SV}) in the Amazon and São Francisco that are coherent with the areas of deepest LAB (~180 km) for those cratons (Priestley et al. 2018; Ciardelli et al. 2022). The lower velocities (~-2% V_{SV}) in the Mantiqueira fold belt also correlate well with the shallow LAB (~70 to 90 km) expected in this area (Priestley et al. 2018; Ciardelli et al. 2022). We also see higher velocities (~2% V_{SV}) under the Paraná basin that can be attributed to the Paranapanema craton underneath the basin. Profile B-B' (Fig. 24) shows the transition between the ~100 km LAB under the subandean region and the Pantanal basin (distances between 550 to 1,750 km) to the ~200 km LAB to the east. Profile C-C' (Fig. 24) shows the cratonic roots of the Amazon and Paranapanema cratons from 1,500 km onward. We also observe crustal and lithospheric thinning near the TBL in the Tocantins fold belt (around 3,500 km in Profile C-C'). The thin crust was also observed in seismic refraction profiles (Berrocal et al. 2004) and receiver functions (Assumpção et al. 2013b; Assumpção et al. 2013a; Rivadeneyra-Vera et al. 2019). Assumpção and Sacek (2013) proposed that crustal thinning could produce higher stresses in the upper crust, which would explain the higher seismicity observed in the area. Lithospheric thinning was also suggested as an additional contributor to the concentration of stresses in the upper crust (Assumpção et al. 2004b). This result is in agreement with the low-velocity anomalies observed in the upper mantle from P-wave tomography (Rocha et al. 2016; Assumpção et al. 2004a).

At 300 km depth, the anomalies are generally well correlated with those found in the Adjoint Tomography of Ciardelli et al. 2022. We resolve general high-velocity anomalies to the west, correlating well with the subduction of the Nazca plate (Slab2 model in Fig. 22 by

Hayes et al. 2018). We can observe the slab in the Central Andes (~15°S 70°W in Fig. 22 at 300 km) where we see a pronounced high-velocity anomaly (~6% V_{SV}). East of the slab (~26°S 60°W) we observe a high-velocity anomaly (~3% V_{SV}) similar to Ciardelli et al. 2022 model. To the south of 35°S the slab is not seen clearly given the poor resolution at the longer periods, as shown in the checkerboard tests in Fig. 10. In NE Brazil we observe a high-velocity anomaly in the Borborema province, similar to Celli et al. (2020), but different from the low velocities of Ciardelli et al. 2022. However, our model is on the edge of its resolution in that region (Fig. 10) to resolve this difference.

6.3 Crustal thickness

We observe thick crust in the Andes (>55 km) and the thin oceanic crust in the Caribbean (<25 km) as major features (Fig. 23). More importantly, we can resolve smaller-scale features, such as thinner crust east of the Pantanal basin and thicker crust inside the Paraná basin. Those are examples of smaller-scale features that correlate well with the thickness map of Rivadeneyra-Vera et al. (2019). The thin crust in the Pantanal basin could have been caused by a delamination near the TBL, as hypothesized by Cedraz et al. (2020). The thicker crust beneath the Paraná basin is usually associated with its thick sedimentary layer (up to 7 km). Overall, our Moho map is consistent with the known crust thickness in South America (derived mainly from receiver functions), indicating that the depth inversion solutions should be helpful in areas where no local data is available, such as the Amazon region.

6.4 Pantanal Basin and thin lithosphere

Low velocities (~-4% V_{SV}) can be seen inside and to the SW of the Pantanal basin (around 19°S 59°W) at 100 km (Fig. 22 and 24B-B'). This low-velocity anomaly has been observed in several tomographic models (e.g. Ciardelli et al. 2022; Nascimento et al. 2022;

Celli et al. 2020; Rocha et al. 2019; Lee et al. 2001; Feng et al. 2004) which makes it a major feature of the upper mantle of the South American Lithosphere. We observe this anomaly from around 70 to 200 km depth (Fig. A5). Both the global model of Priestley et al. (2018) and continental tomography of Ciardelli et al. (2022) show a thin lithosphere (∼100 km) in this area. Those results confirm that these upper mantle low velocities are related to a shallow asthenosphere. In this area, the anisotropy fast direction (Fig. 13 at 100 s) shows an E-W trend just east of the Andes, parallel to the motion of the Nazca Plate relative to the South American Plate (Gripp and Gordon 2002). A change to NE-SW trend, following the low-velocity anomaly under the Pantanal basin, is observed, and it is consistent with mantle flow deflected by the Paranapanema cratonic root, as suggested by Melo et al. (2018) and Assumpcao et al. (2011). However, we do not observe the NW-SE directions south of the Paranapanema craton, as observed by Melo et al. (2018) and Assumpcao et al. (2011). This could be in partly due to low resolution south of 32°S or mantle flow in this area is deeper and not affecting our azimuthal anisotropy at 100 s.

6.5 Amazonian Craton

Geochronologically, the Amazon craton is thought to have been formed by crustal accretion during different orogenic cycles (Santos et al. 2000; Santos et al. 2006; Tassinari and Macambira 1999). The oldest provinces (Santos et al. 2000) are in the eastern part of the craton, such as the Carajás-Imataca (3.0 to 2.5 Ga). The eastern region of the Guyana Shield is mainly composed of the younger Transamazonic province (2.25 to 2 Ga).

Both regional and global scale tomography models show high-velocity shear wave anomalies around 100 km depth in the eastern regions of both shields (Ciardelli et al. 2022; Celli et al. 2020; Feng et al. 2004; Feng et al. 2007; Lebedev and Hilst 2008; Nascimento et al. 2024) relating it to a thicker cratonic root of the oldest provinces. LAB models derived from shear-wave velocities provide different accounts of the cratonic roots of each shield. Priestley et al. (2018) show a lithosphere 180 km thick for both shields. On the other hand, Ciardelli et al. (2022) show in the eastern Guyana Shield a lithosphere ∼110 km thick while the eastern Central Brazil Shield has a ∼160 to 180 km lithosphere. Surface wave group velocities at 100 s tend to be lower in the north and higher in the south (e.g. Nascimento et al. 2022; Rosa et al. 2016), corresponding roughly to a 100 km depth maximum sensitivity for shear-wave velocity kernels. Our phase-velocity map (Fig. 13) for 100 s also shows higher velocities in the Eastern Central Brazil shield compared to the Guyana shield.

At 100 km (Fig. 22), we observe high-velocity anomalies (∼5% V_{SV}) in the eastern Brazil Shield and no anomalies in the eastern Guyana shield. It is possible that the lack of sufficient azimuthal coverage in the area due to a lack of stations makes it difficult to resolve this dispute. However, our checkerboard tests can reasonably recover anomalies in this region larger than 6° (Fig. 10). Therefore, even if small-scale anomalies can not be recovered due to poor coverage, the average seismic properties in the Guyana shield may be preserved in our model, especially given that the lack of a high-velocity anomaly is constant with depth (Fig. A5 and Fig. 24A-A'). The average low V_{SV} in our model could indicate that a cratonic root never formed or it was reworked by volcanic activities during the evolution of the Guyana shield, such as the back-arc extension around 2.2 Ga in French Guyana (Santos et al. 2000) or by the magmatism around 200 Ma that occurred in the CAMP (Deckart et al. 2005; Marzoli et al. 2018).

7 Ambient Noise

To improve the density of interstation measurements, especially at shorter periods, we decided to use Ambient Noise Data to compute additional Rayleigh-wave phase-velocity dispersion curves in our study area. We downloaded the daily raw continuous waveform records of the vertical component of 138 seismic stations from 1998 to 2022 from the RSBR (Bianchi et al. 2018) and from the temporary deployments of the "3 Basin Project". The

RSBR is most dense in the SSE region of Brazil (Fig. 25a), with most stations being deployed after 2015 (Fig. 26) when the seismic network was greatly expanded. Fig. 25b shows the interstation measurements available between each station pair. A total of 163,191 days were downloaded across all stations, with an average of 1,182.54 daily records per station. All waveform data was downloaded from the International Federation of Digital Seismograph Networks (FDSN) service of the *Centro de Sismologia* of the University of São Paulo[2].

The following steps were applied to the raw waveform data, following Bensen et al. (2007): (1) resampled to 5 Hz; (2) instrumental response correction; (3) detrend; (4) demean; (3) tapered; (4) bandpass-filtered between 1 and 200 s; (5) time-domain normalization; (6) running-absolute mean normalization and (7) spectral whitening. The daily records are then cross-correlated and linearly stacked. A total of 3,396 Cross-Correlation Functions (CCF) were produced and can be seen in Fig. 27 filtered between 10 and 100 s to improve the Rayleigh-wave group-velocity arrival visualization at around 3 km/s.

The CCFs are then spectral filtered to isolate the Rayleigh-wave fundamental mode from noise and the higher harmonics (Meier et al. 2004). Gaussian and band-pass filters are applied according to Sec. 2.2. The phase-velocity dispersion curves are extracted in the frequency domain using the automatic algorithm by Wiesenberg et al. (2022). The final dispersion curve selection follows the steps in Sec. 2.3. An additional selection step is the minimum frequency for each dispersion curve segment and it is applied after all the ones from Sec. 2.3. This threshold is distance-dependent and created by interpolating a line defined at the points 400 km and 20 s and 3000 km and 100 s. For example, a phase-velocity curve derived from a pair of stations with an interstation distance of 400 km must have a minimum frequency of 0.05 or 20 s. Fig. 28 exemplifies the dispersion curve selection for the station pair PP1B-BBPS in Brazil. After applying the selection criteria, 1,477 final phase-velocity dispersion curves were selected (Fig. 29 and Fig. 30). The computed phase velocities were determined between 2 and 100 s with around 1,000 dispersion curves with periods below 10 s.

[2] http://seisrequest.iag.usp.br/fdsnws/

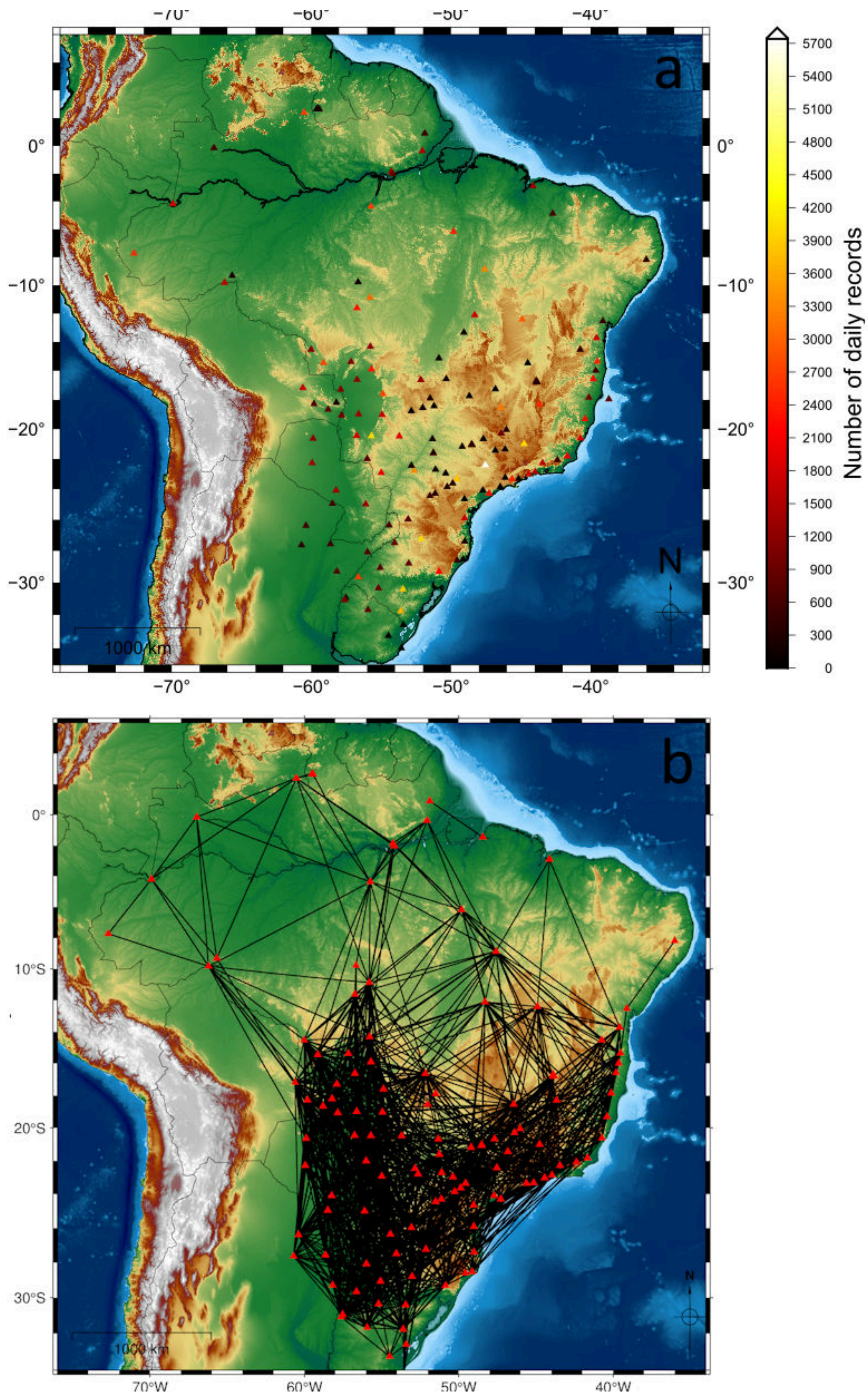

Fig. 25: The 138 broadband stations used in the Ambient Noise analysis. Daily raw continuous waveform records of the vertical component from 1998 and 2022 were downloaded. a) The color scale indicates the number of daily records downloaded for each station. b) interstation paths available between the stations pair.

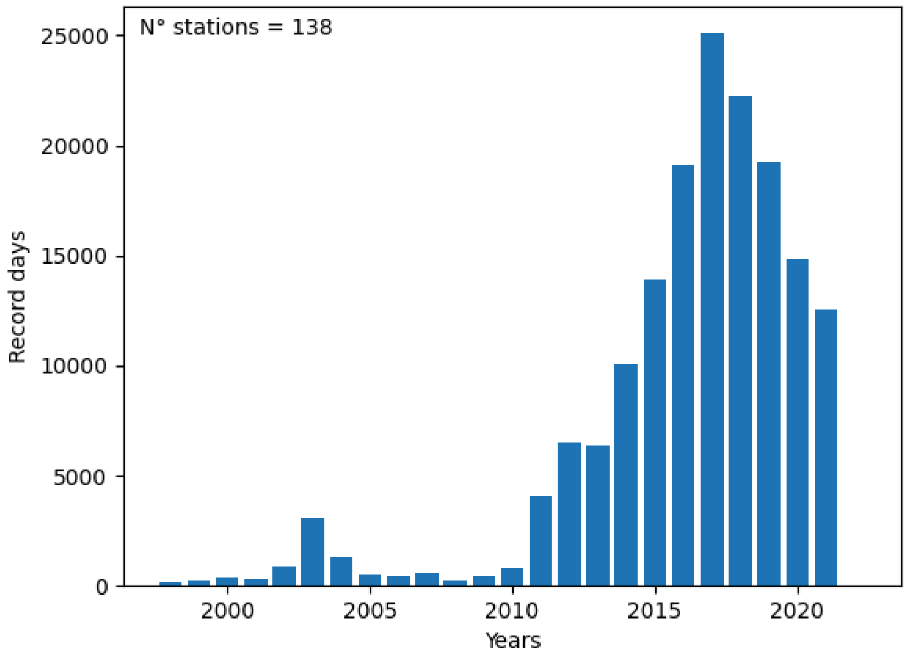

Fig. 26: Number of daily records as a function of the years used in the Ambient Noise analysis.

The ambient noise dataset complements the previously determined earthquake dispersion curves (Sec. 2) at shorter periods and by having a lower shorter period (i.e. 2 s instead of 4 s).

7.1 Dispersion curve dataset integration

The Ambient Noise (AN) and Earthquake (EQ) datasets contain 1,477 and 19,522 dispersion curves, respectively. The AN dataset corresponds to around 7.5% of the EQ dataset. We integrated our AN and EQ datasets to compute higher-resolution phase-velocity inversions for SSE Brazil, repeating the methodology of Sec. 3. However, it is known that there is a systematic discrepancy between the velocities obtained from AN and EQ data (e.g. Kästle et al. 2016; Magrini et al. 2022; Yao et al. 2006; Köhler et al. 2012; Timkó et al. 2022; Zhou et al. 2012). Usually, it is observed that AN data has, on average, a 1 to 2% lower

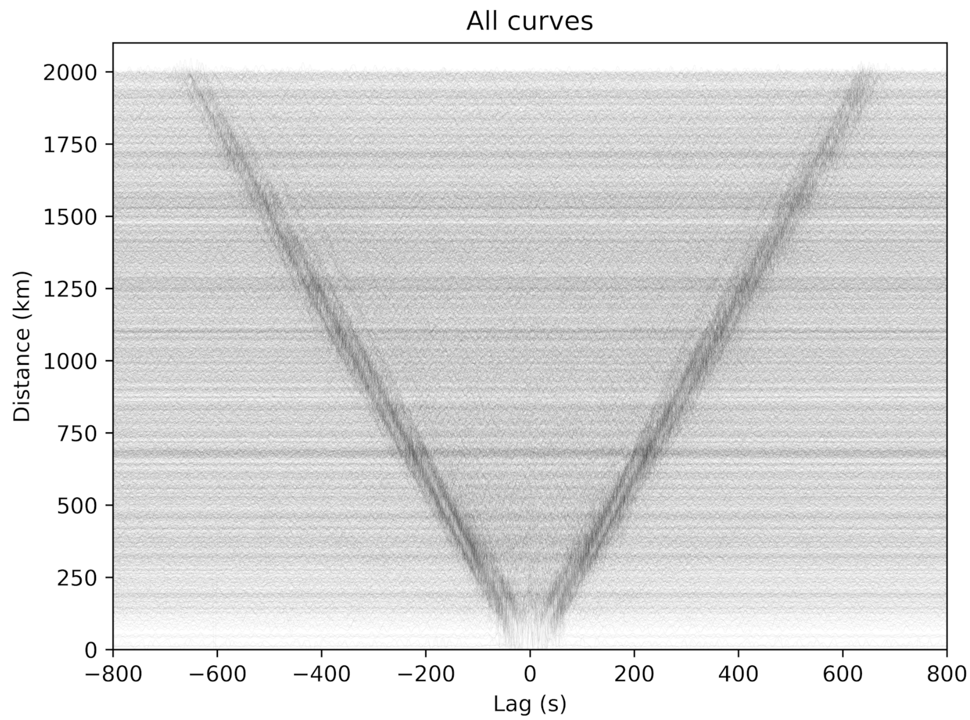

Fig. 27: Rayleigh-wave Estimated Green Function (EGF) section for all 3 396 station pairs band-pass filtered between 10 and 100 s.

phase velocities than EQ. Magrini et al. (2022) observed significant differences between the phase velocities from AN and EQ data at periods > 50 s and this could be explained by the difficulty of AN to produce robust measurements at periods above the primary microseism band, i.e. ∼10 to 20 s (Friedrich et al. 1998). At shorter periods, several explanations exist for the observed bias: (1) AN cross-correlations having a low signal-to-noise ratio (Kästle et al. 2016); (2) Wave propagation path deviations between source and receivers caused by heterogeneities in the subsurface (Magrini et al. 2020); (3) Overtone contamination (Soomro et al. 2016); and (4) Differences in the sensitivity kernels (Fichtner et al. 2017). Magrini et al. (2022) also observed, at periods < 15 s, that the AN and EQ phase velocities differences increased significantly.

To resolve the dataset integration problem, we followed the correction method of Timkó et al. (2022), based on Magrini et al. (2022). First, the discrepancy between those datasets was computed by matching the dispersion curves for the same pairs of stations. 566 common

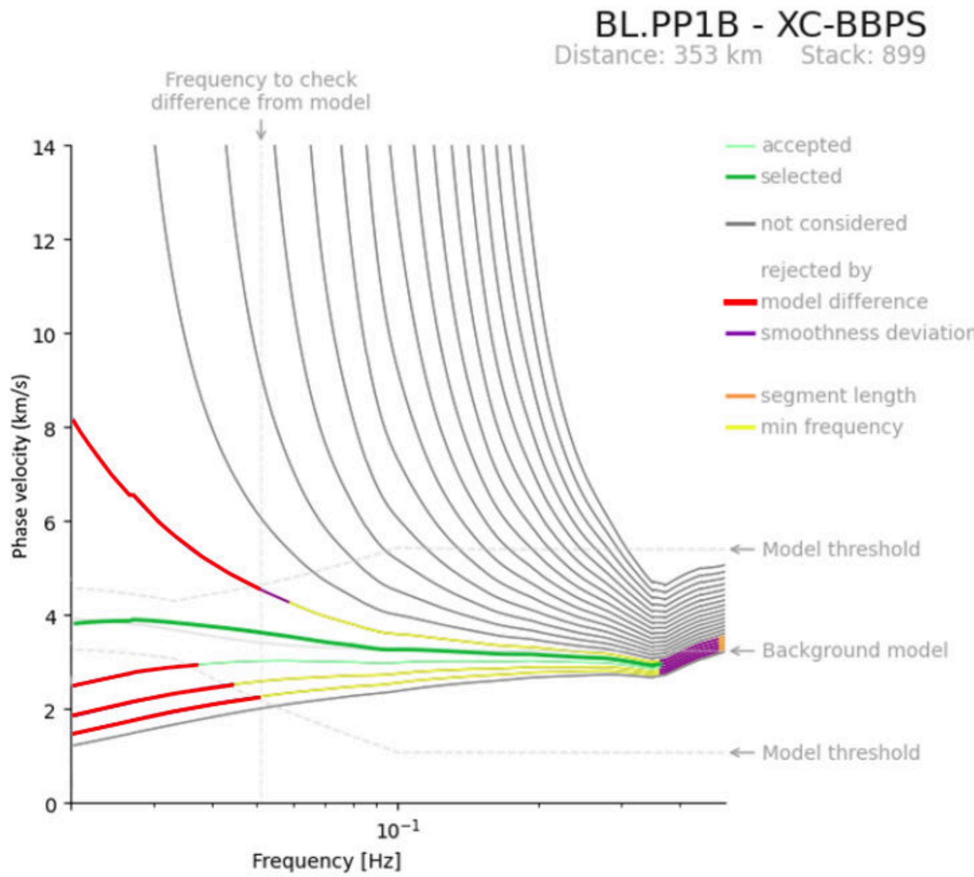

Fig. 28: Selection of the phase-velocity multiples for the station pair PP1B and BBPS. Curves were selected according to the following criteria: (1) distance from a background model (gray and1 red curves) falls within a certain threshold (gray dashed curves); (2) smoothness of each multiple (purple segments); (3) segment length (orange); (4) and minimum required frequency (yellow) calculated as a distance-dependent threshold. The thick green line is the final selected dispersion curve segment.

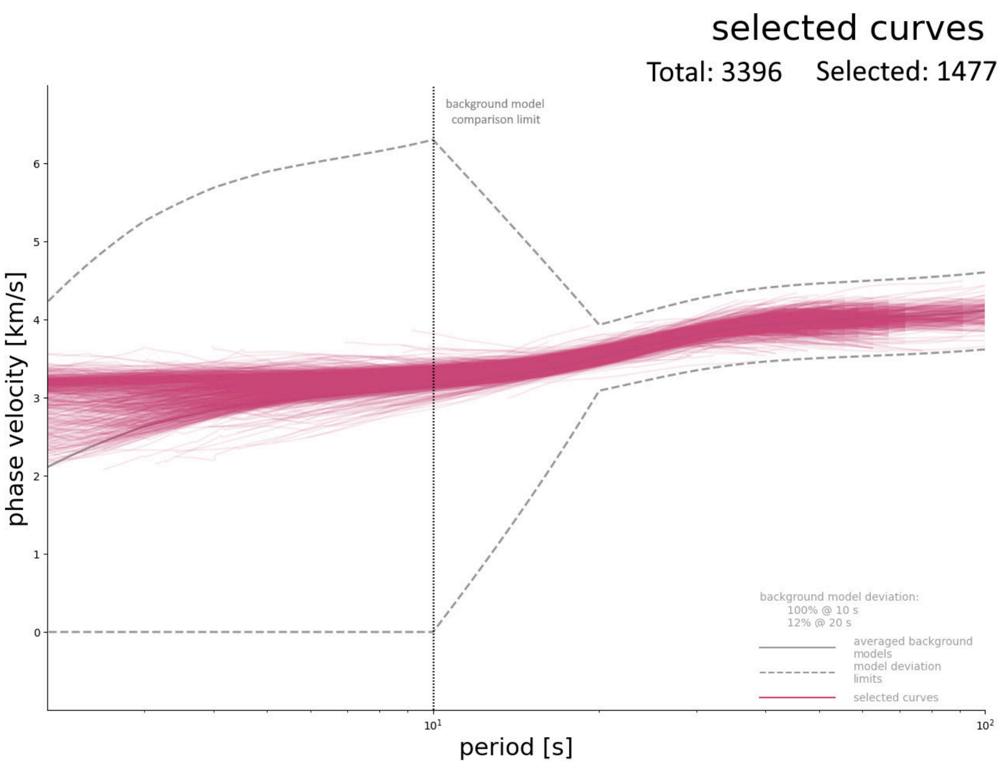

Fig. 29: The 1,477 selected (pink lines) phase-velocity dispersion curves. The thresholds for the background model deviation are shown in the lower right. The average background model for all curves is shown as a gray line with an associated deviation threshold (dashed gray line). The comparison with a background model stops below 10 s (vertical dashed line).

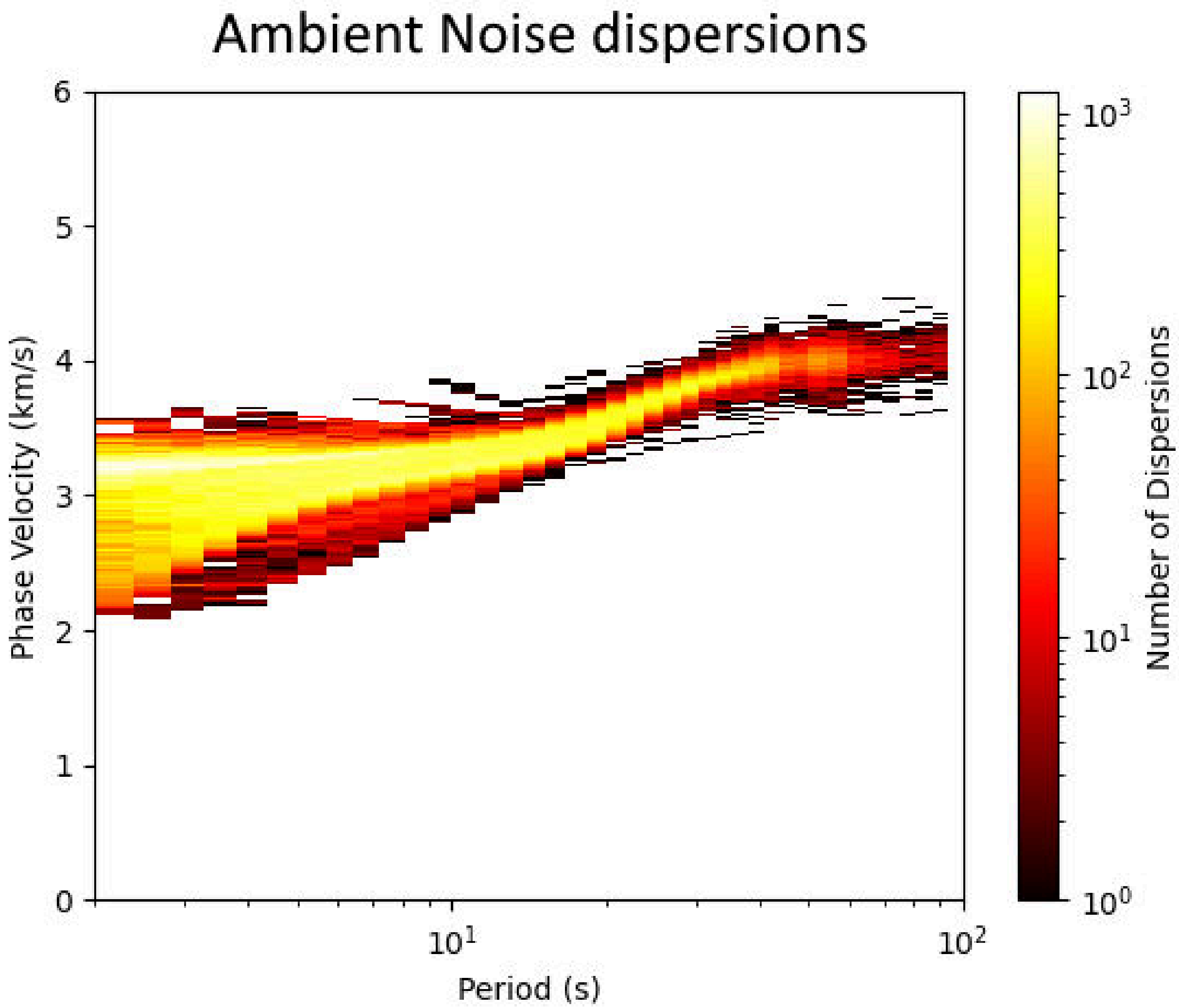

Fig. 30: Hitcount graph for the 1,477 final selected dispersion curves.

paths were selected (∼38% of the AN dataset). Then, the differences between AN and EQ dispersion curves were taken as a function of the period. Fig. 31A shows histograms of those differences for 8, 10, 15, 25, 50 and 60 s before the correction. The histogram median is around ∼-1% for all the periods, confirming the AN negative bias mentioned before. To fix this bias, we implemented a weighted function based on Magrini et al. (2022) (bottom graph in Fig. 32). The correction factors for AN and EQ dispersion curves are computed as follows:

1. Calculate the average difference for each period between AN and EQ dispersion curves for the common paths (dashed orange line in Fig. 32);
2. Smoothing is applied to the difference curve from the previous step (blue curve in Fig. 32);
3. The AN correction factor (pink curve in Fig. 32) is calculated by multiplying the smoothed curve, ω, with the weight function μ (blue line in Fig. 32 bottom graph);
4. The EQ correction factor (yellow curve in Fig. 32) is calculated by $\omega \times (\mu - 1)$;
5. Those differences are removed from the original dispersion curves;

After the correction was applied, we observed that the AN negative bias was removed for all periods (Fig. 31B). Examples of the corrected and final dispersion curves are shown in Fig. 33. We observed a good agreement between both types of dispersion curves for all periods and all areas.

7.2 Isotropic and anisotropic phase-velocity inversion

Following the inversion scheme from Sec. 3, we remade the inversion for SSE Brazil using the earthquake and ambient noise dispersion curves obtained after the bias correction (Sec. 7.1) for periods between 2 and 200 s. The same area as the previous phase-velocity inversion was used. However, most differences should be located in SSE Brazil given the

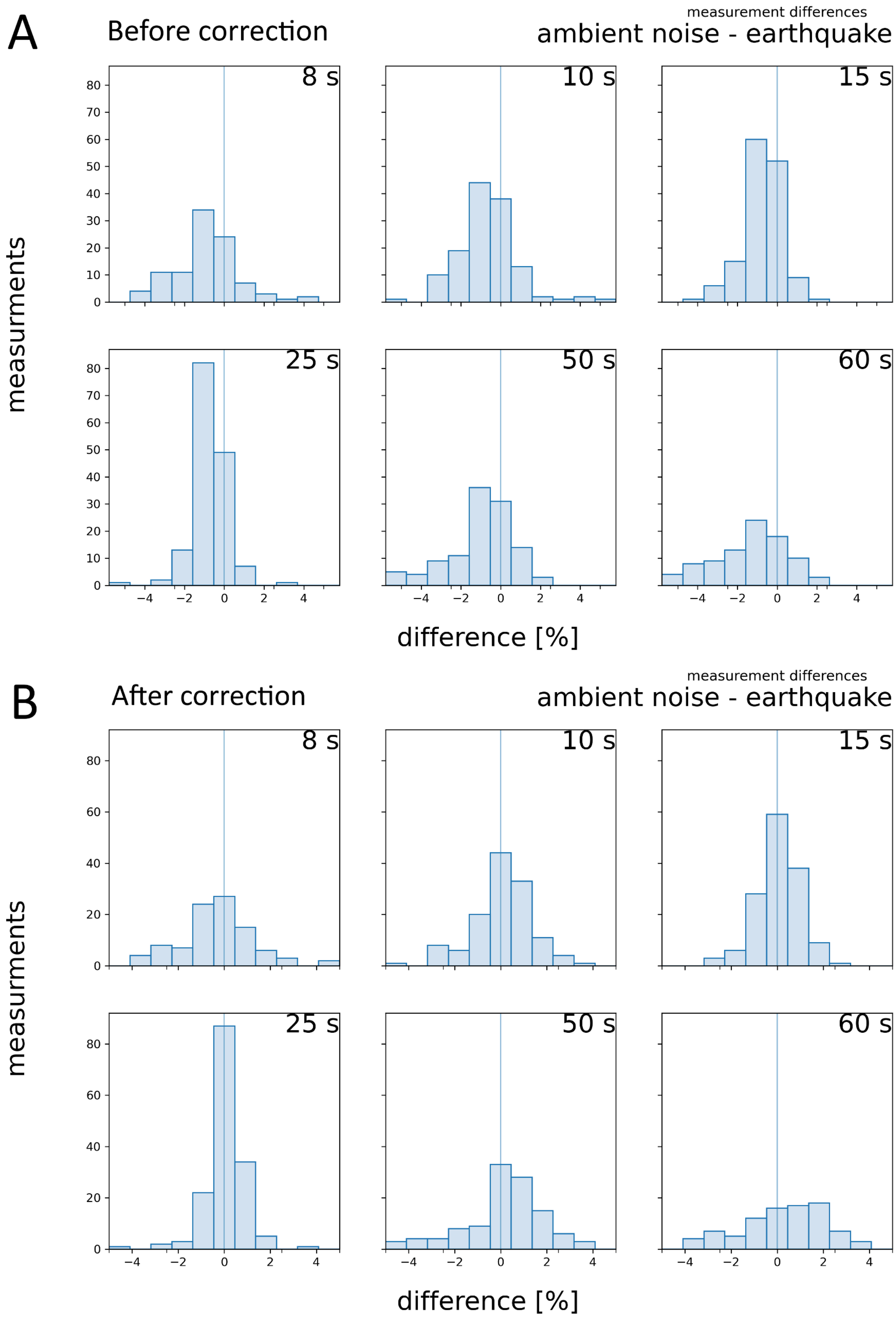

Fig. 31: Histogram of the Earthquake (EQ) and Ambient Noise (AN) phase velocity differences (AN - EQ) for 8, 10, 15, 25, 50 and 60 s. The differences are shown before (A) and after (B) the bias correction.

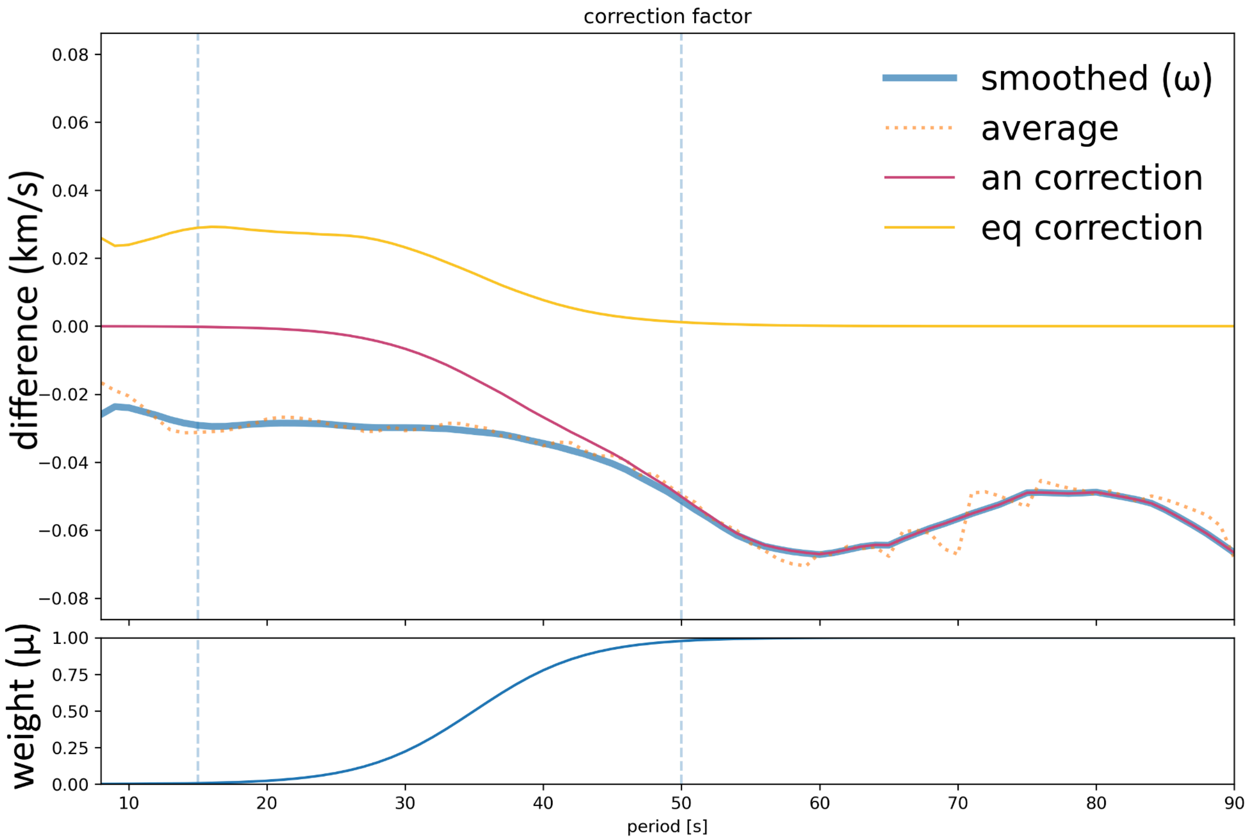

Fig. 32: The top graph shows the average differences between the Ambient Noise and Earthquake datasets (dashed orange), smoothed difference curve (thick blue), calculated correction factors for Ambient Noise (pink) and Earthquake (yellow) datasets. The weighted function used in the calculation of the correction factor is shown at the bottom.

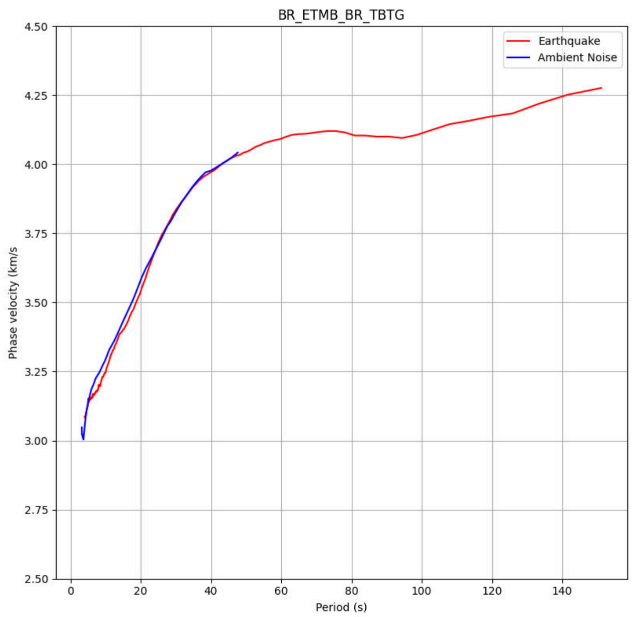
BR_ETMB_BR_TBTG
Earthquake
Ambient Noise
Phase velocity (km/s
Period (s)

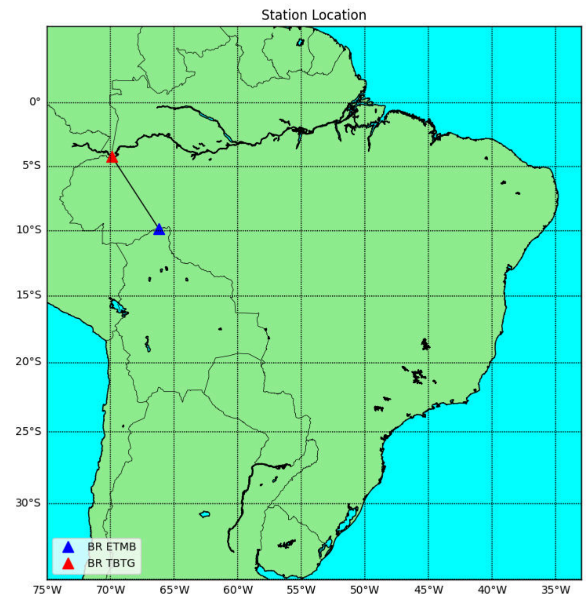
Station Location
BR ETMB
BR TBTG

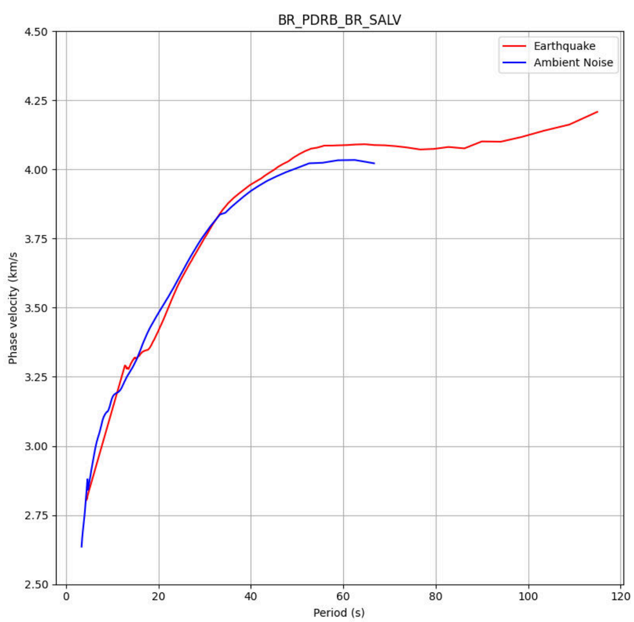
BR_PDRB_BR_SALV
Earthquake
Ambient Noise
Phase velocity (km/s
Period (s)

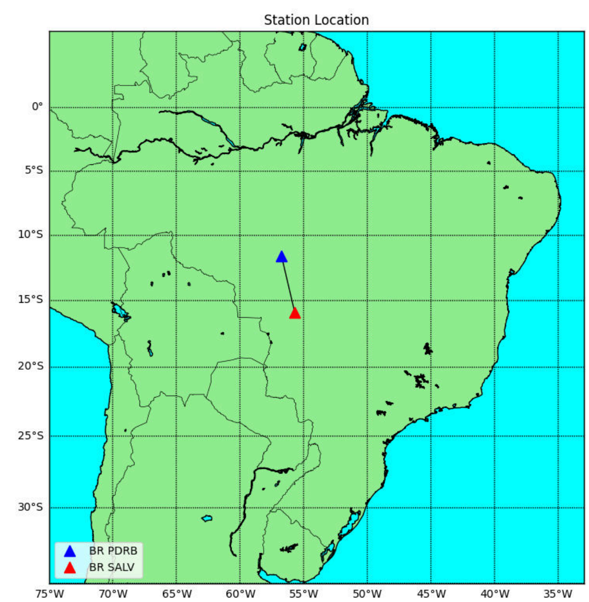
Station Location
BR PDRB
BR SALV

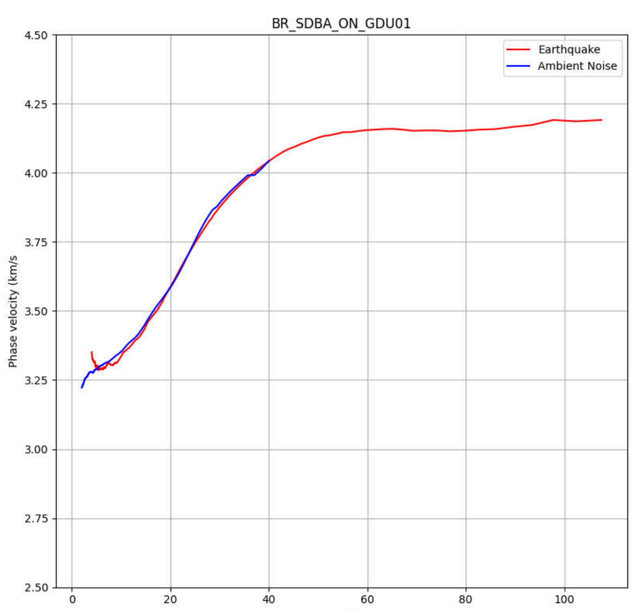
BR_SDBA_ON_GDU01
Earthquake
Ambient Noise
Phase velocity (km/s
Period (s)

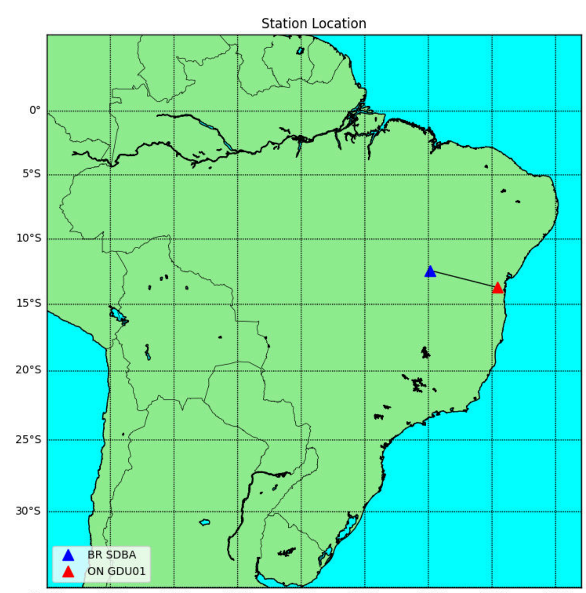
Station Location
BR SDBA
ON GDU01

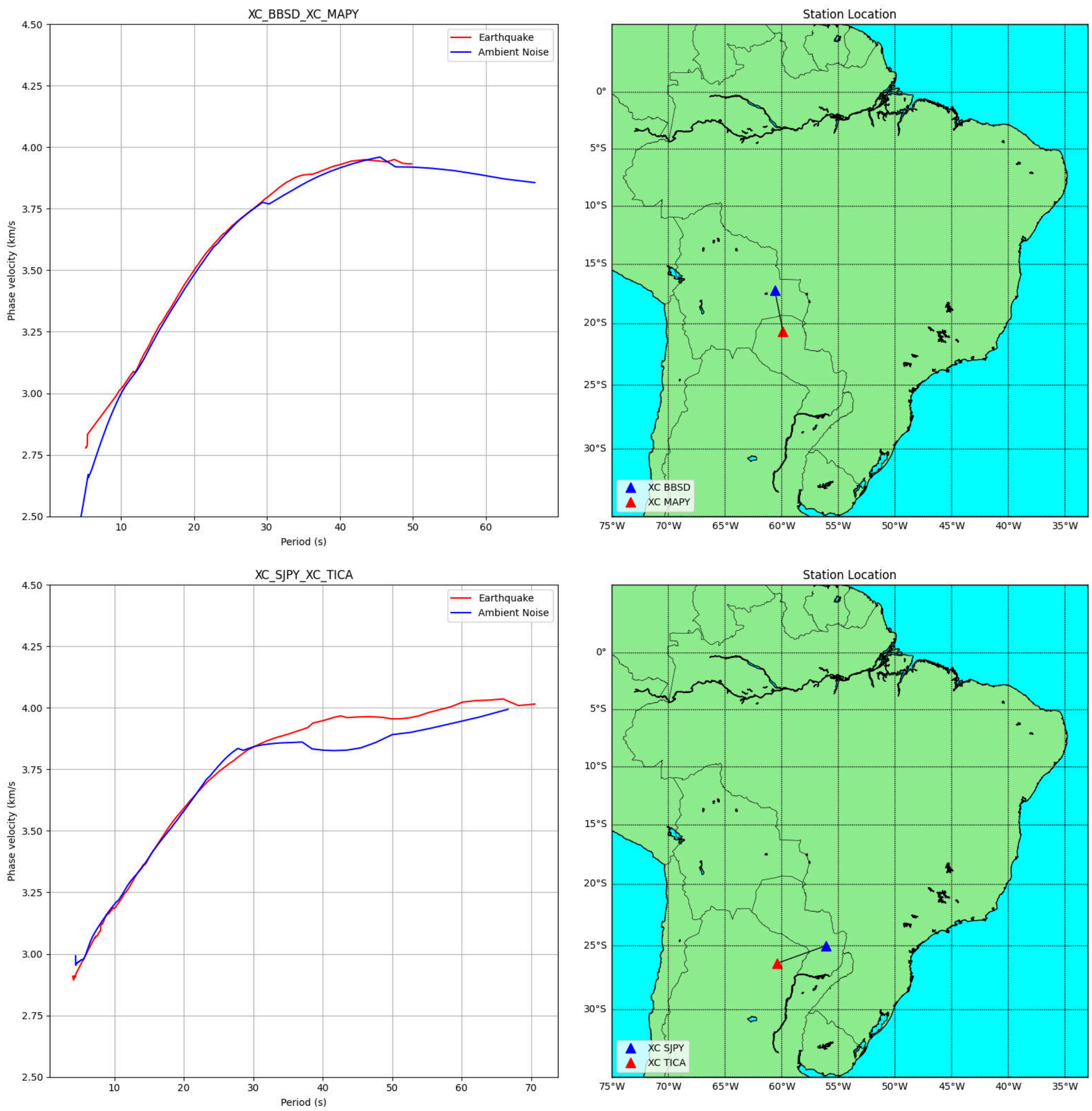

Fig. 33: The left figures are examples of Earthquake (red line) and Ambient Noise (blue line) phase-velocity dispersion curves for different pairs of stations (location map shown on the right).

higher ambient noise ray density (Fig. 25b). Examples for 2, 5, 10 and 20 s are shown in Fig. 34.

8 Discussion - Paper II

8.1 Overview

The periods of 2, 5, 10 and 20 s shown in Fig. 34 were chosen because of the predominance of the microseism band (Friedrich et al. 1998) in ambient noise data, i.e. where dispersion curves derived from ambient noise have the most energy. The periods between 2 and 20 s sample mostly the upper and middle crust, respectively. For all periods, we observe low phase velocities in the Paraná and Chaco-Paraná basins associated with the 7 km thick sedimentary cover of those basins (e.g. Julià et al. 2008; Dragone et al. 2017). A separation between the basins by a shallower basement along the Asunción and Rio Grande arches (roughly along 57°W) follows the results from Shirzad et al. (2020) ambient noise inversion for periods above 5 s. Low velocities are also observed inside the Parecis basin, agreeing with Shirzad et al. (2020) and Nascimento et al. (2022). High-velocity anomalies are seen in shield areas of the Amazon, São Francisco and Rio Apa cratons. For the Pantanal basin, high velocities are observed for periods between 5 and 20 s and are related to the thin (500 m) sedimentary layer (Catto 1975; Weyler 1962). For the 2 s inversion, inside the Pantanal basin, higher phase velocities are observed in the western part of of the basin in relation to the eastern. This difference agrees with the joint inversion of Receiver Function, surface waves and H/V data by Moraes and Assumpção (2022), indicating that Pantanal basin basement is shallower in the west.

As mentioned in Sec. 1.3, most of the anisotropy in South America has been studied with SWS and geodynamic models (e.g. Melo et al. 2018; Assumpcao et al. 2011; Heintz et al. 2003; Assumpção et al. 2006; Russo and Silver 1994; James and Assumpção 1996; Polet et al. 2000; Krüger et al. 2002; Anderson et al. 2004; Piñero-Feliciangeli and Kendall

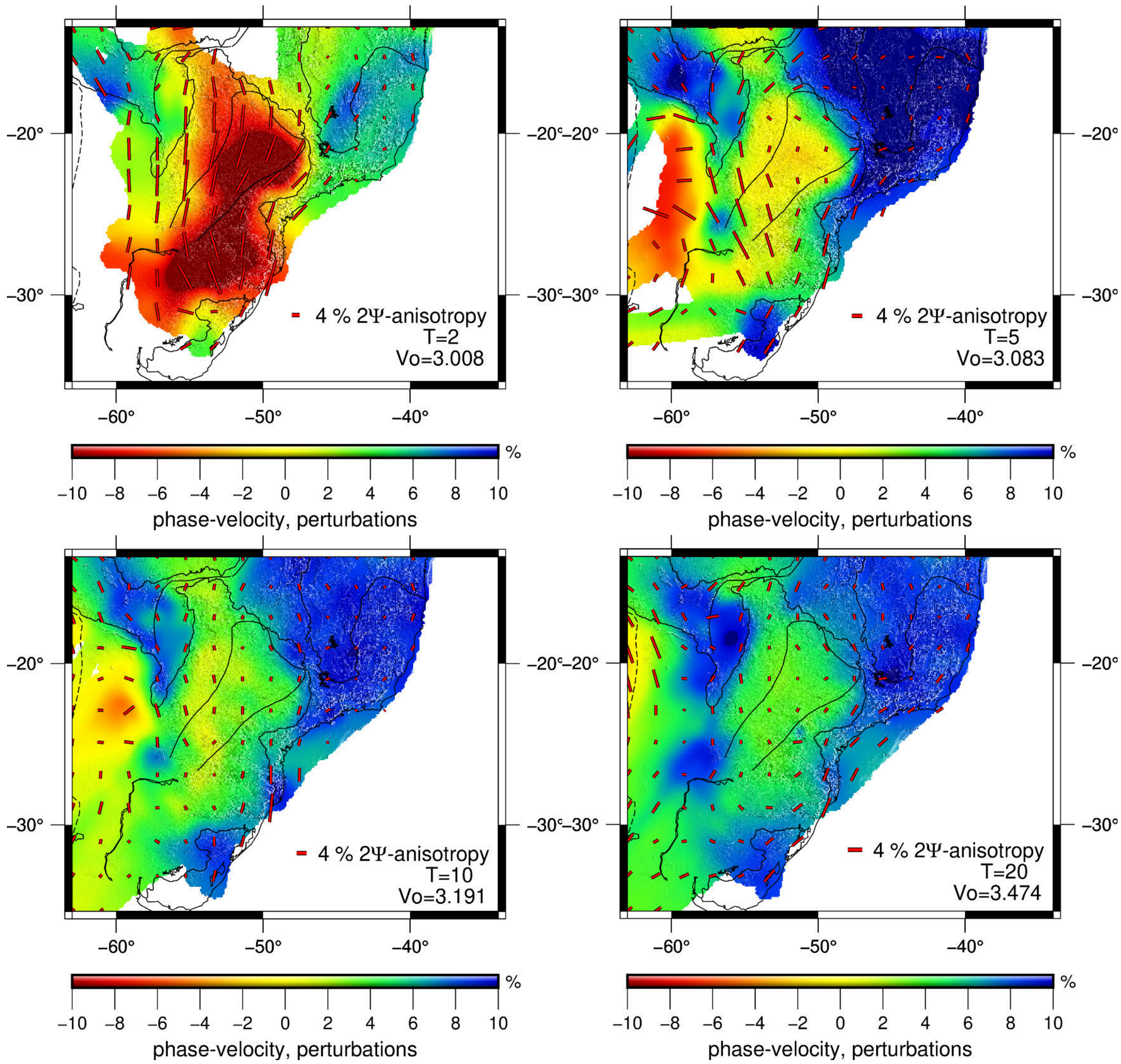

Fig. 34: Rayleigh-wave phase-velocity maps for the earthquake and ambient noise integrated datasets for the periods 2, 5, 10 and 20 s. The percentiles of phase-velocity perturbations are plotted in relation to the average velocity for each period (Vo on the top right of each map). The red bars indicate the direction of fast propagation for the azimuthal anisotropy with a reference scale of 4% amplitude on the top right of each figure. The black outlines are the main tectonic units of South America.

2008; Growdon et al. 2009; Masy et al. 2009; Poveda et al. 2023; Hu et al. 2017). The SWS anisotropy can be mainly related to upper mantle fossil anisotropy due to tectonic processes or present-day asthenospheric mantle flow (Silver and Chan 1991; Silver 1996; Vinnik et al. 1992), which makes a direct comparison of SWS anisotropies with azimuthal anisotropy studies not straightforward. Few recent studies were able to derive azimuthal anisotropy for the area (Poveda et al. 2023; Shirzad et al. 2024) and those can be compared directly with the anisotropies computed in this work. *Pms* splitting was analyzed by Feng et al. (2024), where the time of P-to-S converted phases from Receiver Functions with different back azimuths was observed to vary slightly and can be used to compute an average anisotropy for the crust. The observed dependence of fast *Pms* direction may be similar to our azimuthal anisotropy measurements depending on the origin of the anisotropy. The following comparisons were made with the combined of ambient noise and earthquake dataset (Fig. 34).

8.2 Azimuthal anisotropy comparison with Shirzad et al. (2024)

For crustal periods (5 and 20 s in Fig. 35), the azimuthal anisotropy in SSE Brazil shows fast directions oriented mostly N-S (Fig. 34) with a tendency of being NE-SW north of the Pantanal basin and NW-SE to the south of it. This pattern follows the Paraguay fold belt trend beneath the basin. These results agree with the azimuthal anisotropies from Shirzad et al. (2024) derived from ambient noise. Thus, our results agree with the hypothesis of Shirzad et al. (2024), where the observed pattern could be due to the collision between the Paranapanema, Rio Apa and Amazon cratons during the assemblage of West Gondwana in the Neoproterozoic.

For longer periods sampling the upper mantle (e.g. 60 and 70 s in Fig. 35), our model disagrees with the predominantly N-S anisotropy direction of Shirzad et al. (2024) in the center of Paraná basin (around 20°S). Our model shows a predominantly E-W trend. Along 23°S, Shirzad et al. (2024) show a small region with E-W fast directions that correlate well with our anisotropies. Our model starts to show the change to NE-SW fast direction in the north of the Pantanal basin, as previously discussed in Sec. 6.4, and it seems to have a weak correlation with Shirzad et al. (2024) anisotropies in this area. Beneath 100 km depth, our E-W anisotropies agree better with global S-wave anisotropy from Debayle et al. (2016) and SWS (Melo et al. 2018) and are interpreted as the asthenospheric mantle flow from the Nazca plate subduction guided by LAB topography.

8.3 Azimuthal anisotropy comparison with Feng et al. (2024)

The *Pms* splitting anisotropy from Feng et al. (2024) correspond to an average of crustal anisotropies. To improve the comparison, we averaged our anisotropies between 10 and 30 s for each grid point within a 2.5° radius. Fig. 36 shows a comparison between both works.

Inside the Paraná basin, Feng et al. (2024) show fast E-W anisotropies, while our work shows the trend is mainly N-S in the crust. Feng et al. (2024) N-S trend is interpreted as being related to a synchronous crust-mantle deformation during the breakup of West Gondwana, resulting from the magmatism that formed the Paraná-Etendeka Large Igneous Province. As discussed, our results agree better with Shirzad et al. (2024) and our N-S fast orientations could be explained by cratonic collision in this area (Sec. 8.2). Feng et al. (2024) also interpret the NE-SW trend of anisotropies parallel to the TBL strike and could be formed by dynamic metamorphism during the TBL formation. Our model does not show this pattern, especially inside the Parnaíba basin. In the Mantiqueira fold belt, NE-SW fast direction anisotropies are observed by Feng et al. (2024). An interpretation from Feng et al. (2024) is that the NE-SW trend in Mantiqueira fold belt could be related to extensional crustal fabrics from the West Gondwana rifting. Our fast directions run parallel to the coast and along the large scale shear zone along the Ribeira belt. The strong SKS anisotropy along the Ribeira belt has been interpreted as due to superposition of mantle and crustal anisotropies (Heintz et al. 2003). Our observations of the average crustal anisotropies agrees with that interpretation.

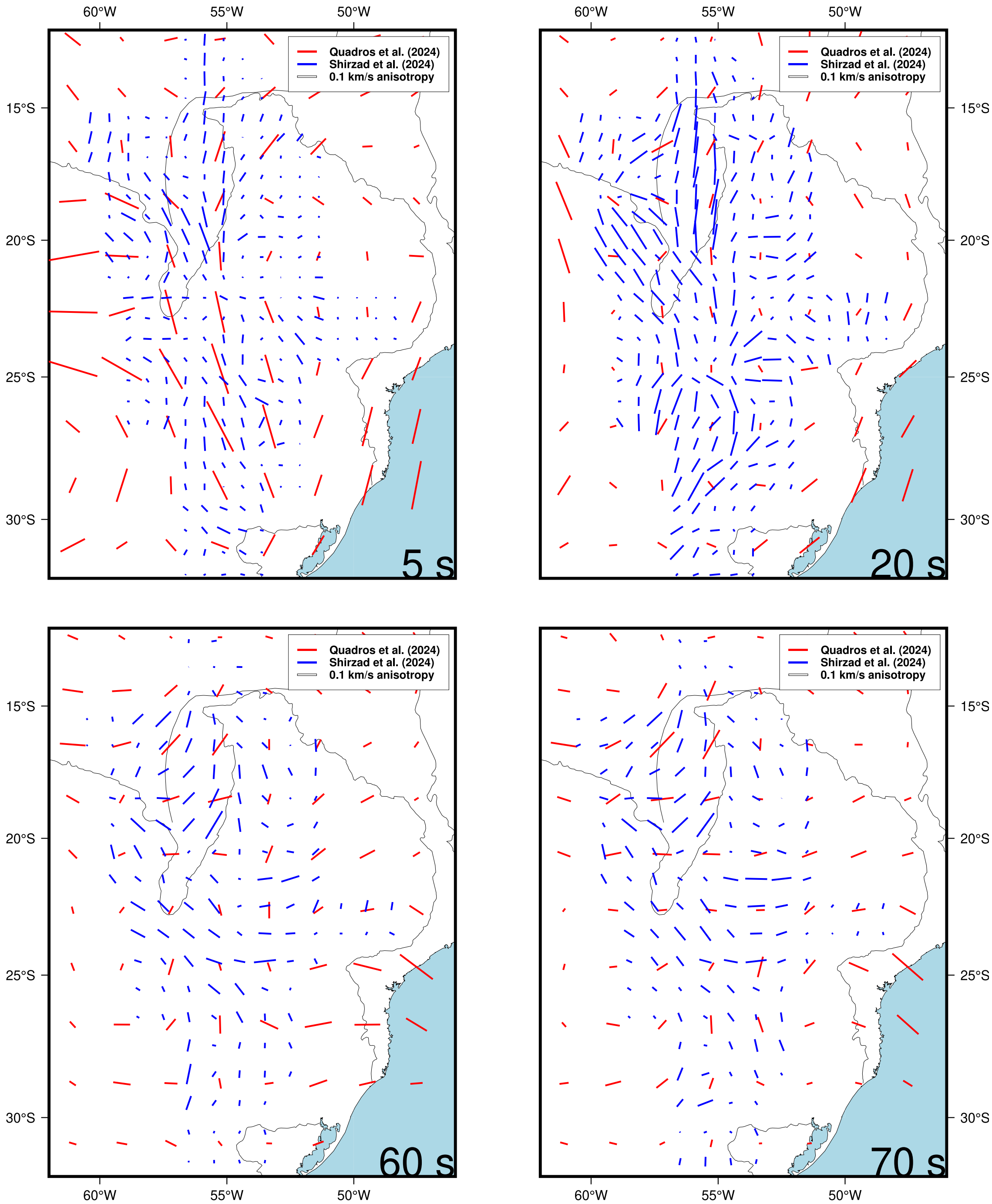

Fig. 35: Azimuthal anisotropy comparison between this work's integrated dataset (red bars) and Shirzad et al. (2024) (blue bars). The top right legend shows the reference bar for 0.1 km/s anisotropy.

Boness and Zoback (2006) categorize the upper-crust anisotropy into two major groups: (1) stress-induced anisotropy due to an anisotropic tectonic state. In a medium with aligned microcracks, vertically propagating seismic waves will have a fast direction anisotropy parallel to the open microcracks (Crampin 1987). For a fractured crust, the fast polarization directions of the vertically propagating seismic waves will be perpendicular to the closure of the fractures (Boness and Zoback 2004). (2) structural anisotropy due to the alignment of planar features, such as macroscopic fractures, parallel sedimentary bedding planes and mineral alignment (e.g. Mueller 1991; Hornby 1998). This differs from the mantle, where the major source of anisotropy is lattice preferred orientation of crystals such as olivine (e.g. Ismail and Mainprice 1998).

The disagreements in most areas with Feng et al. (2024) could be due to the different sources of anisotropy in the upper crust. This is because the Rayleigh-wave phase-velocities are primarily dependent on the vertical polarized shear-wave velocities propagating along a horizontal path, while the P-to-S phase measured by Feng et al. (2024) is primarily dependent on horizontal polarized shear-wave velocities propagating along a mostly vertical path. The difference in polarization between the studies could originate from different sources in the upper crust that affect each azimuthal anisotropy measurement differently depending on which mechanism is predominant in each area.

8.4 Azimuthal anisotropy comparison with Poveda et al. (2023)

Poveda et al. (2023) computed a radial and azimuthal anisotropy map in NW South America from surface waves. They presented group-velocity isotropic and anisotropic maps between 7 and 170 s. The short periods, between 7 to 35 s, were estimated using ambient noise data, while the longer periods (40 to 170 s), were estimated using earthquakes.

Continental-scale works tend to impose strong regularization in such a way as to produce a smoother result across different tectonic areas. This can cause the azimuthal anisotropies

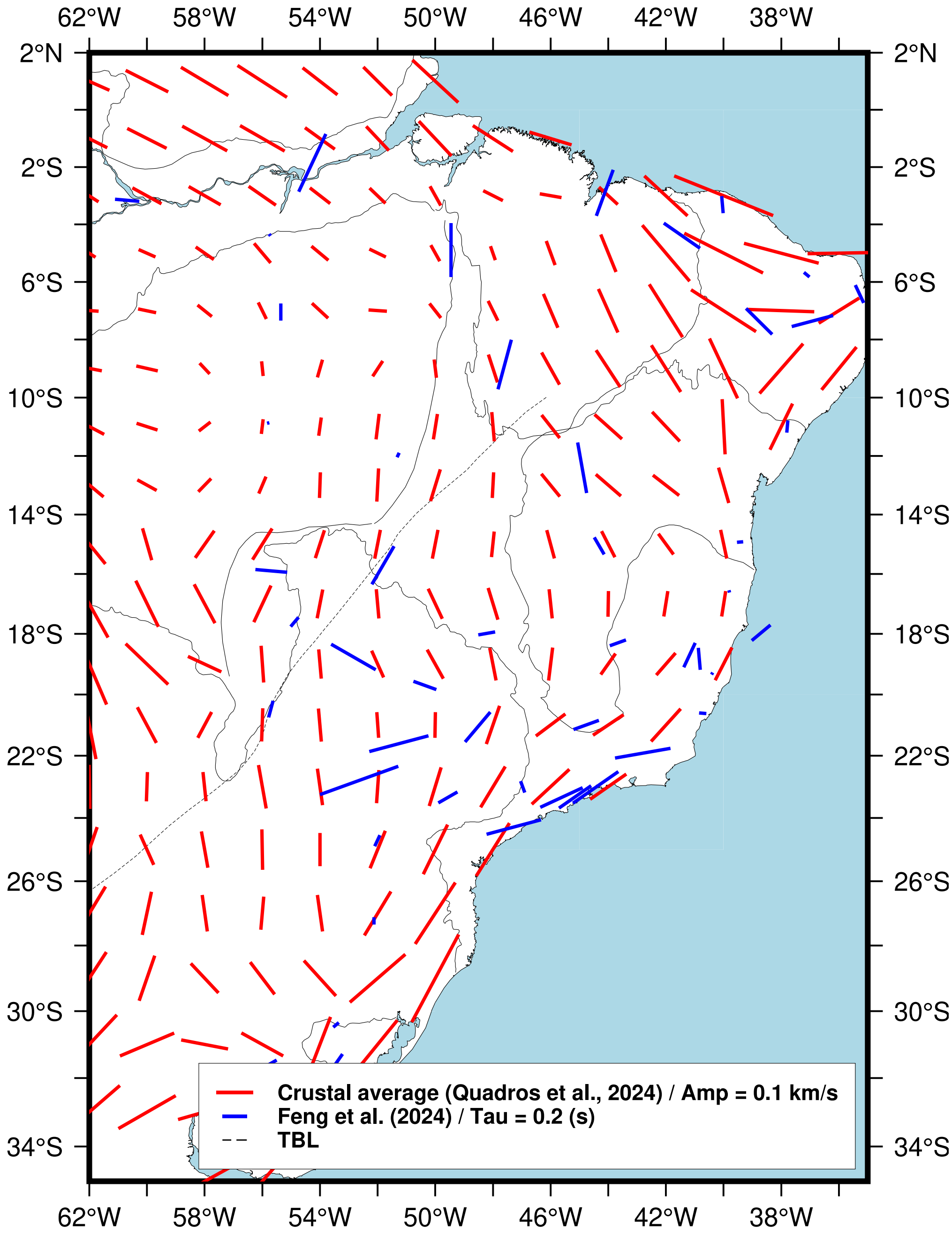

Fig. 36: Comparison between this work integrated dataset average crustal azimuthal anisotropies (red bars) and *Pms* splitting anisotropies from Feng et al. (2024). The red bar size corresponds to a scale of 0.1 km/s and the blue bar size corresponds to a P-to-S conversion delay of 0.2 s. The Transbrasiliano Lineament (TBL) is shown as a dashed line.

amplitudes to be more strongly attenuated in a region with relation to regional works. Fig. 37 shows the average anisotropies amplitudes between this work's integrated dataset (solid red line) and Poveda et al. (2023) model (solid blue line). Our work's average anisotropy amplitude across all periods is around 0.1 km/s, while Poveda et al. (2023) is around 0.18 km/s. To compensate for this effect, we used this result to scale up our model anisotropies amplitudes by a factor of 1.8. The comparison with Poveda et al. (2023) can be seen in Fig. 38 for 25 and 70 s.

For shorter periods (e.g. 25 s in Fig. 38), both models have a good agreement. Our results confirm the observations by Poveda et al. (2023) of fast-direction anisotropies perpendicular to the trench that are consistent with the movement of the South American plate in relation to the Nazca plate. Poveda et al. (2023) point out that this observed anisotropy can be due to the interaction between the descending plate and the upper asthenospheric mantle. The observed anisotropy can be due to mantle wedge flow or alignment of cracks along the subduction direction (Legendre et al. 2021; Long and Silver 2008). We also observe an N-S trend east of the Andes and a trench parallel fast axis in the Caribbean. There is no clear interpretation for those last two.

For longer periods (e.g. 70 s in Fig. 38), both model's anisotropies tend to disagree. At 70 s, Poveda et al. (2023) observed a rotation to N-S (blue line) of the fast axis parallel to the trench, which is challenging to explain. Our model (red line) shows an E-W fast axis consistent with mantle wedge flow in the region. Poveda et al. (2023) commented that mechanisms, such as slab rollback, oblique subduction and water-rich olivine deformation, could explain an N-S trend. This disagreement in the longer periods could be explained by: (1) azimuthal anisotropies calculated from group and phase-velocities have different sensitivity kernels; and (2) our model tends to have poorer resolution along the Andean region for longer periods, as shown during the checkerboard tests (Sec. 3.2).

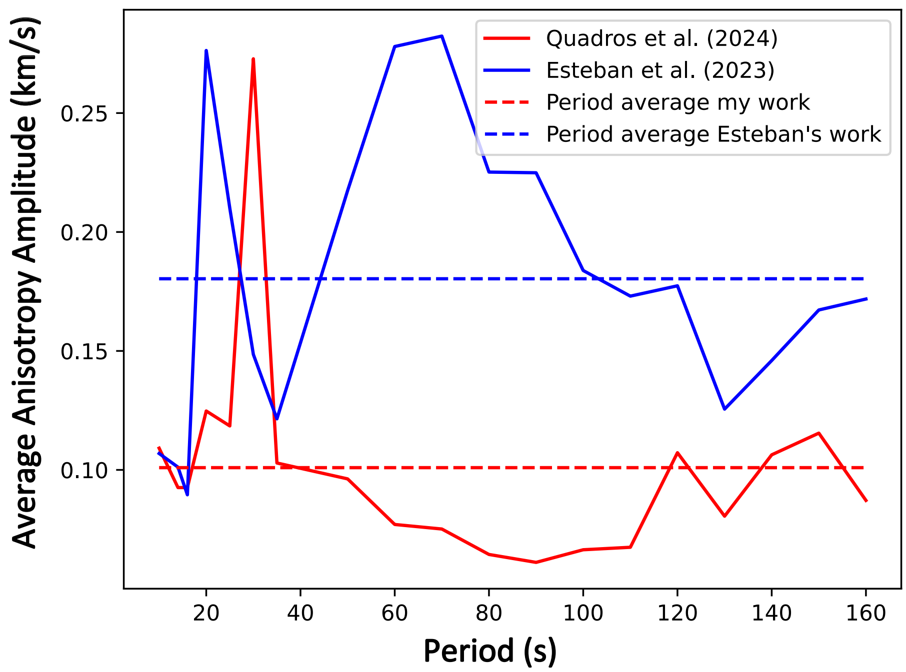

Fig. 37: Average anisotropy amplitude comparison between our integrated model (solid red line) and Poveda et al. (2023) (solid blue line) as a function of the period. The averages across all periods are shown as dashed lines for our model (around 0.1 km/s) and Poveda et al. (2023) (around 0.18 km/s).

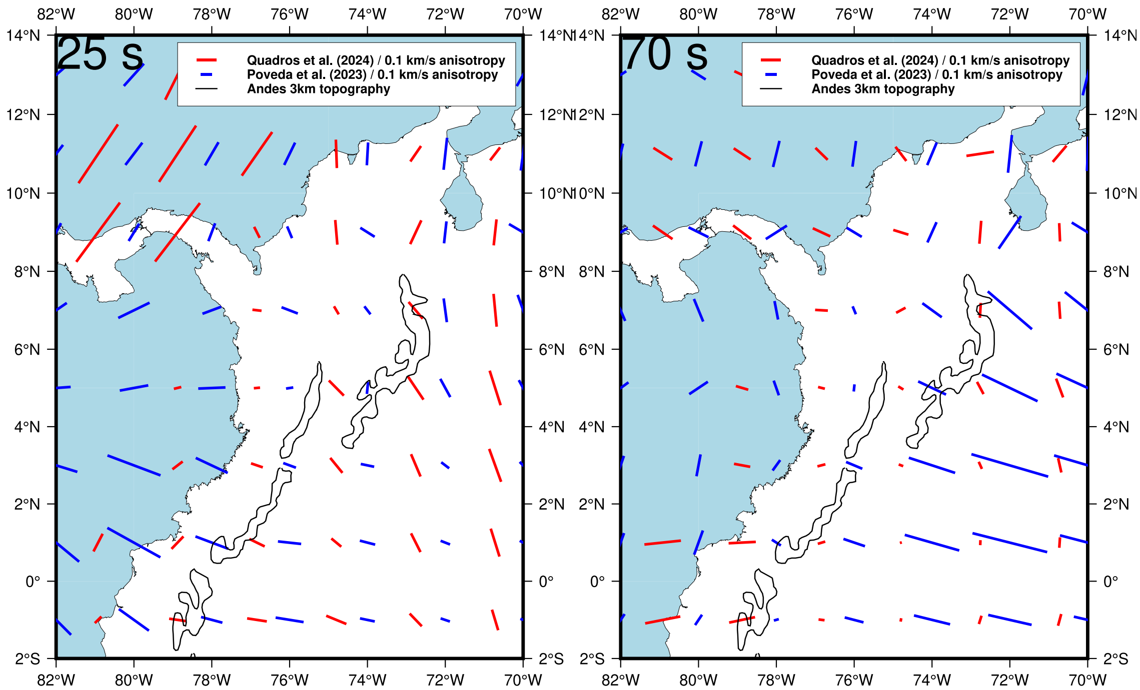

Fig. 38: Azimuthal anisotropy fast direction comparison between our integrated model (red line) and Poveda et al. (2023) (blue line) for 25 and 70 s. Our anisotropies amplitudes were increased by a factor of 1.8 following Fig. 37 results to compensate for differences in each work's scale (continental vs regional). The 3 km topography of the Andes is shown as a black line.

9 Conclusion

For the first study, we presented Rayleigh-wave phase-velocity maps for periods between 5 and 200 s for isotropic and anisotropic components (Fig. 13). We used an automatic implementation of the two-station method to automatically compute and apply quality control to dispersion curves throughout South America (Soomro et al. 2016). This method allowed measurements across a broader range of periods than previous works (Feng et al. 2004; Rosa et al. 2016; Lee et al. 2001; Heintz et al. 2005; Feng et al. 2007; Nascimento et al. 2022). We also used the isotropic component to invert a 3-D shear-wave velocity model between 15 and 300 km (Fig. 22) following a particle-swarm-optimization technique by El-Sharkawy et al. (2020). We also derived a Moho map for South America from this last inversion (Fig. 23) that showed good agreement with the crustal thickness map from Rivadeneyra-Vera et al. (2019) and can help complement the Moho thickness data in areas of poor station coverage for Receiver Function studies.

The lithospheric anisotropy has been studied with SKS in the South American Platform (Melo et al. 2018; Assumpcao et al. 2011; Assumpção et al. 2006). However, such studies have difficulty observing large-scale trends in the anisotropy, given the poor coverage of seismographic stations inside the South American Platform. We were able to compute the anisotropies in areas of previously poor coverage, such as the Amazonian Basin, Amazon Craton and Pantanal Basin. For the 15 and 30 s (Fig. 13) maps, we observed the azimuthal anisotropy fast direction being parallel to the strike of the Andean Orogeny, which is consistent with the observed compression of the South American Plate from the subduction of the Nazca Slab (e.g. Assumpção et al. 2016). For 100 s (Fig. 13), the anisotropy fast direction shows an E-W trend just east of the Andes, parallel to the motion of the Nazca Plate relative to the South American Plate (Gripp and Gordon 2002). A change to NE-SW trend, following the low-velocity anomaly under the Pantanal Basin (e.g. $\sim$4% V_{SV} in Fig. 22 at 100 km), is observed and it is consistent with mantle flow deflected by the Paranapanema cratonic root. However, we do not observe the NW-SE directions south of the Paranapanema block, as observed by Melo et al. (2018) and Assumpcao et al. (2011).

We observed systematic differences between the Guyana Shield and Central Brazil Shield (e.g. Fig. 22 at 100 km) that were constant across different depths (Fig. 24A-A' and Fig. A5. Our model indicates that, on average, the Guyana Shield has lower shear-wave velocities than the Central Brazil Shield (difference of $\sim 3\%$ V_{SV}). This difference could be due to some rework of the lithospheric root of the Guyana Shield by some magmatic event, such as the Central Atlantic Magmatic Province (CAMP).

We also observed a low crustal and LAB thickness (profile C-C' in Fig. 24) in the Tocantins Province, an area of known high seismicity in Brazil (e.g. Agurto-Detzel et al. 2017). The thin crust was observed previously in seismic refraction profiles (Berrocal et al. 2004) and receiver functions (Assumpção et al. 2013a; Assumpção et al. 2013b; Rivadeneyra-Vera et al. 2019). Assumpção and Sacek (2013) proposed that crustal and lithospheric thinning could contribute to the high seismicity observed in this area by producing higher stresses in the upper crust.

Ambient noise-derived dispersion curves were calculated similarly to the earthquake methodology (Sec. 2). We used 138 seismic stations from 1998 to 2022 from the Brazilian Seismographic Network (Fig. 25) to compute 1,477 ambient noise phase-velocity dispersion curves (Fig. 29). Rayleigh-wave isotropic and anisotropic maps, between periods of 2 and 200 s, were calculated by combining the dispersion curves from the earthquake dataset with ambient noise. We showed examples for 2, 5, 10 and 20 s (Fig. 34). For the isotropic phase velocities, the results show good agreement with previous tomographies in the crust. At 2 s, higher phase velocities are observed to the west of the Pantanal Basin relative to the east. This agrees with a joint inversion of Receiver Function, surface waves and H/V data by Moraes and Assumpção (2022) and indicates that the basin's basement is shallower in the west. For the azimuthal anisotropies and crustal depths (5 to 20 s in Fig. 34), we observed a NE-SW fast axis trend to the north of the Pantanal Basin and NW-SE to the south of it, well correlated with the Paraguay fold belt strike under the basin. At the same depths, N-S fast axis anisotropies were observed mainly inside the Paraná Basin and those could be associated with the collision of the Paranapanema, Rio Apa and Amazonian Cratons during the assemblage of West Gondwana during the Neoproterozoic as mentioned by Shirzad et al. (2024). Fast axis anisotropies parallel to the passive margin in Mantiqueira Province were observed and correlated well with Pms splitting anisotropy inversion for the area (Feng et al. 2024). This result helps confirm the interpretation that crustal and lithospheric anisotropy in the Ribeira belt is due mainly to shear deformation during the Brasiliano orogeny.

10 Appendix A - Additional Figures

Supporting figures are available in this appendix. Those are:

- Rotation tests for the full study area (Fig. A1);
- Uncleaned Rayleigh-wave phase-velocity maps for 15, 30, 60 and 100 s (Fig. A2);
- Additional figures about the V_{SV} inversion for the nodes inside the Amazon craton (Fig. A3) and Pantanal basin (Fig. A4) shown initially in Fig. 21;
- 3D shear wave velocities for South America between 15 to 300km every 25 km (Fig. A5);
- Additional vertical cross-sections throughout our V_{SV} model (Fig. A6).

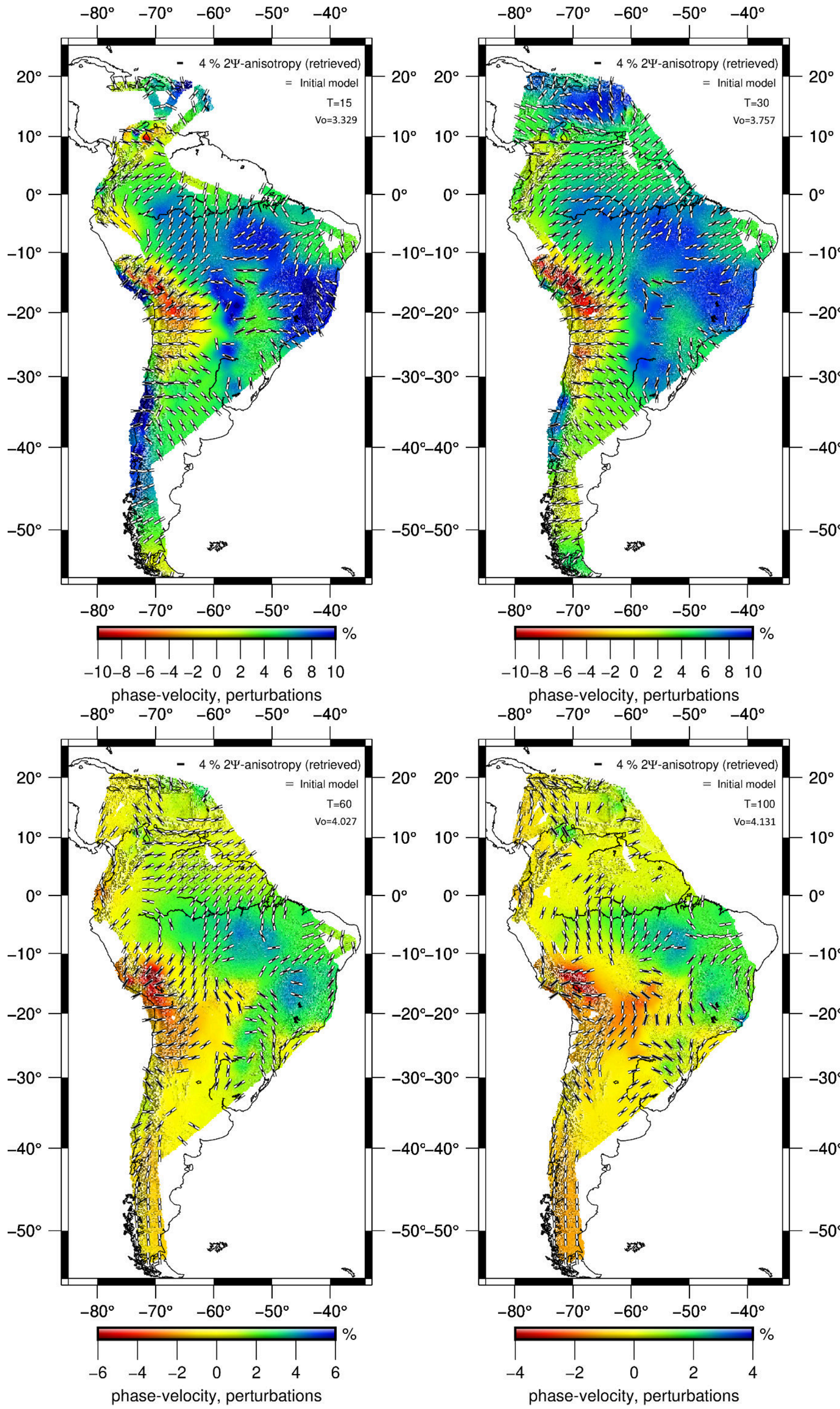

Fig. A1: Rotation test for periods of 15, 30, 60 and 100 s. White bars are the original fast directions rotated 90° that are used as the input for the inversion. The black bars are the results after the inversion with a reference scale of 4% amplitude on the top right of each figure. The background color shows the isotropic perturbations from the original inversion plotted in relation to the average value for each period (V_o on the top right of each map). Regions with no data are places where the original anisotropy amplitude falls below the minimum amplitude threshold (<7.41 m/s), so those nodes were not considered for the rotation test.

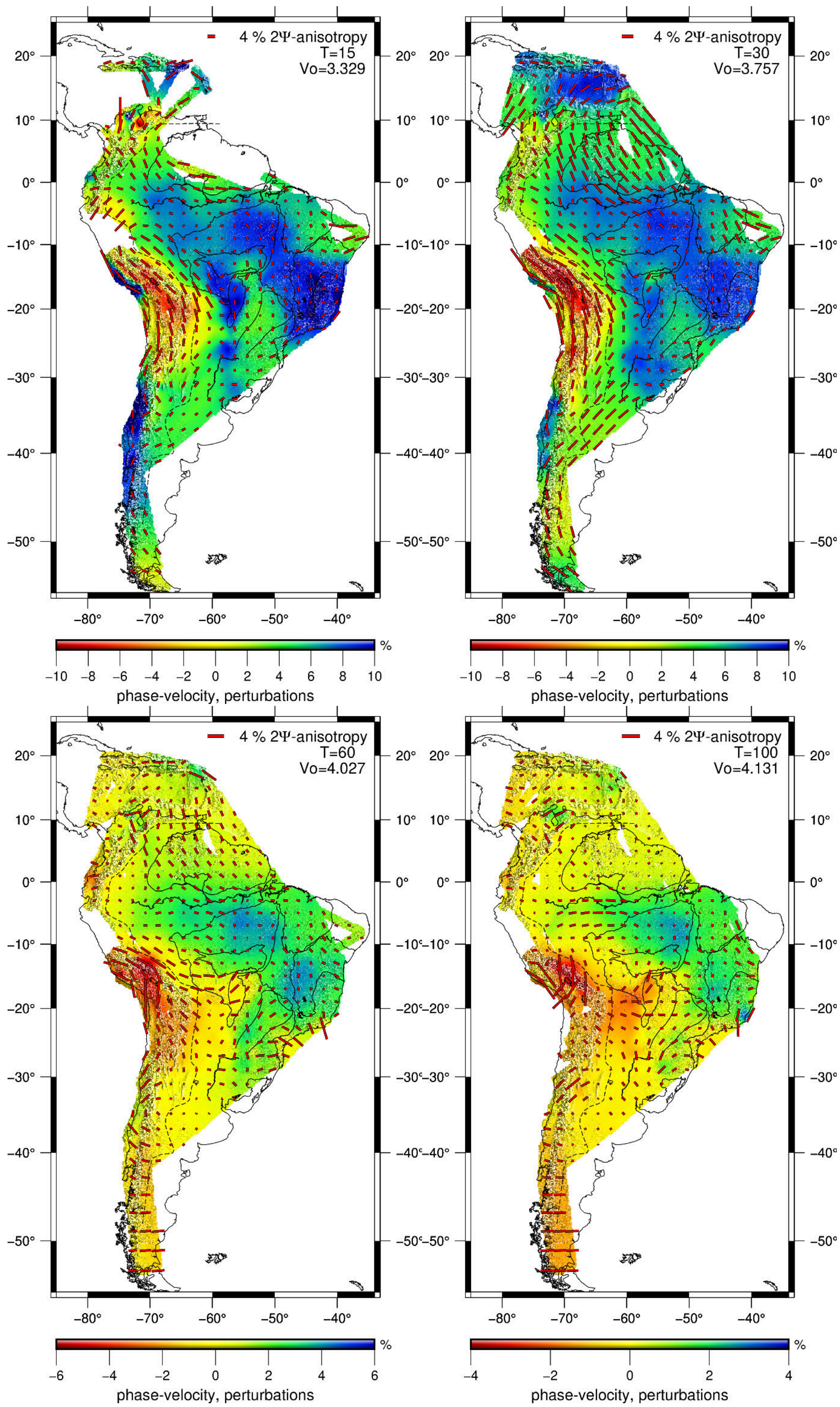

Fig. A2: Uncleaned Rayleigh-wave phase-velocity maps for the isotropic and 2ψ anisotropic components for the periods of 15, 30, 60 and 100 s. The percentiles of phase-velocity perturbations are plotted in relation to the average velocity for each period (Vo on the top right of each map). The red bars indicate the direction of fast propagation for the azimuthal anisotropy with a reference scale of 4% amplitude on the top right of each figure. The black outlines are the main tectonic units of South America.

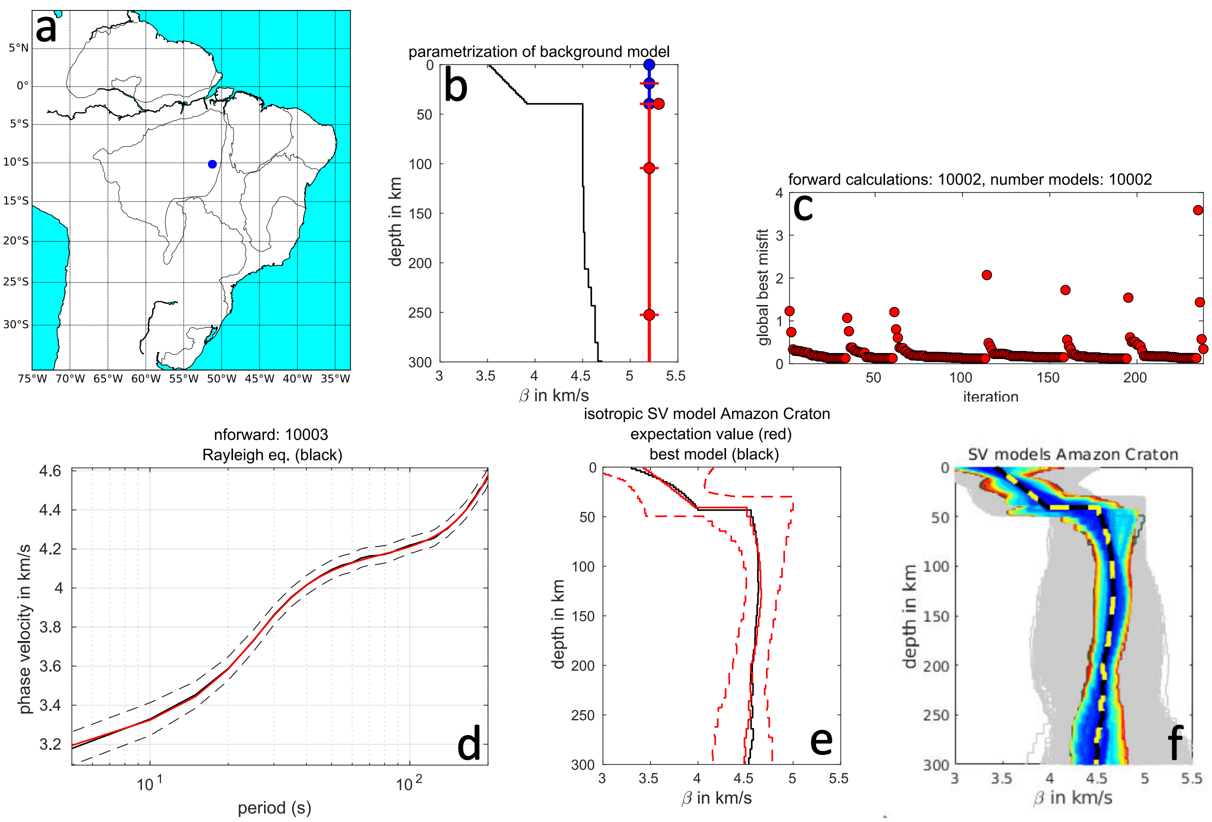

Fig. A3: V_{SV} inversion example for a node inside the Amazon Craton. (a) location of the node. (b) initial background model and its parametrization. The colored lines indicate the order of perturbations for the shear-wave velocity. The blue and red colors indicate quadratic and cubic curvatures, respectively. The colored circles indicate the grid nodes' locations. The lines indicate grid nodes with depth variability enabled. (c) best global misfit for the inversion for each iteration. The jumps in misfits are resets in the inversion random parameter search to try and find better global misfits. (d) In black are the observed local dispersion curve and its standard deviation (dashed). The red line is the best-fitted dispersion curve. (e) final shear-wave velocity models. Best model is in black and the centroid model is in red. The dashed red lines are the models used for calculating the centroid. (f) Gray-shaded areas show the sampled model space, the accepted range of models is plotted in blue and the models are sorted according to their misfit values. The coarse dashed line is the centroid model.

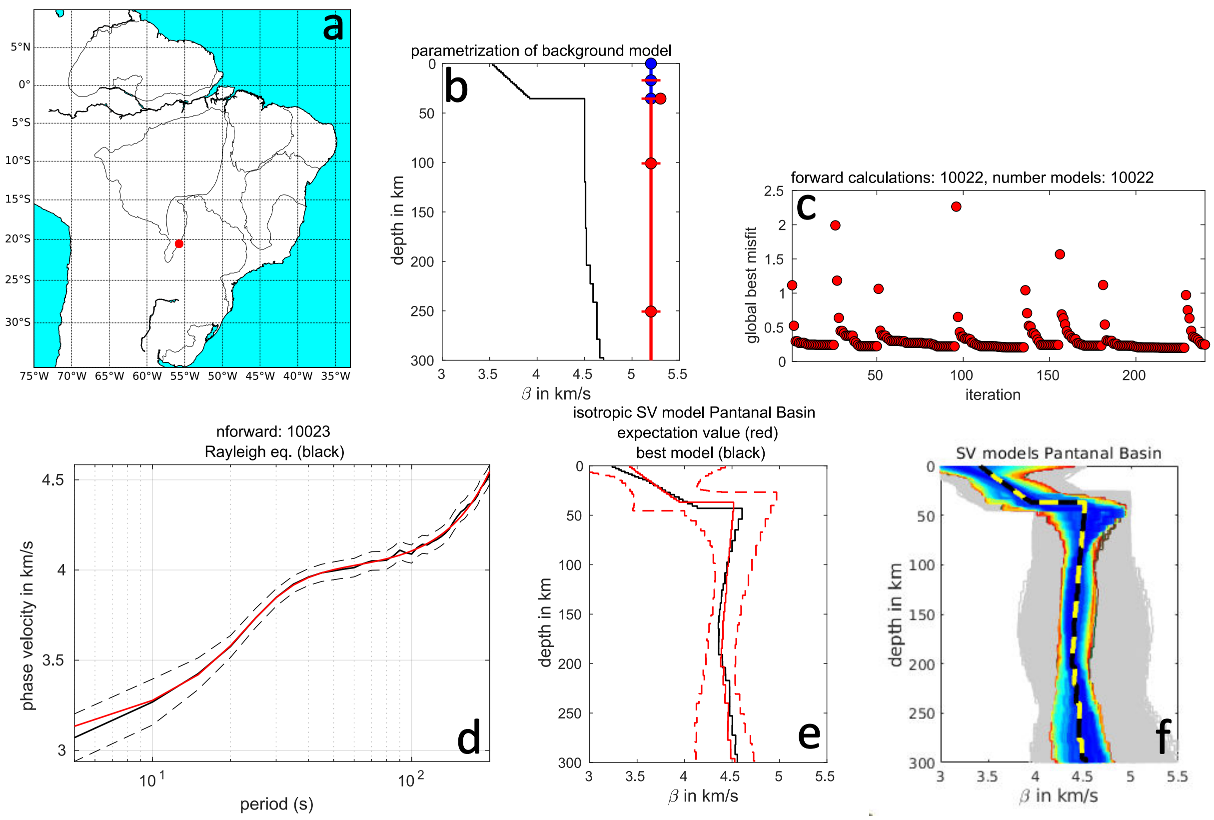

Fig. A4: Same as Fig. A3, but for a node inside the Pantanal Basin.

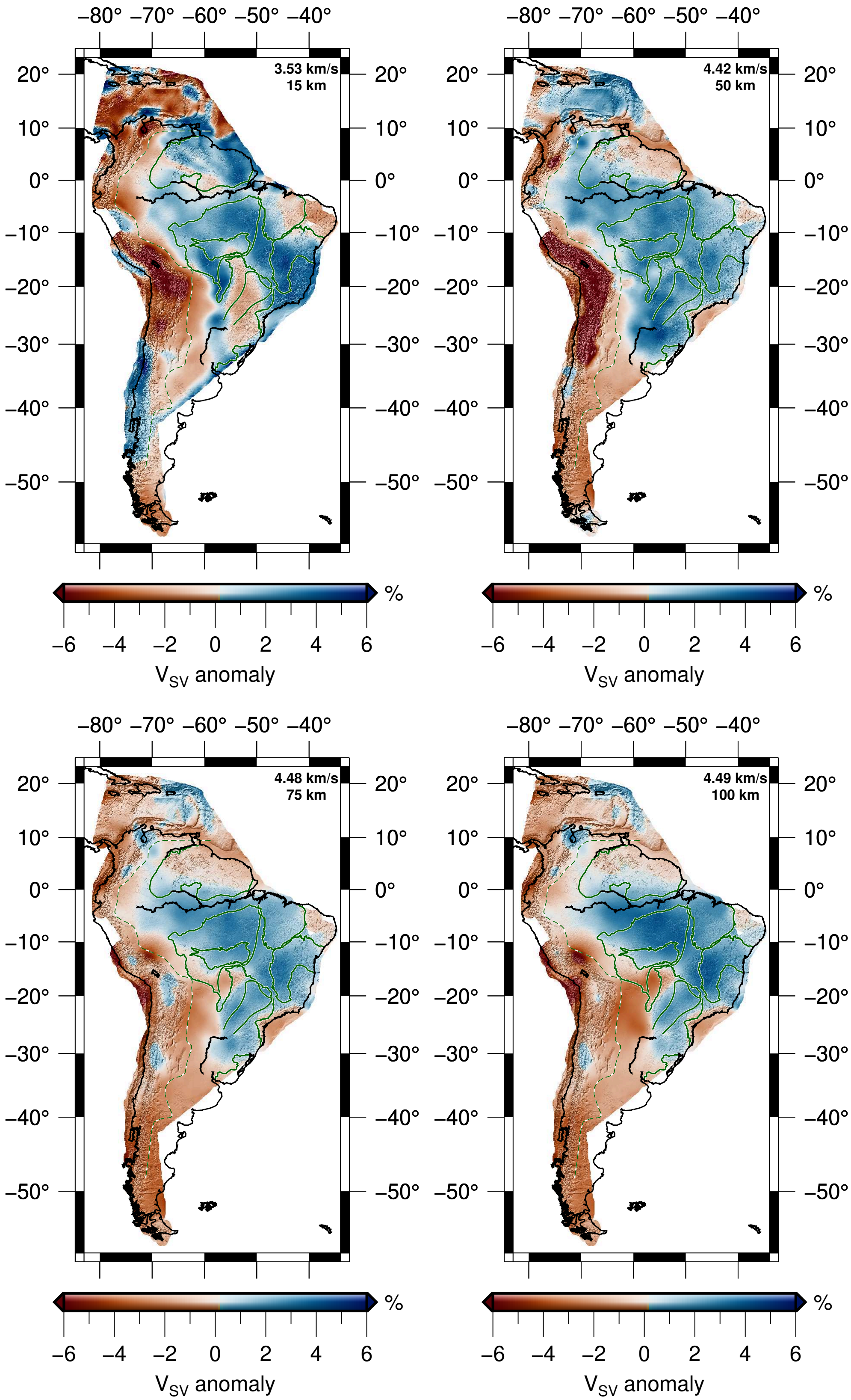
–80° –70° –60° –50° –40°
20°
10°
0°
–10°
–20°
–30°
–40°
–50°
3.53 km/s
15 km
4.42 km/s
50 km
4.48 km/s
75 km
4.49 km/s
100 km
–6 –4 –2 0 2 4 6
%
V_SV anomaly

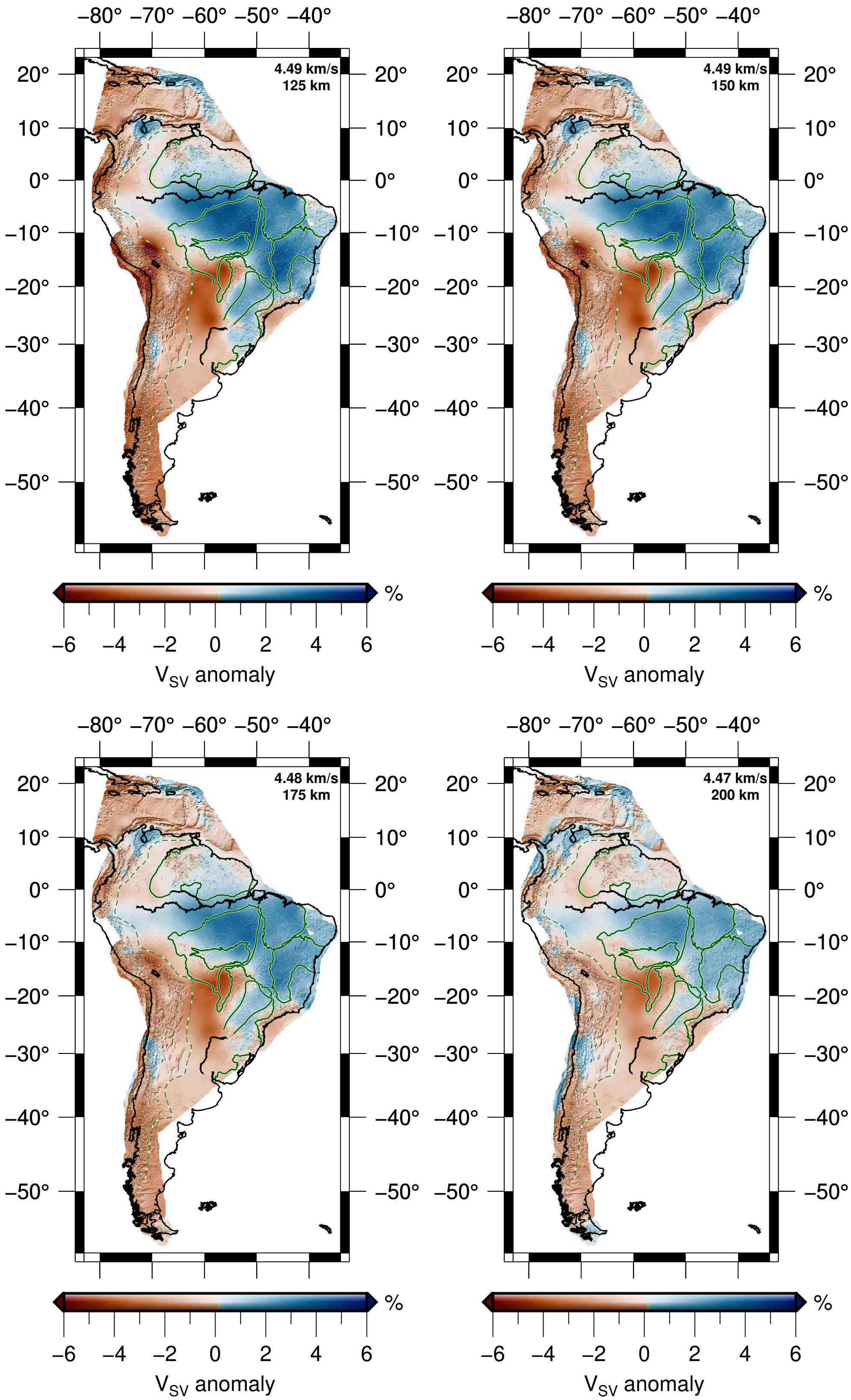
4.49 km/s
125 km
4.49 km/s
150 km
4.48 km/s
175 km
4.47 km/s
200 km
−80° −70° −60° −50° −40°
20° 10° 0° −10° −20° −30° −40° −50°
−6 −4 −2 0 2 4 6
%
V_SV anomaly

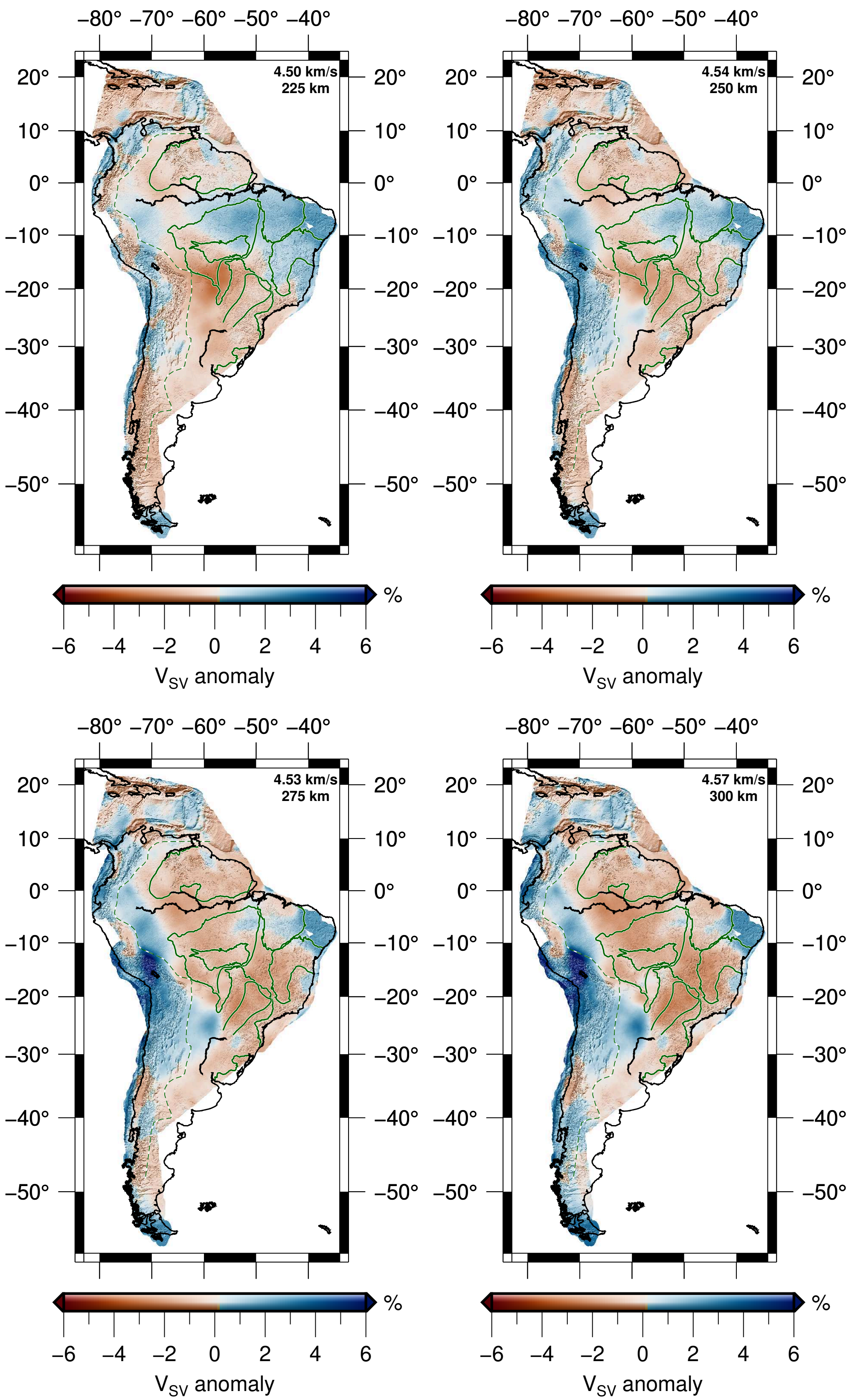

Fig. A5: 3D shear wave velocities for South America between 15 to 300 km. The V_{SV} anomalies are shown in relation to the regional average for each depth (top right velocity in each map). The green outlines are the main tectonic units of South America.

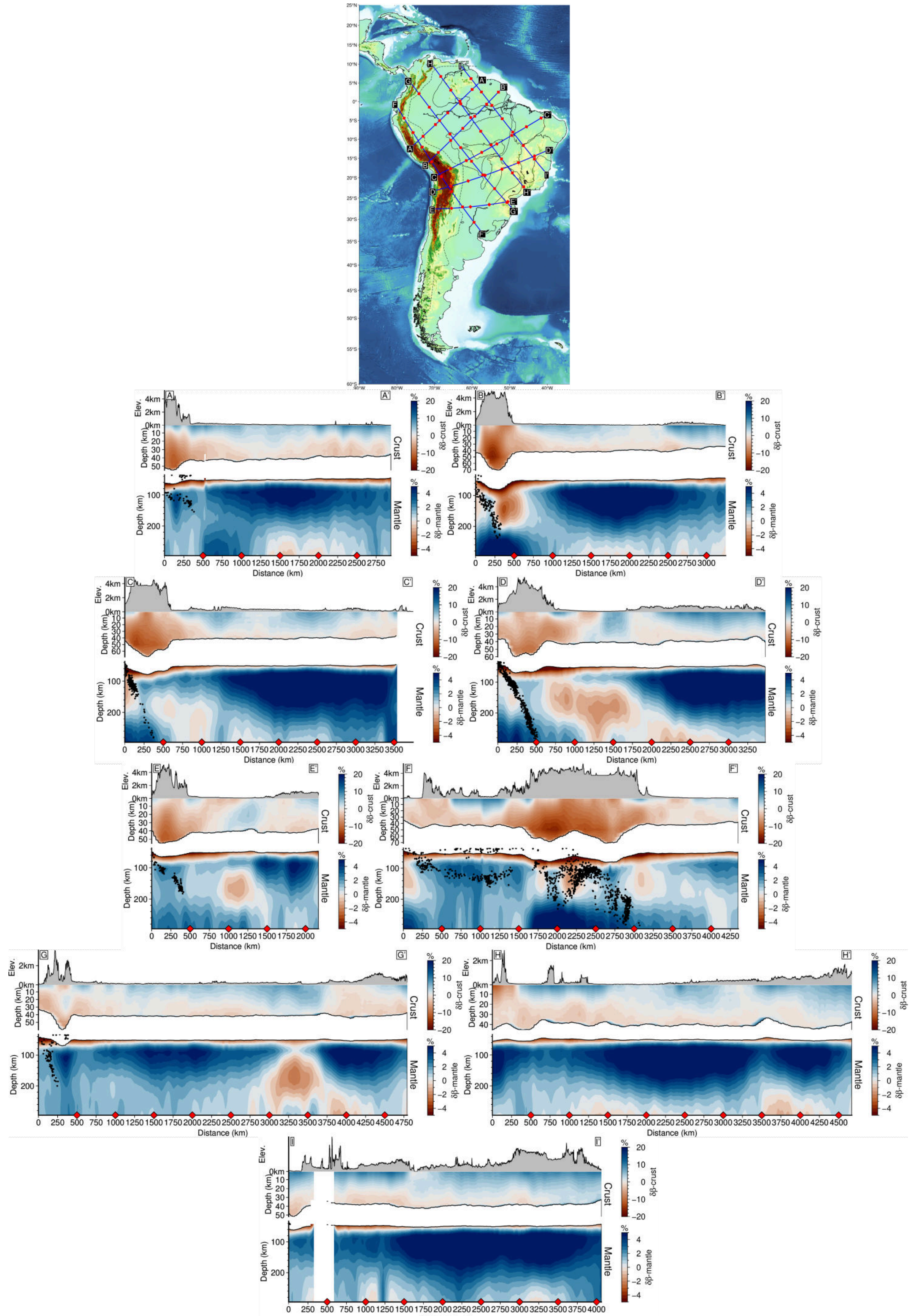

Fig. A6: All vertical cross-sections (A to I) of the shear-wave velocity model, with red diamonds plotted every 500 km along the profiles. The shear wave anomalies are plotted in relation to a 1D gradient velocity model for the crust and mantle The topography is plotted above each cross-section. The ISC-EHB seismicity is shown as red dots. Blank spots mean no data.

11 Appendix B - Paper I

"Earthquake Surface Wave Phase Velocity Tomography of the South American Lithosphere" study produced in cooperation with Prof. Dr. Thomas Meier and his group from the University of Kiel in Germany as part of the *Programa Institucional de Internacionalização* from the *Coordenação de Aperfeiçoamento de Pessoal de Nível Superior* (CAPES). The work was submitted to *Geophysical Journal International* on July 4th, 2024 and is available in this appendix.

Earthquake Surface Wave Phase Velocity Tomography of the South American Lithosphere

L. Quadros[1], A. El-Sharkawy[2,3], M. Assumpção[1], F. Eckel[2], L. Wiesenberg[2], T. Meier[2], S. Lebedev[4], M. Timkó[5], M. Bianchi[1]

[1]Institute of Astronomy, Geophysics and Atmospheric Sciences, University of São Paulo, 05508-090, São Paulo, Brazil

[2]Institute of Geoscience, Christian-Albrechts University, 24118, Kiel, Germany

[3]National Research Institute of Astronomy and Geophysics (NRIAG), 11421, Helwan, Cairo, Egypt

[4]Department of Earth Sciences, University of Cambridge, Cambridge, United Kingdom

[5]Kövesligethy Radó Seismological Observatory, Institute of Earth Physics and Space Science, Budapest, Hungary

Correspondent author: L. Quadros[1] (lucio.quadros@outlook.com)

Abstract

Rayleigh-wave phase velocities are automatically determined using earthquake records of 1,022 stations throughout South America, Antarctica and the Caribbean between 1990 and 2020 for 10,799 earthquakes resulting in 19,522 interstation measurements. Isotropic and anisotropic phase-velocity maps are presented for periods between 5 and 200 s. For depth between 15 km and 300 km, the isotropic components were used to calculate a 3-D shear-wave velocity model for the continent, based on a stochastic particle-swarm-optimization inversion technique. We also obtain a Moho map for South America that shows good agreement with the most recent crustal thickness map for South America. Azimuthal anisotropy is observed in areas of previously poor coverage by SKS studies within the South American Platform, including the Amazonian Basin, Amazonian Craton, and Pantanal Basin. For periods above 60 s, we observed a NE-SW oriented fast direction of azimuthal anisotropy in the regions of the Pantanal and Chaco-Paraná sedimentary basins. This trend coincides with a low-velocity zone (-4% V_{SV} at 100 km) observed in this and other studies interpreted as thinned lithosphere. This result suggests that mantle flow is channeled by the lithospheric topography in this area. At crustal depths, beneath the Andes, azimuthal anisotropy is oriented parallel to the strike of the orogeny, which is consistent with the observed compression of the South American Plate from the subduction of the Nazca Slab. We also observe a systematic difference between the Guyana and Brazilian Shields at lithospheric depths. Our model shows that, on average, shear-wave velocities are approximately 3% lower in the Guyana Shield than in the Brazilian Shield that may result from thermal erosion in the Central Atlantic Magmatic Province. Finally, low crustal and lithospheric thickness is observed in the Tocantins Province in Brazil in accordance with previous seismic refraction and receiver function studies that might explain the high seismicity observed in this area.

Keywords: Crustal imaging, Moho depth, Seismic anisotropy and Seismic tomography

1 Introduction

1.1 Geological Framework

The South American Lithosphere can be divided into three main units: 1) The South American Platform or SAP (Almeida et al. 2000), a mostly stable region since Phanerozoic times that was not affected by the Andean and Caribbean orogenesis; 2) The Andean Phanerozoic Orogeny; and 3) The Patagonian microcontinent. The SAP is bounded west by the Andean Phanerozoic Orogeny, south by the Patagonian block, east by the Atlantic Ocean and north by the Caribbean (Fig. 1). The SAP is divided into cratonic blocks of ages Archean and Proterozoic (blue text in Fig. 1 corresponds to Guyana Shield - GS, Central Brazil Shield - BS, Amazonian Craton - AC, São Francisco Craton - SFC, Rio Apa Craton - RC, Paranapanema Craton - PC and Rio de la Plata Craton - RPC) that are connected by Neoproterozoic mobile belts (green text in Fig. 1 corresponds to Tocantins Province - TP, Borborema Province - BP and Mantiqueira Province - MP). Several Precambrian orogenic events were responsible for the formation of the lithosphere that ranged from 2.2 Ga to 0.5 Ga (Cordani and Sato 1999) through a series of episodes of agglutinations with posterior fragmentation (Almeida et al. 2000). The SAP can be divided into an Amazonian and an Atlantic domain based on their distinct tectonic evolution (Almeida et al. 1981): 1) Amazonian domain contains, more importantly, the AC, whose origin is related to the paleocontinent Laurentia; 2) Atlantic domain whose origin is related to the western region of the Gondwana supercontinent and it contains the cratons of SFC, PC and RPC. All the mentioned cratons have outcrops on the surface (blue and red lines are cratons and sedimentary basins in Fig. 1, respectively), except the PC (blue dashed line in Fig. 1) that is supposed to be underneath the Paraná Basin (Affonso et al. 2021; Mantovani et al. 2005; Ciardelli et al. 2022; Celli et al. 2020). Those domains are roughly divided by a 2,700 km continental-scale megashear zone called Transbrasiliano Lineament (Cordani and Sato 1999; Cordani et al. 2013) or TBL (purple dashed line in Fig. 1). A series of Phanerozoic intracratonic basins (red text in Fig. 1 corresponds to Amazonian Basin - AB, Parnaíba Basin - PaB, Parecis Basin - PrB, Pantanal Basin - PtB, Paraná Basin - PB and Chaco-Paraná Basin - CPB) covers most of the cratonic units of the platform.

A Mesozoic reactivation associated with the fragmentation of the Pangea Supercontinent (Deckart et al. 2005) and opening of the Atlantic Ocean (O'Connor and Duncan 1990) caused magmatism to occur throughout the SAP: 1) Central Atlantic Magmatic Province (CAMP) with its emplacement happening around 200 Ma (Deckart et al. 2005; Marzoli et al. 2018) with extensive basalt flooding in AB and NW-SE and NE-SW orientation dykes in the eastern and northern areas of the GS (Deckart et al. 2005; Knight et al. 2004); 2) Paraná-Etendeka Large Igneous Province, with a major magmatism peak between 137-120 Ma, produced extensive basalt flooding affecting mostly the PB (Turner et al. 1994; Renne et al. 1996; Thiede and Vasconcelos 2010).

1.2 Previous studies

For the SAP, regional P and S tomographies and surface-wave studies allowed for a delineation of the mentioned tectonic units laterally and in depth (e.g. Affonso et al. 2021; Rocha et al. 2019; Feng et al. 2004; Rosa et al. 2016; Lee et al. 2001; Costa et al. 2020; Heintz et al. 2005; Rocha et al. 2011; Simões Neto et al. 2018; Feng et al. 2007). The P-wave tomographies identify strong high-velocity (around 1% for P-wave) anomalies for the PC from 100- to 300 km depth (Affonso et al. 2021; Rocha et al. 2011) and consistent with the block delineation by gravimetric signature from Mantovani et al. (2005). The Partitioned and Full Waveform Inversions by Celli et al. (2020) and Ciardelli et al. (2022) observe high velocities for the PC. For the AC, in general, surface-wave and waveform inversion studies identify high upper-mantle velocities up to 200 km depth, especially in the eastern older provinces of the craton (e.g. Feng et al. 2004; Feng et al. 2007; Heit et al. 2007; Ciardelli et al. 2022; Celli et al. 2020; Nascimento et al. 2022). High-velocity anomalies are also observed for the SFC (e.g. Feng et al. 2004; Feng et al. 2007; Ciardelli et al. 2022; Celli et al. 2020; Nascimento et al. 2022). Global models (e.g. Priestley et al. 2018; Schaeffer and Lebedev 2013) also identify high-velocity anomalies. However, they tend not to show the cratons separately. At crustal depths, we observe low-velocity anomalies in the areas of sedimentary basins from both surface-wave studies (e.g. Feng et al. 2004; Nascimento et al. 2022) and ambient noise (Shirzad et al. 2020), with exception of the PtB, that has a very thin (500 m) sedimentary layer (Catto 1975; Weyler 1962).

The anisotropy of South America is mostly regionally studied using Shear Wave Splitting, SWS (e.g. Melo et al. 2018; Assumpcao et al. 2011; Heintz et al. 2003; Assumpção et al. 2006; Russo and Silver 1994; James and Assumpção 1996; Polet et al. 2000; Krüger et al. 2002; Anderson et al. 2004; Piñero-Feliciangeli and Kendall 2008; Growdon et al. 2009; Masy et al. 2009), and geodynamic models (Hu et al. 2017). For the asthenospheric upper mantle, the anisotropy is thought to be primarily attributed to subduction-induced mantle flow (Hu et al. 2017) or to have some additional contribution from it being deflected by the cratonic roots (Melo et al. 2018; Assumpcao et al. 2011; Assumpção et al. 2006). The AC and PC were observed to cause this deflection in SWS studies (Melo et al. 2018; Assumpcao et al. 2011; Assumpção et al. 2006). In the SAP, those studies are usually limited to the southeastern region of the continent and along the Andes.

2 Data and Method

2.1 Overview

The study of the South American Lithosphere seismic structure as a whole has always been a challenge given the sparse station coverage, especially in the SAP. Methods such as SWS are especially affected by the lack of station coverage. However, two-station methods (e.g. Meier et al. 2004; Kästle et al. 2016; Soomro et al. 2016) can be used to provide accurate surface-wave dispersion data that can be used to derive isotropic and anisotropic anomalies along the whole ray path between a pair of stations. Two-station measurements have an advantage over single-station measurements by not being affected by source mechanism and localization errors (e.g. Muyzert and Snieder 1996; Levshin et al. 1999). Beyond that, the bandwidth for Rayleigh-wave two-station measurements is generally broader than single-station, especially for high frequencies (Lebedev et al. 2006). For the previously mentioned earthquake-based surface-wave studies in the SAP (Feng et al. 2004; Rosa et al. 2016; Lee et al. 2001; Heintz et al. 2005; Feng et al. 2007; Nascimento et al. 2022), all of them use single-station measurements. We used the two-station method to compute a simultaneous inversion for isotropic and anisotropic anomalies using Rayleigh-wave phase velocities in South America.

In the SAP, shear-wave velocity models have commonly been linearly inverted using deterministic methods (e.g. Julià et al. 2000) that jointly invert both surface-wave and receiver function data. However, this type of inversion has complex nonlinearity and its linear approximation requires an initial model close enough to the true earth structure (Ammon et al. 1990; Julià et al. 2000). Stochastic methods allow for a random iterative search over an acceptable model space to find the best solutions for this inverse problem. We used the isotropic component from the inverted phase-velocity maps to compute a 3-D shear-wave velocity model for the continent using a new stochastic inversion approach by El-Sharkawy et al. (2020).

2.2 Data

We applied the two-station method (e.g. Meier et al. 2004; Kästle et al. 2016; Soomro et al. 2016) to measure Rayleigh-wave phase velocities using earthquakes closely aligned with pair of stations. We downloaded broadband earthquake records from 1,022 stations in South America, Antarctica and the Caribbean, as seen in Fig. 2, between 1990 and 2020, from the IRIS data center and the Brazilian Seismographic Network (Bianchi et al.

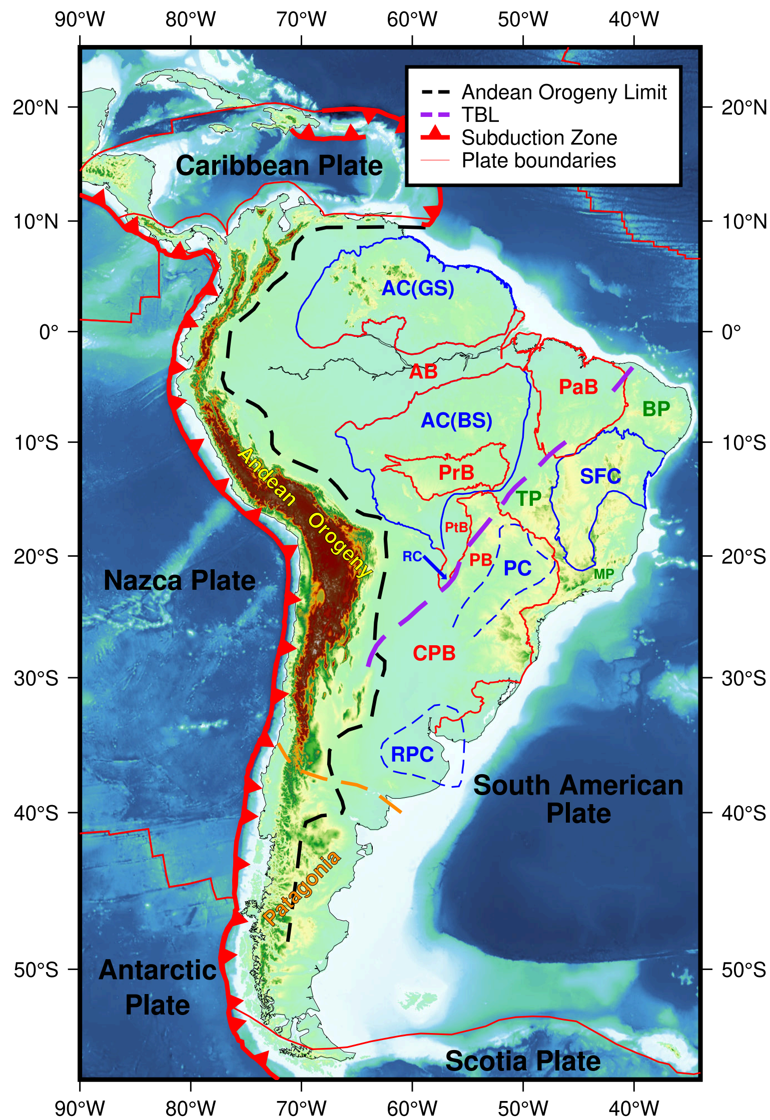

Fig. 1: Major tectonic units for South America. Plate boundaries are shown as a red lines while dented lines are for subductions (Hasterok et al. 2022). Blue outline are craton limits (dashed for cratonic blocks buried beneath sedimentary basins) and red are limits of sedimentary basins (Almeida et al. 1981; Cingolani and Salda 2000). Labels are blue for cratons, red for Phanerozoic sedimentary basins and green for Neoproterozoic orogenic belts. AC = Amazon Craton, composed of the Guyana Shield (GS) and Central Brazil Shield (BS), SFC = São Francisco Craton, RC = Rio Apa Craton, PC = Paranapanema Cratonic block inferred from gravity data (Mantovani et al. 2005) and the RPC = Rio de La Plata Craton. Fold belt provinces: Tocantins (TP), Borborema (BP) and Mantiqueira (MP). Phanerozoic sedimentary basins: Amazonian (AB), Parnaíba (PaB), Parecis (PrB), Pantanal (PtB), Paraná (PB) and Chaco-Paraná (CPB). The dashed purple line denotes the transcontinental Transbrasiliano Lineament, or TBL (Cordani et al. 2016). The black dashed line is the limit between the Andean orogenic belt (Cordani et al. 2016) and the stable platform (Almeida et al. 2000). Orange dashed line is the limit of the Patagonia Paleozoic terrain (Ramos 2008).z

2018). A total of 10,799 earthquakes were selected based on the following criteria: (1) Events aligned within 10° of the great circle path between a pair of stations; (2) A linearly increasing minimum magnitude between 4 and 6 Mw as a function of the epicentral distance; (3) Epicentral distances between 2.5° and 130°.

Fig. 2 shows our station distribution (a) and the 76,038 ray paths coverage (b). The colors indicate the number of events used for each station and interstation path for Fig. 2a and b, respectively. The stations in the Caribbean, Andes and some of the permanent Brazilian seismographic stations provide most of our data.

2.3 Method

2.3.1 Phase-velocity measurement

We followed the automatic implementation of Soomro et al. 2016 to calculate the Rayleigh-wave phase velocities. The phase velocity can be derived from the phase term of the cross-correlation of the earthquake records on each station (Meier et al. 2004). The cross-correlation has the advantage of being less affected by uncorrelated noise and the contribution of the fundamental mode is enhanced by the product of the amplitude spectra, especially towards higher frequencies (Soomro et al. 2016). Fig. S1 gives a general idea of this procedure for the 7.9 Mw Cantwell Alaska Earthquake.

2.3.2 Selection of phase-velocity curves

To select realistic 1-D phase-velocity curves, we follow the automatic selection procedure from Soomro et al. 2016. The first criterion is the background model, where we only allowed a maximum difference of 15% between the calculated and a reference dispersion curve. The reference curve was calculated for each station pair using path averages in a 3-D velocity model constructed from CRUST1.0 (Laske et al. 2013) and the Preliminary reference Earth model, PREM (Dziewonski and Anderson 1981). The second criterion is smoothness as a function of frequency, calculated by taking the first derivative of the dispersion curve. Finally, the length criterion, where dispersion curves with period-length smaller than a frequency-dependent threshold are rejected.

Because the phase-velocity curves calculated for each event can have some variability, especially for events propagating in opposite directions (Soomro et al. 2016). It is necessary to apply further quality control before taking the final average. Following closely Soomro et al. 2016 implementation, for each frequency: (1) 15% of the outermost values were rejected; (2) minimum required measurements of 5; (3) the average and the standard deviation are calculated for each propagation direction ($std1$, $std2$) to define the threshold as $th_{std} = 5 \times max(std1, std2)$. The absolute difference of the mean curves in both directions must be smaller than th_{std}; (4)

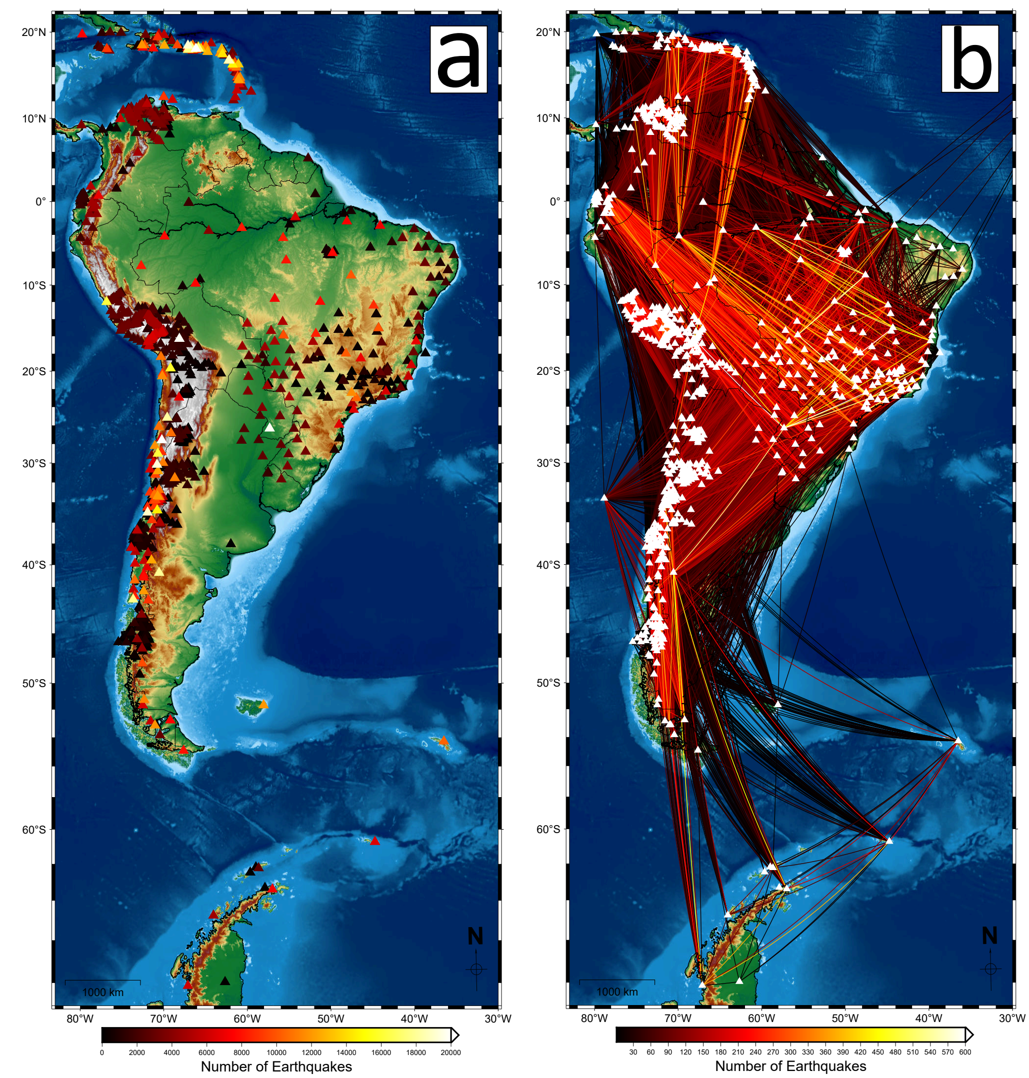

Fig. 2: Color-coded number of earthquake records, between 1990 and 2020, used for each station (a) and for each station-pair along the great-circle path (b). A total of 1,022 stations recorded 10,799 earthquakes distributed over 76,038 interstation paths to calculate Rayleigh-wave phase-velocity maps for South America. The paths going northeastward in (b) are from stations on the Madeira Island, Portugal on the Atlantic Ocean.

the standard deviation of all measurements should be lower than 3%; (5) for the remaining segments, the length criterion is applied again.

Following this process, we obtained 19,522 Rayleigh-wave dispersion measurements between 4 and 315 s (around 26% of the initial dataset). Fig. 3 shows a hitcount plot for all the average dispersion curves. Most of our data is below 200 s, which can roughly indicate we can investigate, at most, 300 km depth. We also observe two branches for periods higher than 15 s where the bottom one is related to the high crustal thickness below the Andes and the top one is related to the cratonic areas inside in the SAP (Fig. 1). The measurements' average standard deviation is approximately 1.5% for all periods (Fig. S2). Fig. 4 shows five examples of average dispersion curves throughout mostly the cratonic area of the SAP. Fig. 4a shows the color-coded location of the interstation paths and Fig. 4b shows all the dispersion curves. Fig. 4b also shows the Civiero et al. (2024) global average cratonic dispersion curve in gray and a shaded area that corresponds to this reference curve ± 0.1 km/s. The shaded area correspond, roughly, to the distribution of dispersion curves around the mean from Civiero et al. (2024). Our dispersions show good agreement with the reference model, starting to deviating only below 15 s. The dispersion that goes through a non-cratonic area (green curve) shows considerably lower phase velocities between 40- and 110 s. In the same period range, we can also observe a systematic difference between the red and brown curves going through the east and west of the AC, respectively. The eastern portion of the AC is the oldest province of the craton (Santos et al. 2000) and several studies identify a high-velocity anomaly in this region (e.g. Feng et al. 2004; Feng et al. 2007; Heit et al. 2007; Ciardelli et al. 2022; Celli et al. 2020; Nascimento et al. 2022).

3 Isotropic and anisotropic phase-velocity maps

We followed Deschamps et al. (2008) by conducting a simultaneous isotropic and anisotropic phase-velocity inversion for Rayleigh waves for periods between 5 and 200 s. The model is parameterized in a triangular grid with a node spacing of 30 km.

3.1 Checkerboard test

Checkerboard tests were made to verify the resolution of our phase-velocity model using different cell sizes for 30 and 100 s. We used checkers of sizes of 1.5°, 3° and 6° spaced by 2°, 2° and 4°, respectively. The test results are shown in Fig. 5.

For 1.5° and 30 s, the test shows well resolved anomalies in the central part of South America and the central Andes. We also can resolve some anomalies in the Southern Andes (along ~70°W). For 100 s, the coverage

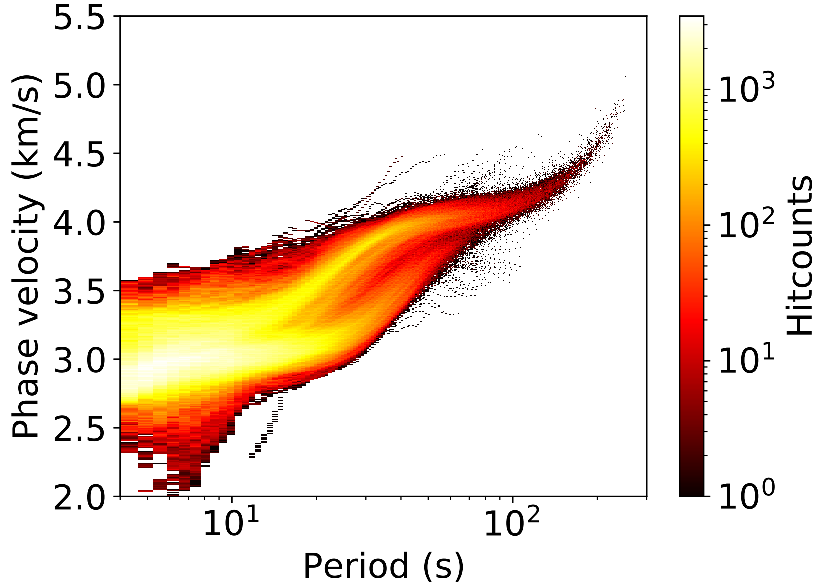

Fig. 3: Hitcount for the final selected dispersion curves. The bottom branch after 15 s shows mainly the lower velocities from the Andean thick crust while the top branch shows higher velocities related to velocities in the upper mantle below the stable continental region.

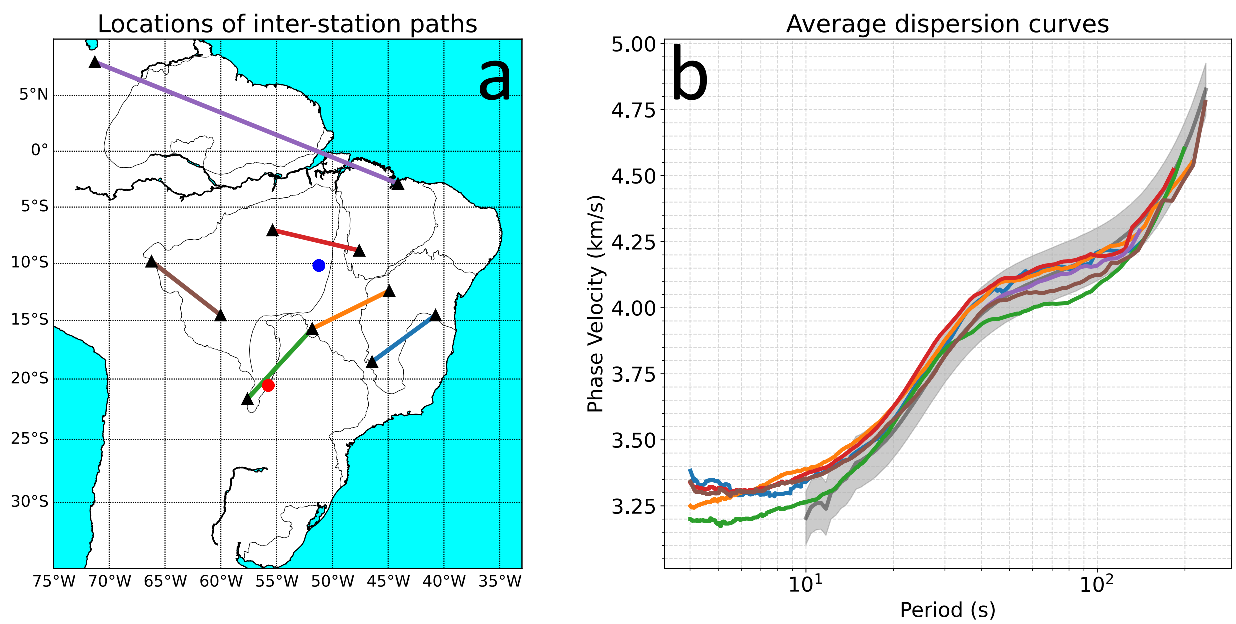

Fig. 4: Example of six average Rayeligh-wave phase-velocity dispersion curves for different tectonic areas. (a) location of each interstation path. The blue and red dots are the locations of shear-wave velocity inversion profiles in Fig. 8 for the Amazonian Craton and Pantanal Basin, respectively. (b) plot of all six dispersion curves. In (b), the global average dispersion for cratons (Civiero et al. 2024) is shown as a dark gray line and the shaded area corresponds to the reference curve $\pm 0.1\,km/s$.

for this checker size is slightly worse, where the main well-resolved area is the cratonic area (mainly Brazil) to the east.

For 3° and 30 s, the coverage is largely similar to 1.5°, but we can resolve a larger region overall in the central part of South America. Also, we can further include a portion of the northern Andes (∼5°N ∼73°S) and east of the Caribbean plate. For 100 s, the test shows similar results to the 1.5° checkerboard test.

For 6°, both periods show we can recover anomalies throughout the model for large-scale features, however, we observe an slightly attenuation of the recovered amplitudes for checkers north of 0° latitude and south of 30°S.

From those tests, our models have good resolution for most of central South America (mainly Brazil), but covering a larger area in the lower periods (e.g. 30 s) with relation to the longer periods (e.g. 100 s). Outside this high-resolution area, we can recover the average tendencies of the medium for large-scale features.

3.2 Rotation test

We applied a two-step procedure to verify the anisotropy component's reliability. First, anisotropies with small amplitudes mostly indicate an isotropic medium. Therefore, they are of no use for the interpretation. We defined a low amplitude threshold, th_A, using the standard deviation of all anisotropy amplitudes, A_{std}, and its mean, A_{mean}, for each period. Then we defined a frequency-independent threshold as $th_A = mean(A_{mean} - A_{std})$ or 7.41 m/s (Fig. S3). Second, for the remaining curves, we applied the 90° rotation test (e.g. Zhang et al. 2009; Endrun et al. 2011; Schaeffer et al. 2016; Wiesenberg et al. 2022). In this test, we rotate the original 2ψ terms 90° while the 4ψ terms are set to zero. Then, we remake the inversion with an initial model that combines the rotated anisotropy and the original isotropic component. The directions of the rotated anisotropy and the one retrieved from the test must be within 20° of each other to be considered a robust result. Fig. 6a shows a cropped region of our model in northern Brazil at 30 s. Azimuthal anisotropy fast direction is plotted over the isotropic model as red bars. Those original amplitudes are rotated 90° with a fixed amplitude (white bars in Fig. 6b) and the recovered anisotropies after remaking the inversion are shown as black bars in Fig. 6b. Fig. 6c shows the cleaned results, where the nodes with amplitudes smaller than th_A are shown as red circles and the nodes where the direction differences were larger than 20° were removed. Fig. S4 shows further examples of the uncleaned phase-velocity maps for 15-, 30-, 60- and 100 s. Fig. S5 shows rotation test examples for the whole model for the same period.

The final, cleaned, results can be seen in Fig. 7 for 15-, 30-, 60- and 100 s. The main area where nodes were removed by amplitude and rotation test was the Guyana Shield. Beyond that, some low-amplitude nodes inside Brazil were also removed. The nodes with NE-SW orientations below the Pantanal Basin and Andean nodes were kept after this test.

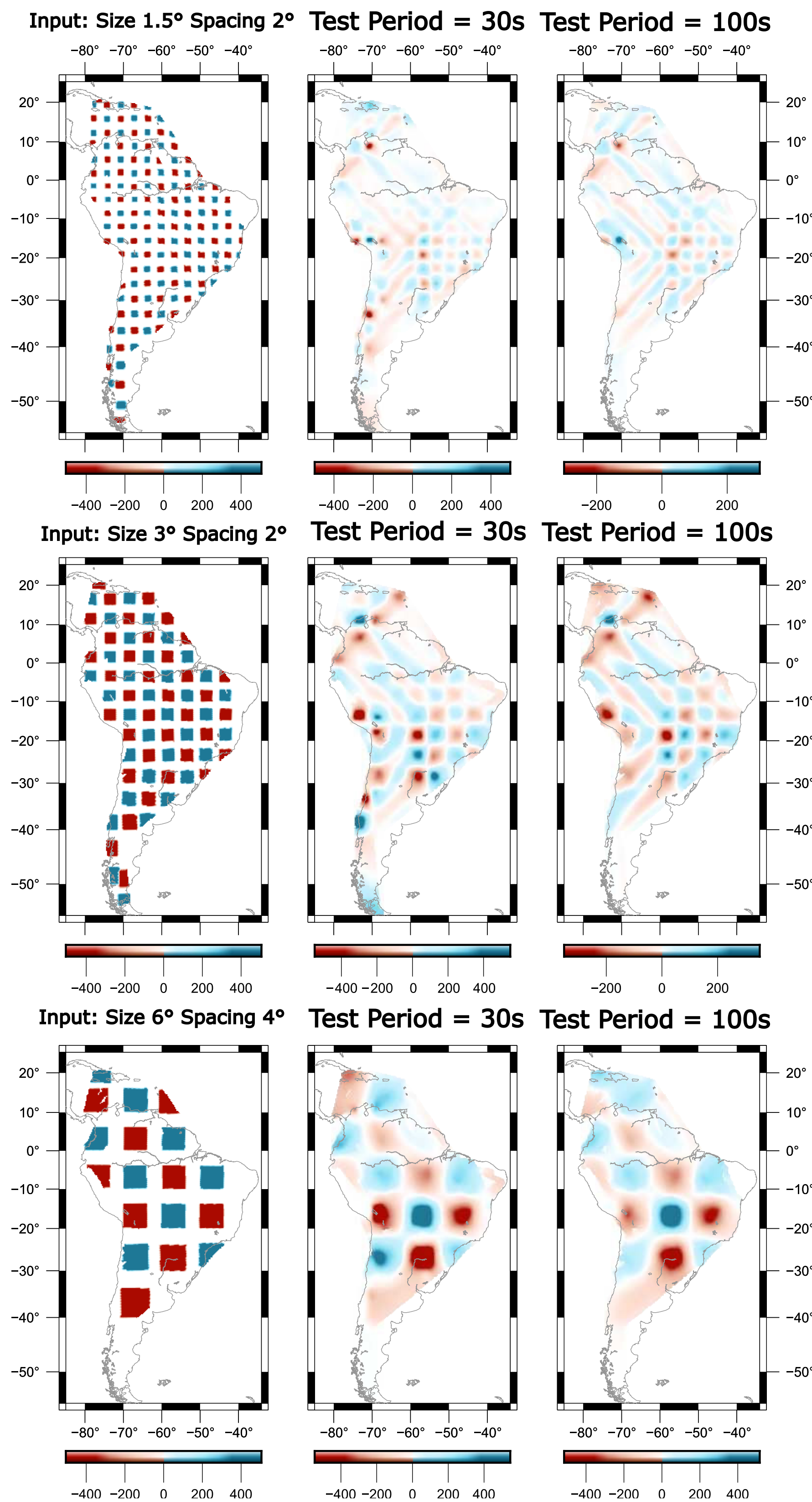

Fig. 5: Checkerboard tests for the isotropic component of the Rayleigh-wave phase-velocity map at 30 and 100 s. We tested checkers with sizes of 1.5°, 3° and 6° spaced by 2°, 2° and 4°, respectively. Anomaly scale is in m/s.

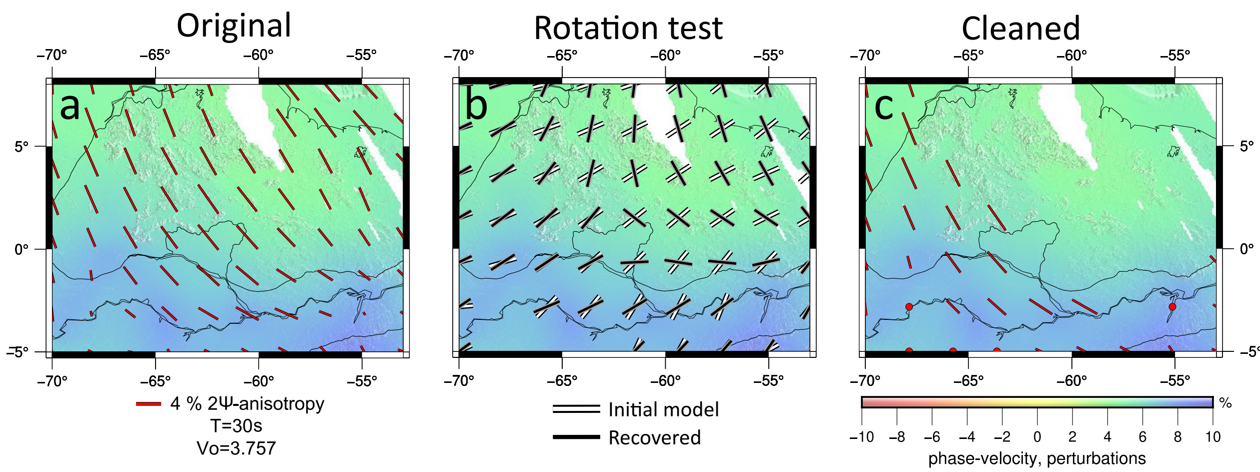

Fig. 6: Rotation test example for the azimuthal anisotropy for the Guyana Shield Craton for 30 s. (a) shows the originally calculated anisotropies as red bars. (b) shows the rotation test in two steps: (1) anisotropies with amplitudes smaller than an empirically defined threshold of 7.41 m/s are removed and (2) the remaining amplitudes are tested using the 90° rotation test (e.g. Zhang et al. 2009; Endrun et al. 2011; Schaeffer et al. 2016; Wiesenberg et al. 2022). The white bars are the original anisotropies rotated 90°. The black bars are the anisotropies recovered after the inversion. Measurements were accepted if the initial and recovered anisotropies are within 20° of each other. (c) shows the final cleaned results. The original anisotropies that passed both steps are shown as red bars and anisotropies that were smaller than the amplitude threshold are plotted as red dots.

4 Depth inversion (V_{SV})

Phase-velocity maps between 5 and 200 s every 5 s were used to extract local dispersion curves at each node following the implementation by Timkó et al. (2022). Where the roughness of the local dispersion curve (eq. 6 of Timkó et al. 2022) is evaluated and the rough samples are removed if they are outside a minimum (0.005) or maximum (0.01) thresholds. The roughness of the local dispersion curves tends to increase mainly for higher frequencies. Therefore, this evaluation was only applied for periods below 50 s. Timkó et al. (2022) method can also estimate a frequency-dependent standard deviation given *a priori* standard deviation values. We used an extensive compilation of earthquake-based dispersion curves from El-Sharkawy et al. 2020 dataset. In order to interpret those phase velocities in terms of shear-wave velocities as a function of depth, we used the implementation of El-Sharkawy et al. 2020 which is based on the particle-swarm-optimization (PSO) technique by Eberhart and Kennedy (1995) and Wilken and Rabbel (2012). This technique creates random background model perturbations for specified depth-dependent velocity ranges. We can calculate synthetic dispersion curves from those random models and compare the resulting misfit between the measured and synthetic dispersion curves. The initial background models were created for each node using CRUST1.0 (Laske et al. 2013) and an isotropic average of PREM (Dziewonski and Anderson 1981) for the upper mantle. A depth-dependent parameterization and regularization can be applied to velocity perturbations on each layer and to discontinuities (such as Moho depth).

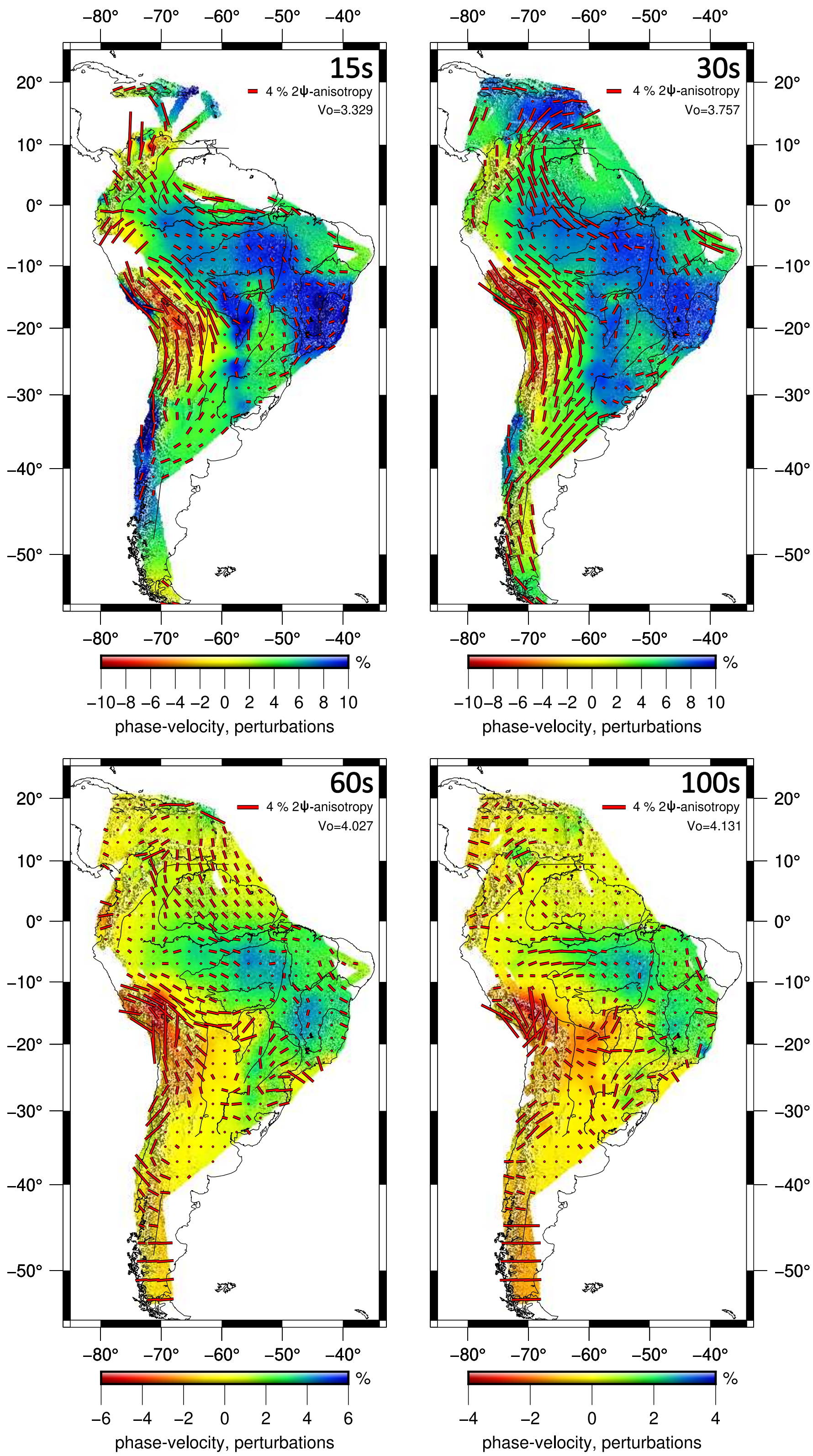

Fig. 7: Final Rayleigh-wave phase-velocity maps for periods 15, 30, 60 and 100s and fast azimuthal directions after removal of anisotropy nodes that failed the rotation tests. Red dots indicate nodes with anisotropy amplitudes below the minimum threshold (<7.41 m/s). The isotropic component remained unchanged.

The model global convergence is sped up by resetting the search after a certain number of forward calculations.

We parameterized our models using eight layers composed by 87 nodes in total with quadratic perturbations on the crust and cubic in the mantle from the Moho depth down to 410 km depth. Perturbations down to 660 km depth are linear. Furthermore, the Moho depth and the depth of nodes in the crust and upper mantle are inversion parameters to ensure a high flexibility of the parametrization. The upper crust nodes had a maximum perturbation allowed of 1 km/s, while all the others were 0.5 km/s. The depth variable nodes for the lower crust, Moho, and Lithosphere-Asthenosphere Boundary (LAB) had a variability of depth of 5-, 10-, 20 km, respectively. The final models were calculated using around 10 000 forward models. Two final models were calculated: (1) the global model with the lowest misfit; and (2) the centroid model. We observed that the best-fit model tends to be similar to the centroid model in most cases, but it can, sometimes, produce final models that do not correspond to the expected geological characteristics of an area because it represents a local minimum instead of main features of models around the minimum. This issue is a consequence of the non-uniqueness of the inversion problem. We found that the centroid model correlates more closely to the known geology, so we used it instead.

We show an isotropic Rayleigh-wave depth inversion for a node in the AC and the PtB (more details can be seen in Fig. S6C and S7C). Those models' locations are given in Fig. 8. The observed and best model dispersion curves can be seen in Fig. 8(a,d) as black and red lines, respectively. The dashed line in Fig. 8(a,d) is the observed curve standard deviation. Fig. 8(b,e) show the best (black line) and centroid (red line) profiles. The red dashed line in 8(b,e) represents the profiles within 0.5 over the global minimum. Those profiles were used to calculate the centroid model, following El-Sharkawy et al. 2020. Fig. 8(c,f) show the sampled model space. The profiles are sorted from worst (gray) to best (blue) global misfits. The centroid model is shown as a coarse dashed line.

For the Amazon Craton node (Fig. 8 blue outline). According to the centroid model (red curve Fig. 8B), we observe a pronounced increase in the shear wave velocities around 100 to 200 km, indicating a high lithospheric thickness. Our results for the centroid model agree with the expected thicker lithosphere from Ciardelli et al. (2022) and Priestley et al. (2018) of around 180 km from both studies. Based on the previous crustal thickness map by Rivadeneyra-Vera et al. (2019), we expected a ~40 km Moho depth for this area that agrees with the 40 km moho found.

For the Pantanal Basin node (Fig. 8 red outline). The centroid model (red curve Fig. 8B) has a pronounced decrease of shear wave velocities from 100 to 200 km, indicating a shallow lithosphere. This result agrees with the results found by Ciardelli et al. (2022) and Priestley et al. (2018). The centroid model also shows a thinner crust (~37 km) corresponding with the thin crustal thickness found in previous works (Rivadeneyra-Vera et al. 2019; Cedraz et al. 2020).

We made a V_{SV} velocity anomaly map for the whole available region using the centroid models for all

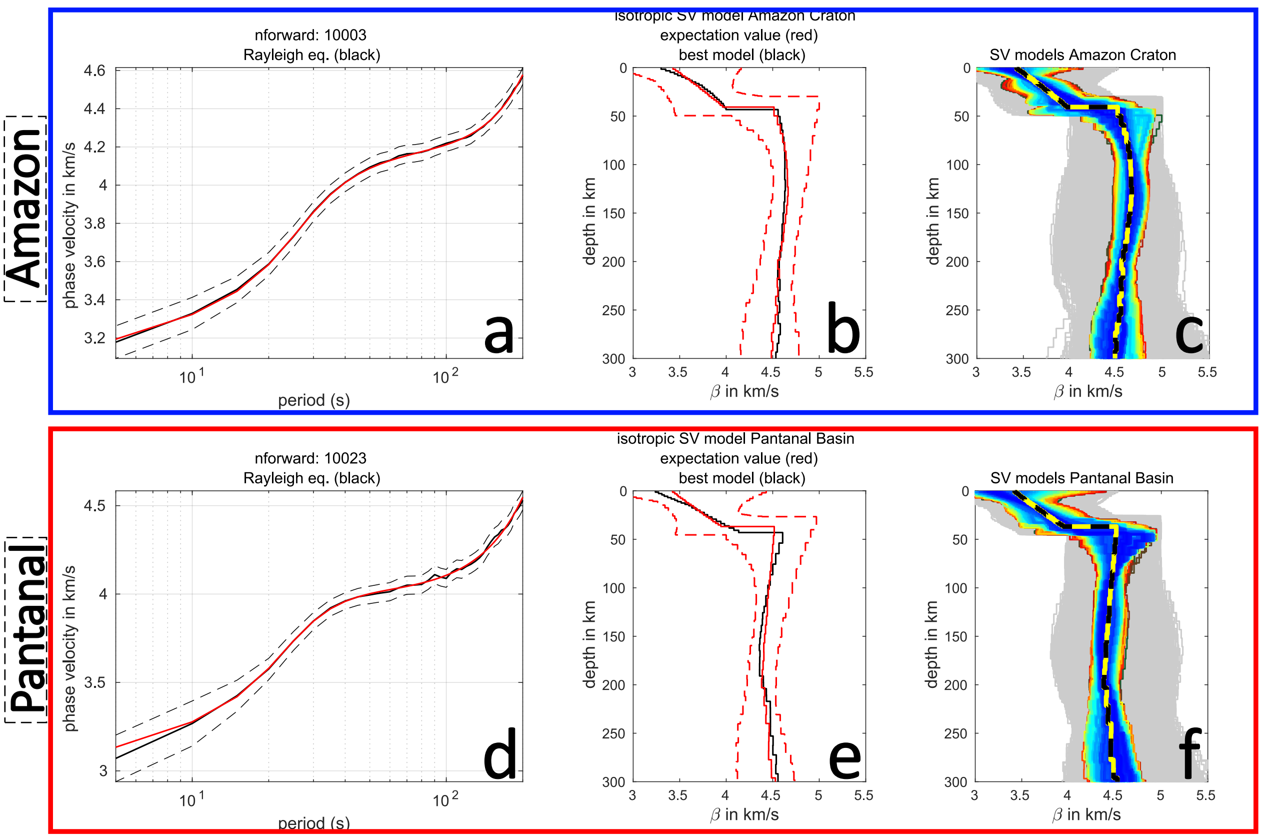

Fig. 8: V_{SV} inversion example for nodes inside the Amazon Craton (blue outline) and Pantanal Basin (red outline) node locations shown in Fig 4. (a,d) Observed local dispersion curve (black line) and its standard deviation (dashed). The red line is the best-inverted dispersion curve. (b,e) 1-D shear-wave velocity profile. Black and red lines are the best-fitting and centroid models, respectively. Red dashed lines show the range of models used to calculate the centroid. (c,f) Gray shaded areas show the sampled model space, the accepted range of models are plotted in blue and are sorted according to their misfit values. The coarse dashed line is the centroid model.

nodes. We show results for depth slices at 15-, 60-, 100- and 300 km (Fig. 9). The anomalies are plotted in relation to average velocities for each depth, reference values are shown in the top right of each figure. We present a Moho thickness map in Fig. 10. We also did nine vertical cross-sections of the model across South America (Fig. S9) with the more important for discussion in Fig. 11. To improve the visualization of the crustal structure, we separated the crustal and mantle profiles along the inverted Moho depths and used different vertical scales for both of them. To enhance the visualization of the lateral variations, we plotted the V_{SV} velocities relative to an empirically defined depth-dependent linear-gradient (Fig. 11) with different values for the crust and mantle, following Timkó et al. (2022). To identify the top of the Nazca slab, we plotted the ISC-EHB (ISC 2023; Engdahl et al. 2020; Weston et al. 2018; Engdahl et al. 1998) seismicity on the profile. The ISC-EHB is a dataset of teleseismically well-constrained events and is well-suited to visualize subduction zones.

5 Discussion

5.1 Phase-velocity maps

The isotropic phase velocity maps at periods of 15 and 30 s indicate around 8% high-velocity perturbations in the regions of: (1) cratonic blocks of the SAP (BS, SFC and RC); and (2) under the Pantanal basin, possibly related to a high-velocity lower crust. We also observed between -8 to -4% low-velocity perturbations in the Andean Mountain range root below the Bolivian Altiplano (Central Andes). The PB, CPB and PrB intracratonic basins also have lower velocities in relation to the neighboring cratonic areas. Those maps also show, in the Central Andes, anisotropy fast directions parallel to the continent coast consistent with the known compression of the South American Plate from the subduction of the Nazca slab (e.g. Assumpção et al. 2016).

The 60- and 100 s maps are mostly sensitive to the lithosphere. The high velocities ($\sim 3\%$) in the SAP's eastern portion correlate well with the deep roots of the oldest region of the AC and the SFC. Lower velocities ($\sim -2\%$) can be seen below the Pantanal basin area and are well correlated with the shallower depths of the LAB from continental scale tomography (Ciardelli et al. 2022) and global model (Priestley et al. 2018). Overall, we do not observe the anisotropy direction changes around the cratonic roots of the PC and AC (Melo et al. 2018; Assumpcao et al. 2011; Assumpção et al. 2006). However, we observe roughly NE-SW fast direction below the PtB that coincide with the area of low-velocity and thin LAB.

For 30-, 60- and 100 s, we observe that the GS has lower velocities than the BS. This result can be seen similarly in the surface-wave group velocity tomographies of Rosa et al. (2016) and Nascimento et al. (2022).

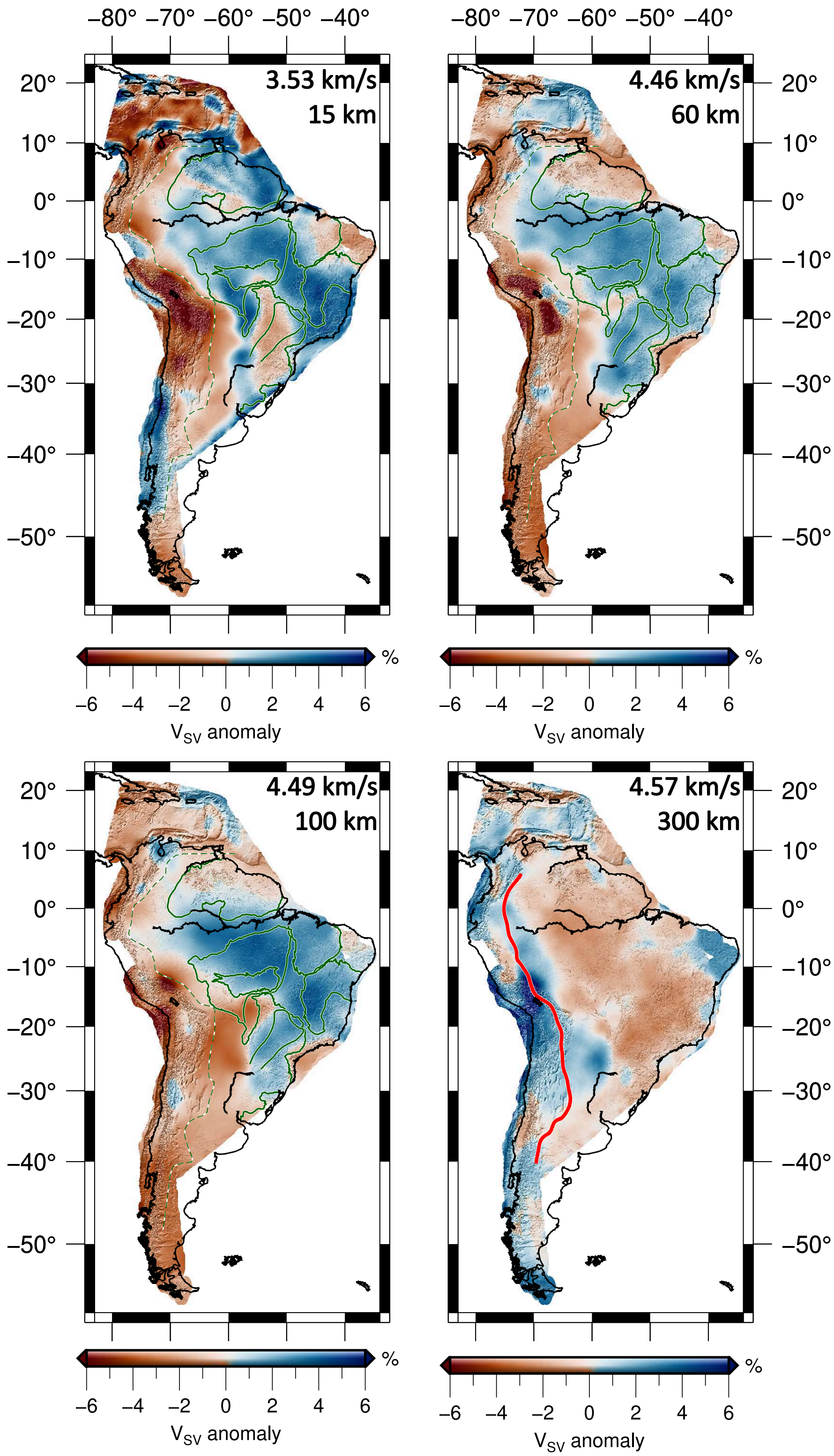

Fig. 9: 3D shear wave velocities for South America at 15, 60, 100 and 300 km. V_{SV} anomalies are shown in relation to the regional average for each depth (top right velocity in each map). For 15-, 60 and 100 km the green outlines are the main tectonic units of South America shown in Fig. 1. For 300 km, the red outline is the Nazca Plate Slab2 model for the same depth (Hayes et al. 2018).

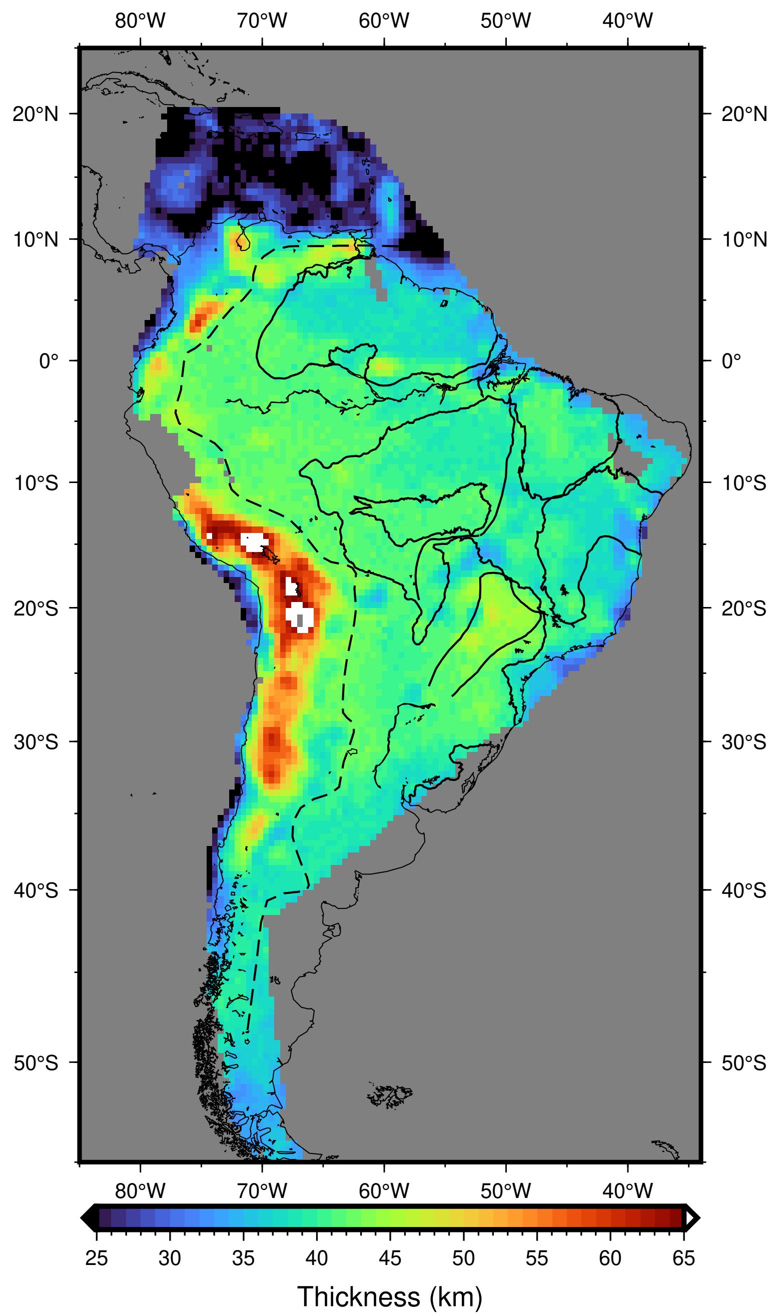

Fig. 10: Crustal thickness map for South America derived from the V_{SV} inversion. Black lines are the main tectonic units of South America, as in Fig. 1.

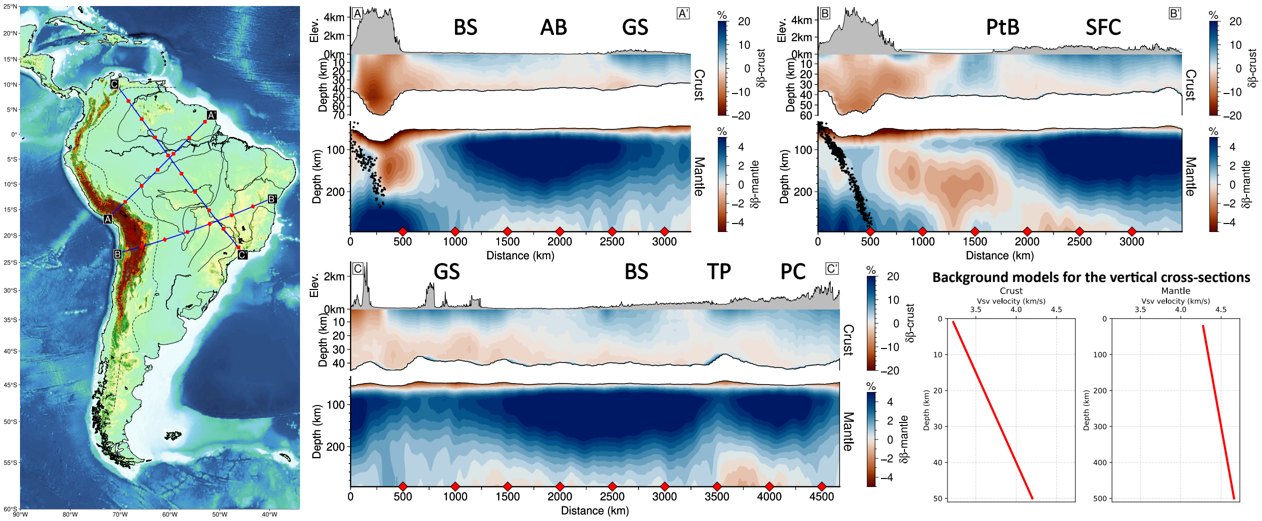

Fig. 11: Vertical cross-sections (A, B and C) of the shear wave velocity model, with red diamonds plotted every 500 km along the profiles. The shear wave anomalies are plotted in relation to a 1D gradient velocity model for the crust and mantle. Topography is plotted above each cross-section. BS = Brazilian Shield, GS = Guyana Shield, SFC = São Francisco Craton, AB = Amazonian Basin, PtB = Pantanal Basin and TP = Tocantins Province, as shown in Fig. 1. The ISC-EHB seismicity (ISC 2023; Engdahl et al. 2020; Weston et al. 2018; Engdahl et al. 1998) is shown as black dots.

However, Celli et al. (2020) and Ciardelli et al. (2022) do not see systematic differences between both shields.

5.2 Depth inversion

At 15 km depth (Fig. 9), we see a good correlation with known crustal tectonic units of South America. High velocities (~2 to 4% V_{SV}) in the crust inside the AC (BS and GS), SFC, PtB's basement and RC (small-scale high to the south of the PtB). We also see lower velocities (~-2 to -6% V_{SV}) in the PB and PrB sedimentary basins and the Andes. In the Caribbean, we see a spotted pattern that is expected, given the thinner oceanic crust. We observe a high-velocity anomaly between the PB and CPB (~1% V_{SV}). The surface-wave Ambient Noise Tomography of Shirzad et al. (2020) V_{SV} inversion also shows a high-velocity anomaly in the PtB and a low-velocity anomaly in the PB at 20 km. The authors also observe a high-velocity anomaly in the transition between the PB and CPB basins at 30 km.

At 60 km depth, we mainly see the contrast between the high velocities of the cratonic SAP and the low velocities of the crustal roots of the Andes. For the cratonic area, the main characteristic is the difference between the average velocity in the northern and southern parts of the AC (profile B-B' in Fig. 11). The northern shield (GS) seems to have lower average velocities than the south (BS) and this difference is consistent with depth in our inversions (Fig. S8 and Fig. 11 A-A'). Therefore, structural differences could exist between the northern and southern Amazonian cratons, which will be discussed in more detail below.

At 100 km depth, we mostly observe lithospheric features and the distinction between the cratonic SAP and the Andean and subandean regions. An important characteristic is the lower shear velocities ($\sim$-4% V_{SV}) beneath the PtB and CPB. This low-velocity zone is well delineated in our model and correlates well with the shallow LAB in Priestley et al. (2018) and Ciardelli et al. (2022) . It will be discussed in more detail below. We observe high-velocity anomalies ($\sim$5% V_{SV}) in the AC and SFC that are coherent with the areas of deepest LAB ($\sim$180 km) for those cratons (Priestley et al. 2018; Ciardelli et al. 2022). The lower velocities ($\sim$-2% V_{SV}) in the MP also correlate well with the shallow LAB ($\sim$70 to 90 km) expected in this area (Priestley et al. 2018; Ciardelli et al. 2022). We also see higher velocities ($\sim$2% V_{SV}) under the PB that can be attributed to the PC underneath the PB. Profile B-B' (Fig. 11) shows the transition between the $\sim$100 km LAB under the subandean region and the PtB (distances between 550 to 1,750 km) to the $\sim$200 km LAB to the east. Profile C-C' (Fig. 11) shows the cratonic roots of the AC and PC cratons from 1,500 km onward. We also observe crustal and lithospheric thinning near the TBL in the TP (around 3,500 km in Profile C-C'). The thin crust was also observed in seismic refraction profiles (Berrocal et al. 2004) and receiver functions (Assumpção et al. 2013b; Assumpção et al. 2013a; Rivadeneyra-Vera et al. 2019). Assumpção and Sacek (2013) proposed that crustal thinning could produce higher stresses in the upper crust, which would explain the higher seismicity observed in the area. Lithospheric thinning was also suggested as an additional contributor to the concentration of stresses in the upper crust. This result is in agreement with the low-velocity anomalies observed in the upper mantle from P-wave tomography (Rocha et al. 2016; Assumpção et al. 2004).

At 300 km depth, the anomalies are generally well correlated with those found in the Adjunct Tomography of Ciardelli et al. 2022. We resolve general high-velocity anomalies to the west, correlating well with the subduction of the Nazca plate (Slab2 model in Fig. 9 by Hayes et al. 2018). We can observe the slab in the Central Andes ($\sim$15°S 70°W in Fig. 9 at 300 km) where we see a pronounced high-velocity anomaly ($\sim$6% V_{SV}). East of the slab ($\sim$26°S 60°W) we observe a high-velocity anomaly ($\sim$3% V_{SV}) similar to Ciardelli et al. 2022 model. To the south of 35°S the slab is not seen clearly given the poor resolution at the longer periods, as shown in the checkerboard tests in Fig. 5. In NE Brazil we observe a high-velocity anomaly in the BP, similar to Celli et al. (2020), but different from the low velocities of Ciardelli et al. 2022. However, our model is on the edge of its resolution in that region (Fig. 5) to resolve this difference.

5.3 Crustal Thickness

We observe thick crust in the Andes (>55 km) and the thin oceanic crust in the Caribbean (<25 km) as major features (Fig. 10). More importantly, we can resolve smaller-scale features, such as thinner crust east of the PtB and thicker crust inside the PB. Those are examples of smaller-scale features that correlate well with the thickness map of Rivadeneyra-Vera et al. (2019). The thin crust in the PtB could have been caused by a delamination near the TBL as hypothesized by Cedraz et al. (2020). The thicker crust beneath the PB is usually associated with its very thick sedimentary layer (up to 7 km). Overall, our Moho map is consistent with the known crust thickness in South America (derived mainly from receiver functions), indicating that the depth inversion solutions should be useful in areas where no local data is available, such as the Amazon region.

5.4 Pantanal Basin and thin lithosphere

Low velocities ($\sim$-4% V_{SV}) can be seen inside and to the SW of the PtB (around 19°S 59°W) at 100 km (Fig. 9 and 11B-B'). This low-velocity anomaly has been observed in several tomographic models (e.g. Ciardelli et al. 2022; Nascimento et al. 2022; Celli et al. 2020; Rocha et al. 2019; Lee et al. 2001; Feng et al. 2004) which makes it a major feature of the upper mantle of the South American Lithosphere. We observe this anomaly from around 70 to 200 km depth (Fig. S8). Both the global model of Priestley et al. (2018) and continental tomography of Ciardelli et al. (2022) show a thin lithosphere ($\sim$100 km) in this area. Those results favor the hypothesis that these upper mantle low velocities are related to a shallow asthenosphere. In this area, the anisotropy fast direction (Fig. 7 at 100 s) shows an E-W trend just east of the Andes, parallel to the motion of the Nazca Plate relative to the South American Plate (Gripp and Gordon 2002). A change to NE-SW trend, following the low-velocity anomaly under the PtB, is observed and it is consistent with mantle flow deflected by the PC cratonic root, as suggested by Melo et al. (2018) and Assumpcao et al. (2011). However, we do not observe the NW-SE directions south of the PC, as observed by Melo et al. (2018) and Assumpcao et al. (2011). This could be in part due to low resolution south of 32°S or due to the mantle flow in this area being deeper and not affecting our azimuthal anisotrophy at 100 s.

5.5 Amazonian Craton

Geochronologically, the AC is thought to be formed by the crustal accretion during different orogenic cycles (Santos et al. 2000; Santos et al. 2006). The oldest provinces (Santos et al. 2000) are in the eastern part of the craton, such as the Carajás-Imataca (3.0 to 2.5 Ga). The eastern region of the Guyana Shield is mainly composed of the younger Transamazonic province (2.25 to 2 Ga).

Both regional and global scale tomography models show high-velocity shear wave anomalies around 100 km depth in the eastern regions of both shields (Ciardelli et al. 2022; Celli et al. 2020; Feng et al. 2004; Feng et al. 2007; Lebedev and Hilst 2008) relating it to a thicker cratonic root of the oldest provinces. LAB models derived from shear-wave velocities provide different accounts of the cratonic roots of each shield. Priestley et al.

(2018) show a lithosphere 180 km thick for both shields. On the other hand, Ciardelli et al. (2022) show in the eastern Guyana Shield a lithosphere ∼110 km thick while the eastern Central Brazil Shield has a ∼160 to 180 km lithosphere. Surface waves group velocities at 100 s tend to be lower in the north and higher in the south (e.g. Nascimento et al. 2022; Rosa et al. 2016), which correspond roughly to a 100 km depth maximum sensitivity for shear-wave velocity kernels.

At 100 km, we observe high-velocity anomalies (∼5% V_{SV}) in the eastern BS and no anomalies in the eastern GS. It is possible that the lack of sufficient azimuthal coverage in the area, due to a lack of stations, makes it difficult to resolve this dispute. However, our checkerboard tests can reasonably recover anomalies this region larger than 6° (Fig. 5). Therefore, even if small-scale anomalies can not be recovered due to poor coverage, it is possible that the average seismic properties in the GS are preserved in our model, especially given that the lack of a high-velocity anomaly is constant with depth (Fig. S8 and Fig. 11A-A'). The average low V_{SV} in our model could indicate that a cratonic root never formed or it was reworked by volcanic activities during the formation of the GS, such as the back-arc extension around 2.2 Ga in French Guyana (Santos et al. 2000) or by the CAMP magmatism around 200 Ma (Deckart et al. 2005; Marzoli et al. 2018).

6 Conclusion

We presented Rayleigh-wave phase-velocity maps for periods between 5 and 200 s for isotropic and anisotropic components (Fig. 7). We used an automatic implementation of the two-station method to automatically compute and apply quality control to dispersion curves throughout South America (Soomro et al. 2016). This method allowed measurements across a broader range of periods than previous works (Feng et al. 2004; Rosa et al. 2016; Lee et al. 2001; Heintz et al. 2005; Feng et al. 2007; Nascimento et al. 2022). We also used the isotropic component to invert a 3-D shear-wave velocity model between 15 and 300 km (Fig. 9) following a particle-swarm-optimization technique by El-Sharkawy et al. (2020). We also derived a Moho map for South America from this last inversion (Fig. 10) that showed good agreement with the crustal thickness map from Rivadeneyra-Vera et al. (2019) and can help complement the Moho thickness data in areas of poor station coverage for Receiver Function studies.

The lithospheric anisotropy is mostly understood by SKS studies in the South American Platform (Melo et al. 2018; Assumpcao et al. 2011; Assumpção et al. 2006). However, such studies have difficulty observing large-scale trends in the anisotropy, given the poor coverage of seismographic stations inside the South American Platform. We were able to compute the anisotropies in areas of previously poor coverage, such as the Amazonian Basin, Amazon Craton and Pantanal Basin. For the 15- and 30 s (Fig. 7) maps, we observed the azimuthal anisotropy fast direction being parallel to the strike of the Andean Orogeny, which is consistent with the observed compression of the South American Plate from the subduction of the Nazca Slab (e.g. Assumpção et al. 2016). For 100 s (Fig. 7), the anisotropy fast direction shows an E-W trend just east of the Andes, parallel to the motion of the Nazca Plate relative to the South American Plate (Gripp and Gordon 2002). A change to NE-SW trend, following the low-velocity anomaly under the Pantanal Basin (e.g. $\sim$4% V_{SV} in Fig. 9 at 100 km), is observed and it is consistent with mantle flow deflected by the Paranapanema cratonic root. However, we do not observe the NW-SE directions south of the Paranapanema block, as observed by Melo et al. (2018) and Assumpcao et al. (2011).

We observed systematic differences between the Guyana Shield and Central Brazil Shield (e.g. Fig. 9 at 100 km) that were constant across different depths (Fig. 11A-A' and Fig. S8). Our model indicates that, on average, the Guyana Shield has lower shear-wave velocities than the Central Brazil Shield (difference of $\sim$3% V_{SV}). This difference could be due to some rework of the lithospheric root of the Guyana Shield by some magmatic event, such as the Central Atlantic Magmatic Province (CAMP).

We also observed a low crustal and LAB thickness (profile C-C' in Fig. 11) in the Tocantins Province, an area of known high seismicity in Brazil (e.g. Agurto-Detzel et al. 2017). The thin crust was observed previously in seismic refraction profiles (Berrocal et al. 2004) and receiver functions (Assumpção et al. 2013a; Assumpção et al. 2013b; Rivadeneyra-Vera et al. 2019). Assumpção and Sacek (2013) proposed that crustal and lithospheric thinning could contribute to the high seismicity observed in this area by producing higher stresses in the upper crust.

7 Data Availability Statement

The downloaded earthquake data is publicly available on IRIS FDSNWS service[1], with exception of the XC network from the Brazilian Seismographic Network (Bianchi et al. 2018) that is publicly available on the Seismology Center of the University of São Paulo FDSNWS service[2].

8 Acknowledgments

This study was financed by the *Coordenação de Aperfeiçoamento de Pessoal de Nível Superior* (CAPES) - Brazil by the grants from the *Programa de Excelência Acadêmica* (PROEX - 88887.464480/2019-00) and *Programa Institucional de Internacionalização* (PrInt - 88887.694554/2022-00). We also would like to thank the Kiel University Computing Centre for supporting this study through high-performance computing resources.

[1] https://service.iris.edu/fdsnws/
[2] http://www.moho.iag.usp.br/fdsnws/

12 Appendix C - Networks

Tab. 1: Networks used in this work. The information was extracted from the FDSN website (https://www.fdsn.org/networks/). Start and End years are the operation time of the network. Networks with DOI available at the FDSN website are cited in the last column.

FDSN Code	Network Name	Operated by	Start Year	End Year	Citation
1P	Solid Earth response of the Patagonia Andes to post-Little Ice Age glacial retreat (Patagonia GIA)	Washington University in St. Louis (WUSTL), United States of America	2018	2021	Douglas Wiens and Maria Beatrice Magnani (2018)
3A	Maule Aftershock Deployment (UK)	University of Liverpool, United Kingdom	2010	2012	-
8A	IPY: Stability of Larsen C Ice Shelf in a Warming Climate (Larsen Ice Shelf)	IRIS PASSCAL Instrument Center @ New Mexico Tech, United States of America	2008	2009	Konrad Steffen and Daniel McGrath (2008)
8G	2016 Pedernales Earthquake Aftershock Deployment Ecuador (Ecuador RAMP)	Lehigh University, United States of America	2016	2017	Anne Meltzer and Susan Beck (2016)

FDSN Code	Network Name	Operated by	Start Year	End Year	Citation
AF	AfricaArray	Penn State University, United States of America	2004	-	Penn State University (2004)
AI	Antarctic Seismographic Argentinean Italian Network - ASAIN	Istituto Nazionale di Oceanografia e di Geofisica Sperimentale (OGS), Italy	1992	-	Istituto Nazionale di Oceanografia e di Geofisica Sperimentale (1992)
AS	Modified High Gain Long Period Observatory (ASRO)	Albuquerque Seismological Laboratory/USGS (ASL), United States of America	1976	1993	Albuquerque Seismological Laboratory (ASL)/USGS (1976)
AY	Haitian Seismic Network	Bureau of Mines and Energy, Haiti	2010	-	-
BL	Brazilian Lithospheric Seismic Project (BLSP)	Universidade de Sao Paulo, USP, Brazil	1988	-	-
BR	University of Brasilia Seismic Network	University of Brasilia, Brazil	1995	-	-
C	Chilean National Seismic Network	Universidad de Chile, Dept de Geofisica (DGF), Chile	1991	-	-
C1	Red Sismologica Nacional (RSN)	Universidad de Chile (UCH), Chile	2012	-	Universidad de Chile (2012)

FDSN Code	Network Name	Operated by	Start Year	End Year	Citation
CM	Red Sismológica Nacional de Colombia (CM)	Servicio Geológico Colombiano (SGC), Colombia	1993	-	Servicio Geológico Colombiano (1993)
CN	Canadian National Seismograph Network (CNSN)	Natural Resources Canada (NRCAN), Canada	1975	-	Natural Resources Canada (1975)
CU	Caribbean Network	Albuquerque Seismological Laboratory/USGS (ASL), United States of America	2006	-	Albuquerque Seismological Laboratory (ASL)/USGS (2006)
CW	Servicio Sismologico Nacional de Cuba (SSNC)	National Centre for Seismological Research (CENAIS), Cuba	1998	-	National Centre for Seismological Research (CENAIS Cuba) (1998)
CY	Cayman Islands	Cayman Islands Government, Cayman Islands	2006	-	-
DR	Centro Nacional de Sismologia (CNS-UASD)	National Seismological Centre (NSC), Nepal	1998	-	National Seismological Centre (1998)

FDSN Code	Network Name	Operated by	Start Year	End Year	Citation
DW	Digital World-Wide Standardized Seismograph Network (DWWSSN)	Albuquerque Seismological Laboratory/USGS (ASL), United States of America	1980	1994	Albuquerque Seismological Laboratory (ASL)/USGS (1980)
EC	Ecuador Seismic Network	Instituto Geofisico Escuela Politecnica Nacional (IG-EPN), Ecuador	2002	-	-
G	GEOSCOPE - French Global Network of Seismological Broadband Stations	Ecole et Observatoire des Sciences de la Terre (EOST), France, Institut de Physique du Globe de Paris (IPGP), France, Observatoire Geoscope, France	1982	-	Institut de physique du globe de Paris (IPGP) and École et Observatoire des Sciences de la Terre de Strasbourg (EOST) (1982)
GE	GEOFON	GEOFON Program (GFZ-Potsdam, Germany), Germany	1991	-	GEOFON Data Centre (1993)

FDSN Code	Network Name	Operated by	Start Year	End Year	Citation
GL	Guadeloupe Seismic and Volcano Observatory Network (OVSG)	Institut de Physique du Globe de Paris (IPGP), France	1950	-	Institut De Physique Du Globe De Paris (IPGP) (2020a)
GT	Global Telemetered Seismograph Network (USAF/USGS) (GTSN)	Albuquerque Seismological Laboratory/USGS (ASL), United States of America	1993	-	Albuquerque Seismological Laboratory (ASL)/USGS (1993)
II	Global Seismograph Network - IRIS/IDA (GSN)	Scripps Institution of Oceanography (SIO), United States of America	1986	-	Scripps Institution of Oceanography (1986)
IU	Global Seismograph Network (GSN - IRIS/USGS)	Albuquerque Seismological Laboratory/USGS (ASL), United States of America	2014	2014	Albuquerque Seismological Laboratory/USGS (2014)
JM	Jamaica Seismograph Network	University of the West Indies - Mona, Jamaica	1985	-	-
MC	Montserrat CALIPSO Borehole Network	University of Texas-Arlington, United States of America	2008	-	-

FDSN Code	Network Name	Operated by	Start Year	End Year	Citation
MQ	Martinique Seismic and Volcano Observatory Network (OVSM)	Institut de Physique du Globe de Paris (IPGP), France	1935	-	Institut De Physique Du Globe De Paris (IPGP) (2020b)
NA	Caribbean Netherlands Seismic Network	Royal Netherlands Meteorological Institute (KNMI), Netherlands	2006	-	KNMI (2006)
NB	Northeastern Brazil UFRN	Universidade Federal do Rio Grande do Norte (UFRN), Brazil	2006	-	-
ON	Rede Sismográfica do Sul e do Sudeste (RSIS)	Observatório Nacional, Rio de Janeiro, RJ, Brazil	2011	-	Observatório Nacional, Rio de Janeiro (2011)
PR	Puerto Rico Seismic Network & Puerto Rico Strong Motion Program (PRSN and PRSMP)	University of Puerto Rico (UPR), United States of America	1986	-	University of Puerto Rico (1986)
TO	Tectonic Observatory - MASE, VEOX , PeruSE, CCSE	California Institute of Technology (CIT), United States of America	2004	-	MASE Caltech (2007)

FDSN Code	Network Name	Operated by	Start Year	End Year	Citation
TR	Eastern Caribbean Seismograph Network	University of the West Indies, Seismic Research Centre, Trinidad and Tobago	1965	-	-
VL	Vale SA Network	Universidade de Sao Paulo, USP, Brazil	2017	-	Universidade de Sao Paulo (2017)
WA	West Central Argentina Network	Universidad Nacional de San Juan (UNSJ), Argentina	1958	-	-
WC	Curacao Seismic Network	Meteorologische Dienst Curacao, Curaçao	2006	-	-
WI	West Indies French Seismic Network	Institut de Physique du Globe de Paris (IPGP), France	2008	-	Institut De Physique Du Globe De Paris (IPGP) (2008)
X1	Aysen Chile Aftershock Deployment (ACAD)	University of Liverpool, United Kingdom	2007	2008	-
X6	SLIP - Seismic Lithospheric Imaging of the Puna Plateau (SLIP/Missouri)	University of Missouri (MU), United States of America	2007	2009	Eric Sandvol and Larry Brown (2007)

FDSN Code	Network Name	Operated by	Start Year	End Year	Citation
XC	Pantanal, Chaco and Paraná structural studies network (PCPB)	Institute of Astronomy, Geophysics & Atmospheric Science, Univ. of Sao Paulo (IAG-USP), Brazil	2016	2024	Marcelo Sousa de Assumpção and Marcelo Belentani de Bianchi (2016)
XE	BBand Andean Joint Exp. / Seismic Exploration of Deep Andes (Banjo/SEDA)	IRIS/PASSCAL	1994	1995	Silver et al. (1994)
XN	Bolivar: Western Venezuela (Bolivar West)	Rice University, United States of America	2008	2009	Alan Levander (2008)
XP	Investigating the relationship between pluton growth and volcanism at two active intrusions in the central Andes (PLUTONS)	University of Alaska, Fairbanks (UAF), United States of America	2010	2013	Michael West and Douglas Christensen (2010)

FDSN Code	Network Name	Operated by	Start Year	End Year	Citation
XS	Maule Earthquake (Chile) Aftershock Experiment (MAULE)	Reseau sismologique et géodésique français (RESIF), France	2010	2011	Vilotte and RESIF (2011)
Y3	Studies of crust and upper mantle structure, mantle flow and geodynamics of the Chile Ridge subduction zone	University of Florida, United States of America	2007	2007	Ray Russo (2007)
YC	Slab Geometry in the Southern Andes	IRIS/PASSCAL	2000	2002	Susan Beck et al. (2000)
YJ	Studies of crust and upper mantle structure, mantle flow and geodynamics of the Chile Ridge subduction zone	IRIS/PASSCAL	2004	2006	Ray Russo (2004)

FDSN Code	Network Name	Operated by	Start Year	End Year	Citation
YM	An Integrated Analysis of Low-Frequency Seismicity at Villarrica Volcano, Chile	Michigan Technological University (MTU), United States of America	2010	2012	Gregory Waite (2010)
YN	Seismic Experiment in Patagonia and Antarctica (SEPA II)	Washington University in St. Louis (WUSTL), United States of America	1999	2004	-
YS	The life cycle of Andean volca-noes:Combining space-based and field studies (ANDIVOLC)	Cornell University, United States of America	2009	2013	Matt Pritchard (2009)
YU	Caribbean-Merida Andes Experiment (CARMA)	Rice University, United States of America	2016	2018	Alan Levander (2016)
ZC	Greater Antilles Seismic Program (GrASP aka GASP)	Baylor University, United States of America	2013	2032	Jay Pulliam (2013)

FDSN Code	Network Name	Operated by	Start Year	End Year	Citation
ZD	PerU Lithosphere and Slab Experiment (PULSE/UNC)	Carnegie Institution for Science (CIS), United States of America	2010	2013	Lara Wagner et al. (2010)
ZG	Central Andean Uplift and the Geodynamics of the High Topography (CAUGHT)	University of Arizona, United States of America	2010	2012	Susan Beck et al. (2010)
ZL	Lithospheric Structure and Deformation of the Flat Slab Region of Argentina (SIEMBRA)	University of Arizona, United States of America	2007	2009	Susan Beck and George Zandt (2007)
ZN	Meteo Aruba/Rice Univ	-	2008	2009	-
ZR	Laguna del Maule seismic imaging (LaMa)	University of Wisconsin, Madison, United States of America	2015	2018	Cliff Thurber (2015)

References

Affonso, G. M. P. C., M. P. Rocha, I. S. L. Costa, M. Assumpção, R. A. Fuck, D. F. Albuquerque, D. E. Portner, E. E. Rodríguez, and S. L. Beck (2021). "Lithospheric Architecture of the Paranapanema Block and Adjacent Nuclei Using Multiple-Frequency P -Wave Seismic Tomography". In: *Journal of Geophysical Research: Solid Earth* 126.4. ISSN: 2169-9313. DOI: 10.1029/2020JB021183. URL: https://agupubs.onlinelibrary.wiley.com/doi/10.1029/2020JB021183.

Agurto-Detzel, Hans, Marcelo Assumpção, Marcelo Bianchi, and Marlon Pirchiner (2017). "Intraplate seismicity in mid-plate South America: correlations with geophysical lithospheric parameters". In: *Geological Society, London, Special Publications* 432.1, pp. 73–90. ISSN: 0305-8719. DOI: 10.1144/SP432.5. URL: https://www.lyellcollection.org/doi/10.1144/SP432.5.

Alan Levander (2008). *Bolivar: Western Venezuela*. DOI: 10.7914/SN/XN_2008. URL: https://www.fdsn.org/networks/detail/XN{_}2008/.

Alan Levander (2016). *Caribbean-Merida Andes Experiment*. DOI: 10.7914/SN/YU_2016. URL: https://www.fdsn.org/networks/detail/YU{_}2016/.

Albuquerque Seismological Laboratory (ASL)/USGS (1976). *Modified High Gain Long Period Observatory*. DOI: 10.7914/SN/AS. URL: https://www.fdsn.org/networks/detail/AS/.

Albuquerque Seismological Laboratory (ASL)/USGS (1980). *Digital World-Wide Standardized Seismograph Network*. DOI: 10.7914/SN/DW. URL: https://www.fdsn.org/networks/detail/DW/.

Albuquerque Seismological Laboratory (ASL)/USGS (1993). *Global Telemetered Seismograph Network (USAF/USGS)*. DOI: 10.7914/SN/GT. URL: https://www.fdsn.org/networks/detail/GT/.

Albuquerque Seismological Laboratory (ASL)/USGS (2006). *Caribbean Network*. DOI: 10.7914/SN/CU. URL: https://www.fdsn.org/networks/detail/CU/.

Albuquerque Seismological Laboratory/USGS (2014). “Global Seismograph Network (GSN - IRIS/USGS) [Data Set]”. In: *International Federation of Digital Seismograph Networks.* DOI: https://doi.org/10.7914/SN/IU.

Almeida, F. F. M., B. B. Brito Neves, and C. D. R. Carneiro (2000). “The origin and evolution of the South American Platform”. In: *Earth-Science Reviews* 50.1-2, pp. 77–111.

Almeida, F.F.M., Y. Hasui, B.B. Brito Neves, and R.A. Fuck (1981). “Brazilian structural provinces: An introduction”. In: *Earth-Science Reviews* 17.1-2, pp. 1–29. ISSN: 00128252. DOI: 10.1016/0012-8252(81)90003-9. URL: https://linkinghub.elsevier.com/retrieve/pii/0012825281900039.

Ammon, C. J., G. E. Randall, and G. Zandt (1990). “On the nonuniqueness of receiver function inversions”. In: *Journal of Geophysical Research: Solid Earth* 95.B10, pp. 15303–15318. ISSN: 01480227. DOI: 10.1029/jb095ib10p15303.

Anderson, Megan L., George Zandt, Enrique Triep, Matthew Fouch, and Susan Beck (2004). “Anisotropy and mantle flow in the Chile-Argentina subduction zone from shear wave splitting analysis”. In: *Geophysical Research Letters* 31.23. ISSN: 0094-8276. DOI: 10.1029/2004GL020906. URL: https://agupubs.onlinelibrary.wiley.com/doi/10.1029/2004GL020906.

Anne Meltzer and Susan Beck (2016). *2016 Pedernales Earthquake Aftershock Deployment Ecuador*. DOI: 10.7914/SN/8G_2016. URL: https://www.fdsn.org/networks/detail/8G{_}2016/.

Assumpção, M., M. An, M. Bianchi, G. S. França, M. Rocha, J. R. Barbosa, and J. Berrocal (2004a). “Seismic studies of the Brasília fold belt at the western border of the São Francisco Craton, Central Brazil, using receiver function, surface-wave dispersion and teleseismic tomography”. In: *Tectonophysics* 388.1-4, pp. 173–185. DOI: 10.1016/j.tecto.2004.04.029. URL: www.elsevier.com.

Assumpção, M., M. Bianchi, J. Julià, F. L. Dias, G. Sand França, R. Nascimento, S. Drouet, C. G. Pavão, D. F. Albuquerque, and A. E. V. Lopes (2013a). “Crustal thickness map of Brazil: Data compilation and main features". In: *Journal of South American Earth Sciences* 43, pp. 74–85. ISSN: 08959811. DOI: 10.1016/j.jsames.2012.12.009.

Assumpção, M., F. L. Dias, I. Zevallos, and J. B. Naliboff (2016). "Intraplate stress field in South America from earthquake focal mechanisms". In: *Journal of South American Earth Sciences* 71, pp. 278–295. ISSN: 08959811. DOI: 10.1016/j.jsames.2016.07.005.

Assumpção, M., M. Feng, A. Tassara, and J. Julià (2013b). *Models of crustal thickness for South America from seismic refraction, receiver functions and surface wave tomography.* DOI: 10.1016/j.tecto.2012.11.014.

Assumpcao, M., M. Guarido, S. van der Lee, and J. C. Dourado (2011). "Upper-mantle seismic anisotropy from SKS splitting in the South American stable platform: A test of asthenospheric flow models beneath the lithosphere". In: *Lithosphere* 3.2, pp. 173–180. ISSN: 1941-8264. DOI: 10.1130/L99.1. URL: https://pubs.geoscienceworld.org/lithosphere/article/3/2/173-180/145585.

Assumpção, M., M. Heintz, A. Vauchez, and M. Silva (2006). "Upper mantle anisotropy in SE and Central Brazil from SKS splitting: Evidence of asthenospheric flow around a cratonic keel". In: *Earth and Planetary Science Letters* 250.1-2, pp. 224–240. ISSN: 0012821X. DOI: 10.1016/j.epsl.2006.07.038. URL: https://linkinghub.elsevier.com/retrieve/pii/S0012821X06005437.

Assumpção, M. and V. Sacek (2013). "Intra-plate seismicity and flexural stresses in central Brazil". In: *Geophysical Research Letters* 40.3, pp. 487–491. ISSN: 00948276. DOI: 10.1002/grl.50142. URL: http://doi.wiley.com/10.1002/grl.50142.

Assumpção, Marcelo, Martin Schimmel, Christian Escalante, José Roberto Barbosa, Marcelo Rocha, and Lucas V. Barros (2004b). "Intraplate seismicity in SE Brazil: stress concentration in lithospheric thin spots". In: *Geophysical Journal International* 159.1, pp. 390–399. ISSN: 0956540X. DOI: 10.1111/j.1365-246X.2004.02357.x. URL: https://academic.oup.com/gji/article-lookup/doi/10.1111/j.1365-246X.2004.02357.x.

Bensen, G. D., M. H. Ritzwoller, M. P. Barmin, A. L. Levshin, F. Lin, M. P. Moschetti, N. M. Shapiro, and Y. Yang (2007). "Processing seismic ambient noise data to obtain reliable broad-band surface wave dispersion measurements". In: *Geophysical Journal International*. ISSN: 0956540X. DOI: 10.1111/j.1365-246X.2007.03374.x.

Berrocal, Jesus, Yara Marangoni, Nelsí C. de Sá, Reinhardt Fuck, José E.P. Soares, E. Dantas, Fábio Perosi, and Celia Fernandes (2004). "Deep seismic refraction and gravity crustal model and tectonic deformation in Tocantins Province, Central Brazil". In: *Tectonophysics* 388.1-4, pp. 187–199. ISSN: 00401951. DOI: 10.1016/j.tecto.2004.04.033. URL: https://linkinghub.elsevier.com/retrieve/pii/S0040195104002665.

Bianchi, M., M. Assumpção, M. P. Rocha, J. M. Carvalho, P. A. Azevedo, S. L. Fontes, F. L. Dias, J. M. Ferreira, A. F. Nascimento, M. V. Ferreira, and I. S. L. Costa (2018). "The Brazilian Seismographic Network (RSBR): Improving Seismic Monitoring in Brazil". In: *Seismological Research Letters* 89.2A, pp. 452–457. ISSN: 0895-0695. DOI: 10.1785/0220170227. URL: https://pubs.geoscienceworld.org/ssa/srl/article/89/2A/452/528165/The-Brazilian-Seismographic-Network-RSBR-Improving.

Bologna, M. S., G. N. Dragone, R. Muzio, E. Peel, P. Nuñez-Demarco, and N. Ussami (2019). "Electrical Structure of the Lithosphere From Rio de la Plata Craton to Paraná Basin: Amalgamation of Cratonic and Refertilized Lithospheres in SW Gondwanaland". In: *Tectonics* 38.1, pp. 77–94. ISSN: 02787407. DOI: 10.1029/2018TC005148. URL: http://doi.wiley.com/10.1029/2018TC005148.

Boness, Naomi L. and Mark D. Zoback (2004). "Stress-induced seismic velocity anisotropy and physical properties in the SAFOD Pilot Hole in Parkfield, CA". In: *Geophysical Research Letters* 31.15. ISSN: 0094-8276. DOI: 10.1029/2003GL019020. URL: https://agupubs.onlinelibrary.wiley.com/doi/10.1029/2003GL019020.

Boness, Naomi L. and Mark D. Zoback (2006). "A multiscale study of the mechanisms controlling shear velocity anisotropy in the San Andreas Fault Observatory at Depth".

In: *GEOPHYSICS* 71.5, F131–F146. ISSN: 0016-8033. DOI: 10.1190/1.2231107. URL: https://library.seg.org/doi/10.1190/1.2231107.

Catto, A. J. (1975). "Análise Geológica e Geofísica da Bacia do Pantanal Matogrossense". In: *internal report, 23 pp., Petrobrás, Rio de Janeiro, Brazil*.

Cedraz, V., J. Julià, and M. Assumpção (2020). "Joint inversion of receiver functions and surface-wave dispersion in the Pantanal Wetlands: Implications for basin formation". In: *Journal of Geophysical Research: Solid Earth* 125.2. DOI: 10.1029/2019JB018337.

Celli, N. L., S. Lebedev, A. J. Schaeffer, M. Ravenna, and C. Gaina (2020). "The upper mantle beneath the South Atlantic Ocean, South America and Africa from waveform tomography with massive data sets". In: *Geophysical Journal International* 221.1, pp. 178–204. ISSN: 0956-540X. DOI: 10.1093/gji/ggz574. URL: https://academic.oup.com/gji/article/221/1/178/5697204.

Ciardelli, Caio, Marcelo Assumpção, Ebru Bozdağ, and Suzan van der Lee (2022). "Adjoint Waveform Tomography of South America". In: *Journal of Geophysical Research: Solid Earth* 127.2, pp. 1–36. ISSN: 21699356. DOI: 10.1029/2021JB022575.

Cingolani, C. and L.D. Salda (2000). "Buenos Aires cratonic region". In: *Tectonic Evolution of South America, eds. Cordani et al., 31 st Int.Geological Congr., Rio de Janeiro*, pp. 139–146.

Civiero, Chiara, Sergei Lebedev, Yihe Xu, Raffaele Bonadio, and François Lavoué (2024). "Toward Tectonic-Type and Global 1D Seismic Models of the Upper Mantle Constrained by Broadband Surface Waves". In: *Bulletin of the Seismological Society of America* 114.3, pp. 1321–1346. ISSN: 0037-1106. DOI: 10.1785/0120230295. URL: https://pubs.geoscienceworld.org/bssa/article/114/3/1321/638328/Toward-Tectonic-Type-and-Global-1D-Seismic-Models.

Cliff Thurber (2015). *Laguna del Maule seismic imaging*. DOI: 10.7914/SN/ZR_2015. URL: https://www.fdsn.org/networks/detail/ZR{_}2015/.

Cordani, Umberto G. and Benjamim Bley de Bruto Neves (1982). "THE GEOLOGIC EVOLUTION OF SOUTH AMERICA DURING THE ARCHAEAN AND EARLY PROTEROZOIC". In: *Revista Brasileira de Geociências* 12, pp. 78–88.

Cordani, Umberto G., Victor A. Ramos, Lêda Maria Fraga, Marcelo Cegarra, Inácio Delgado, Kaiser G. de Souza, Francisco Edson M. Gomes, and Carlos Schobbenhaus (2016). *Mapa tectônico da América do Sul*. URL: https://rigeo.sgb.gov.br/handle/doc/16750.

Cordani, Umberto G. and Kei Sato (1999). "Crustal evolution of the South American Platform, based on Nd isotopic systematics on granitoid rocks". In: *Episodes* 22.3, pp. 167–173. ISSN: 0705-3797. DOI: 10.18814/epiiugs/1999/v22i3/003. URL: http://www.episodes.org/journal/view.html?doi=10.18814/epiiugs/1999/v22i3/003.

Cordani, Umberto Giuseppe, Marcio Martins Pimentel, Carlos Eduardo Ganade de Araújo, and Reinhardt Adolfo Fuck (2013). "The significance of the -Transbrasiliano-Kandi tectonic corridor for the amalgamation of West Gondwana". In: *Brazilian Journal of Geology* 43.3, pp. 583–597. ISSN: 2317-4889. DOI: 10.5327/Z2317-48892013000300012. URL: http://bjg.siteoficial.ws/2013/n.3/mM.pdf.

Crampin, Stuart (1987). "Geological and industrial implications of extensive-dilatancy anisotropy". In: *Nature* 328.6130, pp. 491–496. ISSN: 0028-0836. DOI: 10.1038/328491a0. URL: https://www.nature.com/articles/328491a0.

Daly, Michael C., Vander Andrade, Chuck A. Barousse, Rafaela Costa, Kenneth McDowell, Neil Piggott, and Alan J. Poole (2014). "Brasiliano crustal structure and the tectonic setting of the Parnaíba basin of NE Brazil: Results of a deep seismic reflection profile". In: *Tectonics* 33.11, pp. 2102–2120. ISSN: 0278-7407. DOI: 10.1002/2014TC003632. URL: https://onlinelibrary.wiley.com/doi/10.1002/2014TC003632.

Debayle, Eric, Fabien Dubuffet, and Stéphanie Durand (2016). "An automatically updated S -wave model of the upper mantle and the depth extent of azimuthal anisotropy". In: *Geophysical Research Letters* 43.2, pp. 674–682. ISSN: 0094-8276. DOI: 10.1002/2015GL067329. URL: https://agupubs.onlinelibrary.wiley.com/doi/10.1002/2015GL067329.

Deckart, Katja, Hervé Bertrand, and Jean-Paul Liégeois (2005). "Geochemistry and Sr, Nd, Pb isotopic composition of the Central Atlantic Magmatic Province (CAMP) in Guyana and Guinea". In: *Lithos* 82.3-4, pp. 289–314. ISSN: 00244937. DOI: 10.1016/j.lithos.2004.09.023. URL: https://linkinghub.elsevier.com/retrieve/pii/S0024493705000204.

Deschamps, Frédéric, Sergei Lebedev, Thomas Meier, and Jeannot Trampert (2008). "Azimuthal anisotropy of Rayleigh-wave phase velocities in the east-central United States". In: *Geophysical Journal International* 173.3, pp. 827–843. ISSN: 0956540X. DOI: 10.1111/j.1365-246X.2008.03751.x.

Douglas Wiens and Maria Beatrice Magnani (2018). *Solid Earth response of the Patagonia Andes to post-Little Ice Age glacial retreat.* DOI: 10.7914/SN/1P_2018. URL: https://www.fdsn.org/networks/detail/1P{_}2018/.

Dragone, G. N., N. Ussami, M. E. Gimenez, F. G. Lince Klinger, and C. A. M. Chaves (2017). "Western Paraná suture/shear zone and the limits of Rio Apa, Rio Tebicuary and Rio de la Plata cratons from gravity data". In: *Precambrian Research* 291, pp. 162–177. DOI: 10.1016/j.precamres.2017.01.029.

Dziewonski, Adam M. and Don L. Anderson (1981). "Preliminary reference Earth model". In: *Physics of the Earth and Planetary Interiors* 25.4, pp. 297–356. ISSN: 00319201. DOI: 10.1016/0031-9201(81)90046-7. URL: https://linkinghub.elsevier.com/retrieve/pii/0031920181900467.

Eberhart, R. and J. Kennedy (1995). "A new optimizer using particle swarm theory". In: *In MHS'95. Proceedings of the sixth international symposium on micro machine and human science*, pp. 39–43.

El-Sharkawy, Amr, Thomas Meier, Sergei Lebedev, Jan H. Behrmann, Mona Hamada, Luigia Cristiano, Christian Weidle, and Daniel Köhn (2020). "The Slab Puzzle of the Alpine-Mediterranean Region: Insights From a New, High-Resolution, Shear Wave Velocity Model of the Upper Mantle". In: *Geochemistry, Geophysics, Geosystems* 21.8. ISSN: 15252027. DOI: 10.1029/2020GC008993.

Endrun, Brigitte, Sergei Lebedev, Thomas Meier, Céline Tirel, and Wolfgang Friederich (2011). “Complex layered deformation within the Aegean crust and mantle revealed by seismic anisotropy”. In: *Nature Geoscience* 4.3, pp. 203–207. ISSN: 1752-0894. DOI: 10.1038/ngeo1065. URL: https://www.nature.com/articles/ngeo1065.

Engdahl, E. R., D. Di Giacomo, B. Sakarya, C. G. Gkarlaouni, J. Harris, and D. A. Storchak (2020). “ISC-EHB 1964–2016, an Improved Data Set for Studies of Earth Structure and Global Seismicity”. In: *Earth and Space Science* 7.1. ISSN: 2333-5084. DOI: 10.1029/2019EA000897. URL: https://agupubs.onlinelibrary.wiley.com/doi/10.1029/2019EA000897.

Engdahl, E. Robert, Rob van der Hilst, and Raymond Buland (1998). “Global teleseismic earthquake relocation with improved travel times and procedures for depth determination”. In: *Bulletin of the Seismological Society of America* 88.3, pp. 722–743. ISSN: 1943-3573. DOI: 10.1785/BSSA0880030722. URL: https://pubs.geoscienceworld.org/bssa/article/88/3/722/102761/Global-teleseismic-earthquake-relocation-with.

Eric Sandvol and Larry Brown (2007). *SLIP - Seismic Lithospheric Imaging of the Puna Plateau*. DOI: 10.7914/SN/X6_2007. URL: https://www.fdsn.org/networks/detail/X6{_}2007/.

Feng, Mei, Meijian An, Hulin Zang, Marcelo S Assumpção, Marcelo B Bianchi, George S França, Marcelo P Rocha, Leda S Bettucci, and Carlos A Chaves (2024). “Dynamic evolution of West Gondwana inferred from crustal anisotropy of the South American platform”. In: *Geophysical Journal International* 239.1, pp. 201–217. ISSN: 0956-540X. DOI: 10.1093/gji/ggae267. URL: https://academic.oup.com/gji/article/239/1/201/7725832.

Feng, Mei, Marcelo Assumpção, and Suzan Van der Lee (2004). “Group-velocity tomography and lithospheric S-velocity structure of the South American continent”. In: *Physics of the Earth and Planetary Interiors* 147.4, pp. 315–331. ISSN: 00319201. DOI: 10.

1016 / j . pepi . 2004 . 07 . 008. URL: https : / / linkinghub . elsevier . com / retrieve / pii / S0031920104002924.

Feng, Mei, Suzan van der Lee, and Marcelo Assumpção (2007). "Upper mantle structure of South America from joint inversion of waveforms and fundamental mode group velocities of Rayleigh waves". In: *Journal of Geophysical Research: Solid Earth* 112.B4. ISSN: 0148-0227. DOI: 10.1029/2006JB004449. URL: https://agupubs.onlinelibrary.wiley.com/doi/10.1029/2006JB004449.

Fichtner, Andreas, Laurent Stehly, Laura Ermert, and Christian Boehm (2017). "Generalized interferometry – I: theory for interstation correlations". In: *Geophysical Journal International* 208.2, pp. 603–638. ISSN: 0956-540X. DOI: 10.1093/gji/ggw420. URL: https://academic.oup.com/gji/article-lookup/doi/10.1093/gji/ggw420.

Friedrich, A., F. Krüger, and K. Klinge (1998). "Ocean-generated microseismic noise located with the Gräfenberg array". In: *Journal of Seismology* 2, pp. 47–64.

GEOFON Data Centre (1993). *GEOFON Seismic Network*. DOI: 10.14470/TR560404. URL: http://geofon.gfz-potsdam.de/doi/network/GE.

Gregory Waite (2010). *An Integrated Analysis of Low-Frequency Seismicity at Villarrica Volcano, Chile*. DOI: 10.7914/SN/YM_2010. URL: https://www.fdsn.org/networks/detail/YM{_}2010/.

Gripp, Alice E. and Richard G. Gordon (2002). "Young tracks of hotspots and current plate velocities". In: *Geophysical Journal International* 150.2, pp. 321–361. ISSN: 0956540X. DOI: 10.1046/j.1365-246X.2002.01627.x. URL: https://academic.oup.com/gji/article/150/2/321/603154.

Growdon, Mark A., Gary L. Pavlis, Fenglin Niu, Frank L. Vernon, and Herbert Rendon (2009). "Constraints on mantle flow at the Caribbean–South American plate boundary inferred from shear wave splitting". In: *Journal of Geophysical Research: Solid Earth* 114.B2. ISSN: 0148-0227. DOI: 10.1029/2008JB005887. URL: https://agupubs.onlinelibrary.wiley.com/doi/10.1029/2008JB005887.

Hasterok, Derrick, Jacqueline A. Halpin, Alan S. Collins, Martin Hand, Corné Kreemer, Matthew G. Gard, and Stijn Glorie (2022). "New Maps of Global Geological Provinces and Tectonic Plates". In: *Earth-Science Reviews* 231, p. 104069. ISSN: 00128252. DOI: 10.1016/j.earscirev.2022.104069. URL: https://linkinghub.elsevier.com/retrieve/pii/S0012825222001532.

Hayes, Gavin P., Ginevra L. Moore, Daniel E. Portner, Mike Hearne, Hanna Flamme, Maria Furtney, and Gregory M. Smoczyk (2018). "Slab2, a comprehensive subduction zone geometry model". In: *Science* 362.6410, pp. 58–61. ISSN: 0036-8075. DOI: 10.1126/science.aat4723. URL: https://www.science.org/doi/10.1126/science.aat4723.

Heidbach, Oliver, Mojtaba Rajabi, Karsten Reiter, Moritz Ziegler, and WSM Team (2016). "World Stress Map Database Release 2016". In: *GFZ Data Service*. DOI: http://doi.org/10.5880/WSM.2016.001.

Heintz, Maggy, Eric Debayle, and Alain Vauchez (2005). "Upper mantle structure of the South American continent and neighboring oceans from surface wave tomography". In: *Tectonophysics* 406.1-2, pp. 115–139. ISSN: 00401951. DOI: 10.1016/j.tecto.2005.05.006. URL: https://linkinghub.elsevier.com/retrieve/pii/S0040195105002052.

Heintz, Maggy, Alain Vauchez, Marcelo Assumpção, Guilhem Barruol, and Marcos Egydio-Silva (2003). "Shear wave splitting in SE Brazil: an effect of active or fossil upper mantle flow, or both?" In: *Earth and Planetary Science Letters* 211.1-2, pp. 79–95. ISSN: 0012821X. DOI: 10.1016/S0012-821X(03)00163-8. URL: https://linkinghub.elsevier.com/retrieve/pii/S0012821X03001638.

Heit, B., F. Sodoudi, X. Yuan, M. Bianchi, and R. Kind (2007). "An S receiver function analysis of the lithospheric structure in South America". In: *Geophysical Research Letters* 34.14, p. L14307. ISSN: 0094-8276. DOI: 10.1029/2007GL030317. URL: http://doi.wiley.com/10.1029/2007GL030317.

Hornby, Brian E. (1998). "Experimental laboratory determination of the dynamic elastic properties of wet, drained shales". In: *Journal of Geophysical Research: Solid Earth*

103.B12, pp. 29945–29964. ISSN: 0148-0227. DOI: 10.1029/97JB02380. URL: https://agupubs.onlinelibrary.wiley.com/doi/10.1029/97JB02380.

Hu, Jiashun, Manuele Faccenda, and Lijun Liu (2017). "Subduction-controlled mantle flow and seismic anisotropy in South America". In: *Earth and Planetary Science Letters* 470, pp. 13–24. ISSN: 0012821X. DOI: 10.1016/j.epsl.2017.04.027. URL: http://dx.doi.org/10.1016/j.epsl.2017.04.027.

Institut De Physique Du Globe De Paris (IPGP) (2008). *GNSS, seismic broadband and strong motion permanent networks in West Indies*. DOI: 10.18715/ANTILLES.WI. URL: http://volobsis.ipgp.fr/networks/detail/WI/.

Institut De Physique Du Globe De Paris (IPGP) (2020a). *Seismic, tiltmeter, extensometer, tide , magnetic and weather permanent networks on La Soufrière volcano and Guadeloupe*. DOI: 10.18715/GUADELOUPE.GL. URL: http://volobsis.ipgp.fr/networks/detail/GL/.

Institut De Physique Du Globe De Paris (IPGP) (2020b). *Seismic, tiltmeter, groundwater, magnetic and weather permanent networks on Montagne Pelée volcano and Martinique*. DOI: 10.18715/MARTINIQUE.MQ. URL: http://volobsis.ipgp.fr/networks/detail/MQ/.

Institut de physique du globe de Paris (IPGP) and École et Observatoire des Sciences de la Terre de Strasbourg (EOST) (1982). *GEOSCOPE, French Global Network of broad band seismic stations*. DOI: 10.18715/GEOSCOPE.G. URL: http://geoscope.ipgp.fr/networks/detail/G/.

ISC (2023). *ISC-EHB Dataset*. DOI: https://doi.org/10.31905/PY08W6S3.

Ismail, Walid Ben and David Mainprice (1998). "An olivine fabric database: an overview of upper mantle fabrics and seismic anisotropy". In: *Tectonophysics* 296.1-2, pp. 145–157. ISSN: 00401951. DOI: 10.1016/S0040-1951(98)00141-3. URL: https://linkinghub.elsevier.com/retrieve/pii/S0040195198001413.

Istituto Nazionale di Oceanografia e di Geofisica Sperimentale (1992). *Antarctic Seismographic Argentinean Italian Network - ASAIN*. DOI: 10.7914/SN/AI. URL: https://www.fdsn.org/networks/detail/AI/.

James, David E. and Marcelo Assumpção (1996). "Tectonic implications of S -wave anisotropy beneath SE Brazil". In: *Geophysical Journal International* 126.1, pp. 1–10. ISSN: 0956540X. DOI: 10.1111/j.1365-246X.1996.tb05263.x. URL: https://academic.oup.com/gji/article-lookup/doi/10.1111/j.1365-246X.1996.tb05263.x.

Jay Pulliam (2013). *Greater Antilles Seismic Program*. DOI: 10.7914/SN/ZC_2013. URL: https://www.fdsn.org/networks/detail/ZC{_}2013/.

Julià, J., C. J. Ammon, R. B. Herrmann, and A. M. Correig (2000). "Joint inversion of receiver function and surface wave dispersion observations". In: *Geophysical Journal International* 143.1, pp. 99–112. ISSN: 0956540X. DOI: 10.1046/j.1365-246x.2000.00217.x. URL: https://academic.oup.com/gji/article/143/1/99/894713.

Julià, J., M. Assumpção, and M. P. Rocha (2008). "Deep crustal structure of the Paraná Basin from receiver functions and Rayleigh-wave dispersion: Evidence for a fragmented cratonic root". In: *Journal of Geophysical Research: Solid Earth* 113.B8. ISSN: 0148-0227. DOI: 10.1029/2007JB005374. URL: https://agupubs.onlinelibrary.wiley.com/doi/10.1029/2007JB005374.

Kästle, Emanuel D., Riaz Soomro, Cornelis Weemstra, Lapo Boschi, and Thomas Meier (2016). "Two-receiver measurements of phase velocity: Cross-validation of ambient-noise and earthquake-based observations". In: *Geophysical Journal International* 207.3, pp. 1493–1512. ISSN: 1365246X. DOI: 10.1093/gji/ggw341.

Knight, K.B., S. Nomade, P.R. Renne, A. Marzoli, H. Bertrand, and N. Youbi (2004). "The Central Atlantic Magmatic Province at the Triassic–Jurassic boundary: paleomagnetic and 40Ar/39Ar evidence from Morocco for brief, episodic volcanism". In: *Earth and Planetary Science Letters* 228.1-2, pp. 143–160. ISSN: 0012821X. DOI: 10.1016/j.epsl.2004.09.022. URL: https://linkinghub.elsevier.com/retrieve/pii/S0012821X04005667.

KNMI (2006). *Caribbean Netherlands Seismic Network*. DOI: 10.21944/DFFA7A3F-7E3A-3B33-A436-516A01B6AF3F. URL: http://rdsa.knmi.nl/network/NA/.

Knopoff, L. (1964). “A matrix method for elastic wave problems”. In: *Bulletin of the Seismological Society of America* 54.1, pp. 431–438. ISSN: 1943-3573. DOI: 10.1785/BSSA0540010431. URL: https://pubs.geoscienceworld.org/bssa/article/54/1/431/101455/A-matrix-method-for-elastic-wave-problems.

Köhler, Andreas, Christian Weidle, and Valérie Maupin (2012). “Crustal and uppermost mantle structure of southern Norway: results from surface wave analysis of ambient seismic noise and earthquake data”. In: *Geophysical Journal International* 191.3, pp. 1441–1456. ISSN: 0956540X. DOI: 10.1111/j.1365-246X.2012.05698.x. URL: https://academic.oup.com/gji/article-lookup/doi/10.1111/j.1365-246X.2012.05698.x.

Konrad Steffen and Daniel McGrath (2008). *IPY: Stability of Larsen C Ice Shelf in a Warming Climate*. DOI: 10.7914/SN/8A_2008. URL: https://www.fdsn.org/networks/detail/8A{_}2008/.

Krüger, F., F. Scherbaum, J. W. C. Rosa, R. Kind, F. Zetsche, and J. Höhne (2002). “Crustal and upper mantle structure in the Amazon region (Brazil) determined with broadband mobile stations”. In: *Journal of Geophysical Research: Solid Earth* 107.B10. ISSN: 0148-0227. DOI: 10.1029/2001JB000598. URL: https://agupubs.onlinelibrary.wiley.com/doi/10.1029/2001JB000598.

Kulesh, Michail A., Mamadou Sanou Diallo, and M. Holschneider (2005). “Wavelet analysis of ellipticity, dispersion and dissipation properties of Rayleigh waves”. In: *Acoustical Physics* 51.4, pp. 425–434.

Lara Wagner, Susan Beck, and Maureen Long (2010). *PerU Lithosphere and Slab Experiment*. DOI: 10.7914/SN/ZD_2010. URL: https://www.fdsn.org/networks/detail/ZD{_}2010/.

Laske, G., G. Masters, Z. Ma, and M. Pasyanos (2013). “Update on CRUST1.0 - a 1-degree global model of Earth’s crust”. In: *Proceedings of the EGU General Assembly 2013 held 7-12 April 2013, Vienna, Austria, id. EGU2013-2658.*

Laske, Gabi, Amanda Markee, John A. Orcutt, Cecily J. Wolfe, John A. Collins, Sean C. Solomon, Robert S. Detrick, David Bercovici, and Erik H. Hauri (2011). “Asymmetric shallow mantle structure beneath the Hawaiian Swell-evidence from Rayleigh waves recorded by the PLUME network”. In: *Geophysical Journal International* 187.3, pp. 1725–1742. ISSN: 0956540X. DOI: 10.1111/j.1365-246X.2011.05238.x. URL: https://academic.oup.com/gji/article-lookup/doi/10.1111/j.1365-246X.2011.05238.x.

Lebedev, Sergei and Rob D. van der Hilst (2008). “Global upper-mantle tomography with the automated multimode inversion of surface and S -wave forms”. In: *Geophysical Journal International* 173.2, pp. 505–518. ISSN: 0956540X. DOI: 10.1111/j.1365-246X.2008.03721.x. URL: https://academic.oup.com/gji/article-lookup/doi/10.1111/j.1365-246X.2008.03721.x.

Lebedev, Sergei, Thomas Meier, and Rob D. van der Hilst (2006). “Asthenospheric flow and origin of volcanism in the Baikal Rift area”. In: *Earth and Planetary Science Letters* 249.3-4, pp. 415–424. ISSN: 0012821X. DOI: 10.1016/j.epsl.2006.07.007. URL: https://linkinghub.elsevier.com/retrieve/pii/S0012821X06004985.

Lee, Suzan van der, David James, and Paul Silver (2001). “Upper mantle S velocity structure of central and western South America”. In: *Journal of Geophysical Research: Solid Earth* 106.B12, pp. 30821–30834. ISSN: 0148-0227. DOI: 10.1029/2001JB000338. URL: https://agupubs.onlinelibrary.wiley.com/doi/10.1029/2001JB000338.

Legendre, Cédric P., Li Zhao, and Tai-Lin Tseng (2021). “Large-scale variation in seismic anisotropy in the crust and upper mantle beneath Anatolia, Turkey”. In: *Communications Earth and Environment* 2.1, p. 73. ISSN: 2662-4435. DOI: 10.1038/s43247-021-00142-6. URL: https://www.nature.com/articles/s43247-021-00142-6.

Levshin, A. L., T. B. Yanovskaya, A. V. Lander, B. G. Bukchin, M. P. Barmin, L. I. Ratnikova, and E. N. Its (1989). *Seismic Surface Waves in a Laterally Inhomogeneous Earth*. Ed. by V. I. Keilis-Borok. Kluwer Academic Publishers.

Levshin, Anatoli L, Michael H Ritzwoller, and Joe S Resovsky (1999). "Source effects on surface wave group travel times and group velocity maps". In: *Physics of the Earth and Planetary Interiors* 115.3-4, pp. 293–312. ISSN: 00319201. DOI: 10.1016/S0031-9201(99)00113-2. URL: https://linkinghub.elsevier.com/retrieve/pii/S0031920199001132.

Long, Maureen D. and Paul G. Silver (2008). "The Subduction Zone Flow Field from Seismic Anisotropy: A Global View". In: *Science* 319.5861, pp. 315–318. ISSN: 0036-8075. DOI: 10.1126/science.1150809. URL: https://www.science.org/doi/10.1126/science.1150809.

Magrini, Fabrizio, Giovanni Diaferia, Lapo Boschi, and Fabio Cammarano (2020). "Arrival-angle effects on two-receiver measurements of phase velocity". In: *Geophysical Journal International* 220.3, pp. 1838–1844. ISSN: 0956-540X. DOI: 10.1093/gji/ggz560. URL: https://academic.oup.com/gji/article/220/3/1838/5672636.

Magrini, Fabrizio, Giovanni Diaferia, Amr El-Sharkawy, Fabio Cammarano, Mark van der Meijde, Thomas Meier, and Lapo Boschi (2022). "Surface-Wave Tomography of the Central-Western Mediterranean: New Insights Into the Liguro-Provençal and Tyrrhenian Basins". In: *Journal of Geophysical Research: Solid Earth* 127.3, pp. 1–23. ISSN: 21699356. DOI: 10.1029/2021JB023267.

Mantovani, M.S.M., M.C.L. Quintas, W. Shukowsky, and B.B. Brito Neves (2005). "Delimitation of the Paranapanema Proterozoic block: A geophysical contribution". In: *Episodes* 28.1, pp. 18–22. ISSN: 0705-3797. DOI: 10.18814/epiiugs/2005/v28i1/002. URL: http://www.episodes.org/journal/view.html?doi=10.18814/epiiugs/2005/v28i1/002.

Marcelo Sousa de Assumpção and Marcelo Belentani de Bianchi (2016). *Pantanal, Chaco and Paraná (PCPB) structural studies network*. DOI: 10.7914/8SCF-YD39. URL: https://www.fdsn.org/networks/detail/XC{_}2016/.

Marzoli, Andrea, Callegaro Sara, Dal Corso Jacopo, Joshua HFL Davies, Massimo Chiaradia, Nassrrdine Youbi, Hervé Bertrand, Laurie Reisberg, Renaud Merle, and Fred Jourdan (2018). "The Central Atlantic magmatic province (CAMP): A review". In: *The Late Triassic World: Earth in a time of transition*, pp. 91–125.

MASE Caltech (2007). *Meso America Subduction Experiment*. DOI: 10.7909/C3RN35SP. URL: http://www.gps.caltech.edu/{~}clay/MexWeb/MexSubduction.html.

Masy, J., F. Niu, and A. Levander (2009). "Seismic anisotropy and mantle flow beneath western Venezuela". In: *American Geophysical Union Fall Meeting 2009*, paper T53A–1554.

Matt Pritchard (2009). *The life cycle of Andean volcanoes:Combining space-based and field studies*. DOI: 10.7914/SN/YS_2009. URL: https://www.fdsn.org/networks/detail/YS{_}2009/.

Meier, T., K. Dietrich, B. Stöckhert, and H. P. Harjes (2004). "One-dimensional models of shear wave velocity for the eastern Mediterranean obtained from the inversion of Rayleigh wave phase velocities and tectonic implications". In: *Geophysical Journal International* 156.1, pp. 45–58. ISSN: 0956540X. DOI: 10.1111/j.1365-246X.2004.02121.x.

Melo, Bruna Chagas, Marcelo Assumpção, Felipe Neves, Luís Galhardo, José Roberto Barbosa, Cleusa Barbosa, Bruno Collaço, Jackson Calhau, Marcelo Bianchi, Emilia Brasilio, Paulo Azevedo, Marcelo Rocha, Tiago Silva, Edna Facincani, Gonzalo Fernandez, Felipe Condori, Gerardo Sánchez, Luis Andujar, Rafael Fugarazzo, Moisés Gadea, Vincent Figueres, Leda Sánchez, Enrique Latorres, Hernán Castro, Martín Rodríguez, and Anahí Curbelo (2018). "Mantle anisotropy and asthenospheric flow around cratons in southeastern South America". In: *Geophysical Journal International* 215.1, pp. 494–506. ISSN: 1365246X. DOI: 10.1093/gji/ggy288.

Michael West and Douglas Christensen (2010). *Investigating the relationship between pluton growth and volcanism at two active intrusions in the central Andes*. DOI: 10.7914/SN/XP_2010. URL: https://www.fdsn.org/networks/detail/XP{_}2010/.

Moraes, P. and M Assumpção (2022). "Estrutura rasa da Bacia do Pantanal com função do receptor, dispersão de ondas superficiais e curva H/V". In: *Master's dissertation.* URL: https://www.teses.usp.br/teses/disponiveis/14/14132/tde-26042022-204518/en.php.

Moura, Denise S., André V.S. Nascimento, Carlos A.M. Chaves, Yára R. Marangoni, and George S. França (2024). "Lithospheric structure of the Paraná, Chaco-Paraná, and Pantanal basins: Insights from ambient noise and earthquake-based surface wave tomography". In: *Journal of South American Earth Sciences* 145, p. 105048. ISSN: 08959811. DOI: 10.1016/j.jsames.2024.105048. URL: https://linkinghub.elsevier.com/retrieve/pii/S0895981124002700.

Mueller, Michael C. (1991). "Prediction of lateral variability in fracture intensity using multicomponent shear-wave surface seismic as a precursor to horizontal drilling in the Austin Chalk". In: *Geophysical Journal International* 107.3, pp. 409–415. ISSN: 0956540X. DOI: 10.1111/j.1365-246X.1991.tb01402.x. URL: https://academic.oup.com/gji/article-lookup/doi/10.1111/j.1365-246X.1991.tb01402.x.

Muyzert, Everhard and Roel Snieder (1996). "The influence of errors in source parameters on phase velocity measurements of surface waves". In: *Bulletin of the Seismological Society of America* 86.6, pp. 1863–1872. ISSN: 1943-3573. DOI: 10.1785/BSSA0860061863. URL: https://pubs.geoscienceworld.org/bssa/article/86/6/1863/102663/The-influence-of-errors-in-source-parameters-on.

Nascimento, André Vinícius De Sousa, George Sand França, Carlos Alberto Moreno Chaves, and Giuliano Sant Anna Marotta (2022). "Rayleigh wave group velocity maps at periods of 10-150 s beneath South America". In: *Geophysical Journal International* 228.2, pp. 958–981. ISSN: 1365246X. DOI: 10.1093/gji/ggab363.

Nascimento, André V.S., George S. França, Carlos A.M. Chaves, Giuliano S. Marotta, and Marcelo Assumpção (2024). "Unraveling Precambrian cratonic roots beneath South America: A contribution from surface wave tomography". In: *Tectonophysics* 883, p. 230392.

ISSN: 00401951. DOI: 10.1016/j.tecto.2024.230392. URL: https://linkinghub.elsevier.com/retrieve/pii/S004019512400194X.

National Centre for Seismological Research (CENAIS Cuba) (1998). *Servicio Sismologico Nacional de Cuba*. DOI: 10.7914/SN/CW. URL: https://www.fdsn.org/networks/detail/CW/.

National Seismological Centre (1998). *Centro Nacional de Sismologia*. DOI: 10.7914/SN/DR. URL: https://www.fdsn.org/networks/detail/DR/.

Natural Resources Canada (1975). *Canadian National Seismograph Network*. DOI: 10.7914/SN/CN. URL: https://www.fdsn.org/networks/detail/CN/.

Observatório Nacional, Rio de Janeiro, RJ (2011). *Rede Sismográfica do Sul e do Sudeste*. DOI: 10.7914/SN/ON. URL: https://www.fdsn.org/networks/detail/ON/.

O'Connor, John M. and Robert A. Duncan (1990). "Evolution of the Walvis Ridge-Rio Grande Rise Hot Spot System: Implications for African and South American Plate motions over plumes". In: *Journal of Geophysical Research: Solid Earth* 95.B11, pp. 17475–17502. ISSN: 0148-0227. DOI: 10.1029/JB095iB11p17475. URL: https://agupubs.onlinelibrary.wiley.com/doi/10.1029/JB095iB11p17475.

Paige, C.C. and M.A Saunders (1982). "LSQR: An algorithm for sparse linear equations and sparse least squares". In: *Transactions on Mathematical Software* 8.1, pp. 43–71.

Penn State University (2004). *AfricaArray*. DOI: 10.7914/SN/AF. URL: https://www.fdsn.org/networks/detail/AF/.

Piñero-Feliciangeli, L.T. and J.-M. Kendall (2008). "Sub-slab mantle flow parallel to the Caribbean plate boundaries: Inferences from SKS splitting". In: *Tectonophysics* 462.1-4, pp. 22–34. ISSN: 00401951. DOI: 10.1016/j.tecto.2008.01.022. URL: https://linkinghub.elsevier.com/retrieve/pii/S0040195108003569.

Polet, J., P. G. Silver, S. Beck, T. Wallace, G. Zandt, S. Ruppert, R. Kind, and A. Rudloff (2000). "Shear wave anisotropy beneath the Andes from the BANJO, SEDA, and PISCO experiments". In: *Journal of Geophysical Research: Solid Earth* 105.B3, pp. 6287–6304.

ISSN: 0148-0227. DOI: 10.1029/1999JB900326. URL: https://agupubs.onlinelibrary.wiley.com/doi/10.1029/1999JB900326.

Poveda, Esteban, Gaspar Monsalve, Jordi Julià, and Patricia Pedraza (2023). "Radial and azimuthal seismic anisotropy in NW South America: Insights into crustal deformation and mantle flow using ambient noise and surface wave tomography". In: *Journal of South American Earth Sciences* 131, p. 104606. ISSN: 08959811. DOI: 10.1016/j.jsames.2023.104606. URL: https://linkinghub.elsevier.com/retrieve/pii/S0895981123004182.

Priestley, Keith, Dan McKenzie, and Tak Ho (2018). "A Lithosphere–Asthenosphere Boundary—a Global Model Derived from Multimode Surface-Wave Tomography and Petrology". In: pp. 111–123. DOI: 10.1002/9781119249740.ch6. URL: https://agupubs.onlinelibrary.wiley.com/doi/10.1002/9781119249740.ch6.

Ramos, Victor A. (2008). "Patagonia: A paleozoic continent adrift?" In: *Journal of South American Earth Sciences* 26.3, pp. 235–251. ISSN: 08959811. DOI: 10.1016/j.jsames.2008.06.002. URL: https://linkinghub.elsevier.com/retrieve/pii/S0895981108000527.

Ray Russo (2004). *Studies of crust and upper mantle structure, mantle flow and geodynamics of the Chile Ridge subduction zone*. DOI: 10.7914/SN/YJ_2004. URL: https://www.fdsn.org/networks/detail/YJ{_}2004/.

Ray Russo (2007). *Studies of crust and upper mantle structure, mantle flow and geodynamics of the Chile Ridge subduction zone*. DOI: 10.7914/SN/Y3_2007. URL: https://www.fdsn.org/networks/detail/Y3{_}2007/.

Renne, Paul R., Katja Deckart, Marcia Ernesto, Gilbert Fe´raud, and Enzo M. Piccirillo (1996). "Age of the Ponta Grossa dike swarm (Brazil), and implications to Parana´flood volcanism". In: *Earth and Planetary Science Letters* 144.1-2, pp. 199–211. ISSN: 0012821X. DOI: 10.1016/0012-821X(96)00155-0. URL: https://linkinghub.elsevier.com/retrieve/pii/0012821X96001550.

Rivadeneyra-Vera, Carolina, Marcelo Bianchi, Marcelo Assumpção, Victoria Cedraz, Jordi Julià, Martín Rodríguez, Leda Sánchez, Gerardo Sánchez, Luciana Lopez-Murua, Gonzalo Fernandez, and Rafael Fugarazzo (2019). “An Updated Crustal Thickness Map of Central South America Based on Receiver Function Measurements in the Region of the Chaco, Pantanal, and Paraná Basins, Southwestern Brazil”. In: *Journal of Geophysical Research: Solid Earth* 124.8, pp. 8491–8505. ISSN: 2169-9313. DOI: 10.1029/2018JB016811. URL: https://onlinelibrary.wiley.com/doi/10.1029/2018JB016811.

Rocha, M. P., M. Assumpção, G. M. P. C. Affonso, P. A. Azevedo, and M. Bianchi (2019). “Teleseismic P-wave Tomography Beneath the Pantanal, Paraná and ChacoParaná Basins, SE South America: Delimiting Lithospheric Blocks of the SW Gondwana Assemblage”. In: *American Geophysical Union*. DOI: 10.1029/2018JB016807.

Rocha, Marcelo Peres, Paulo Araújo de Azevedo, Giuliano Sant’Anna Marotta, Martin Schimmel, and Reinhardt Fuck (2016). “Causes of intraplate seismicity in central Brazil from travel time seismic tomography”. In: *Tectonophysics* 680, pp. 1–7. ISSN: 00401951. DOI: 10.1016/j.tecto.2016.05.005. URL: https://linkinghub.elsevier.com/retrieve/pii/S0040195116301214.

Rocha, Marcelo Peres, Martin Schimmel, and Marcelo Assumpção (2011). “Upper-mantle seismic structure beneath SE and Central Brazil from P- and S-wave regional traveltime tomography”. In: *Geophysical Journal International* 184.1, pp. 268–286. ISSN: 0956540X. DOI: 10.1111/j.1365-246X.2010.04831.x. URL: https://academic.oup.com/gji/article-lookup/doi/10.1111/j.1365-246X.2010.04831.x.

Rosa, María Laura, Bruno Collaço, Marcelo Assumpção, Nora Sabbione, and Gerardo Sánchez (2016). “Thin crust beneath the Chaco-Paraná Basin by surface-wave tomography”. In: *Journal of South American Earth Sciences* 66, pp. 1–14. ISSN: 08959811. DOI: 10.1016/j.jsames.2015.11.010.

Russo, R. M. and P. G. Silver (1994). “Trench-Parallel Flow Beneath the Nazca Plate from Seismic Anisotropy”. In: *Science* 263.5150, pp. 1105–1111. ISSN: 0036-8075. DOI: 10.1126/science.263.5150.1105. URL: https://www.science.org/doi/10.1126/science.263.5150.1105.

Santos, João Orestes Schneider, Léo Afraneo Hartmann, Henri Eugene Gaudette, David Ian Groves, Neal Jesse Mcnaughton, and Ian Robert Fletcher (2000). "A New Understanding of the Provinces of the Amazon Craton Based on Integration of Field Mapping and U-Pb and Sm-Nd Geochronology". In: *Gondwana Research* 3.4, pp. 453–488. ISSN: 1342937X. DOI: 10.1016/S1342-937X(05)70755-3. URL: https://linkinghub.elsevier.com/retrieve/pii/S1342937X05707553.

Santos, J.O.S., L.A. Hartmann, M.S.G Faria, S.R.L. Riker, M.M. Souza, M.E. Almdeida, and N.J. Mcnaughton (2006). "A compartimentação do Cráton Amazonas em províncias: avanços ocorridos no período de 2000–2006". In: *SBG-Núcleo Norte, Simp. Geol. Amaz.* 9, CD–ROM.

Schaeffer, A. J. and S. Lebedev (2013). "Global shear speed structure of the upper mantle and transition zone". In: *Geophysical Journal International* 194.1, pp. 417–449. ISSN: 0956-540X. DOI: 10.1093/gji/ggt095. URL: https://academic.oup.com/gji/article-lookup/doi/10.1093/gji/ggt095.

Schaeffer, A.J., S. Lebedev, and T.W. Becker (2016). "Azimuthal seismic anisotropy in the Earth's upper mantle and the thickness of tectonic plates". In: *Geophysical Journal International* 207.2, pp. 901–933. ISSN: 0956-540X. DOI: 10.1093/gji/ggw309. URL: https://academic.oup.com/gji/article-lookup/doi/10.1093/gji/ggw309.

Schimmel, M., M. Assumpção, and J. C. VanDecar (2003). "Seismic velocity anomalies beneath SE Brazil from P and S wave travel time inversions". In: *Journal of Geophysical Research: Solid Earth* 108.B4. ISSN: 0148-0227. DOI: 10.1029/2001JB000187. URL: https://agupubs.onlinelibrary.wiley.com/doi/10.1029/2001JB000187.

Schwab, F.A. and L. Knopoff (1972). "Fast Surface Wave and Free Mode Computations". In: pp. 87–180. DOI: 10.1016/B978-0-12-460811-5.50008-8. URL: https://linkinghub.elsevier.com/retrieve/pii/B9780124608115500088.

Scripps Institution of Oceanography (1986). *Global Seismograph Network - IRIS/IDA*. DOI: 10.7914/SN/II. URL: https://www.fdsn.org/networks/detail/II/.

Servicio Geológico Colombiano (1993). *Red Sismologica Nacional de Colombia*. DOI: 10.7914/SN/CM. URL: https://www.fdsn.org/networks/detail/CM/.

Shirzad, T., M. Assumpção, and M. Bianchi (2020). "Ambient seismic noise tomography in west-central and Southern Brazil, characterizing the crustal structure of the Chaco-Paraná, Pantanal and Paraná basins". In: *Geophysical Journal International* 220.3, pp. 2074–2085.

Shirzad, Taghi, Marcelo Assumpção, Eric Debayle, Marcelo Bianchi, Bruno Collaço, Jackson Calhau, Gabriel N. Dragone, and Carlos Alberto Moreno Chaves (2024). "Crustal and Uppermost Mantle Azimuthal Anisotropy beneath West and SE Brazil using Ambient Seismic Noise". In: *Tectonophysics* 886, p. 230436. ISSN: 00401951. DOI: 10.1016/j.tecto.2024.230436. URL: https://linkinghub.elsevier.com/retrieve/pii/S0040195124002385.

Silver, Paul, Susan Beck, and Terry Wallace (1994). "BBand Andean Joint Exp. / Seismic Exploration of Deep Andes [Data set]". In: *International Federation of Digital Seismograph Networks*. DOI: https://doi.org/10.7914/SN/XE_1994.

Silver, Paul G. (1996). "SEISMIC ANISOTROPY BENEATH THE CONTINENTS: Probing the Depths of Geology". In: *Annual Review of Earth and Planetary Sciences* 24.1, pp. 385–432. ISSN: 0084-6597. DOI: 10.1146/annurev.earth.24.1.385. URL: https://www.annualreviews.org/doi/10.1146/annurev.earth.24.1.385.

Silver, Paul G. and W. Winston Chan (1991). "Shear wave splitting and subcontinental mantle deformation". In: *Journal of Geophysical Research: Solid Earth* 96.B10, pp. 16429–16454. ISSN: 0148-0227. DOI: 10.1029/91JB00899. URL: https://agupubs.onlinelibrary.wiley.com/doi/10.1029/91JB00899.

Smith, Martin L. and F. A. Dahlen (1973). "The azimuthal dependence of Love and Rayleigh wave propagation in a slightly anisotropic medium". In: *Journal of Geophysical Research* 78.17, pp. 3321–3333. ISSN: 01480227. DOI: 10.1029/JB078i017p03321. URL: http://doi.wiley.com/10.1029/JB078i017p03321.

Snoke, J. Arthur and David E. James (1997). “Lithospheric structure of the Chaco and Paraná Basins of South America from surface-wave inversion”. In: *Journal of Geophysical Research: Solid Earth* 102.B2, pp. 2939–2951. ISSN: 0148-0227. DOI: 10.1029/96JB03180. URL: https://agupubs.onlinelibrary.wiley.com/doi/10.1029/96JB03180.

Soomro, R. A., C. Weidle, L. Cristiano, S. Lebedev, T. Meier, M. Wilde-Piórko, W. Geissler, J. Plomerová, M. Grad, V. Babuška, E. Brückl, J. Čyžiene, W. Czuba, R. England, E. Gaczyński, R. Gazdova, S. Gregersen, A. Guterch, W. Hanka, E. Hegedus, B. Heuer, P. Jedlička, J. Lazauskiene, G. Randy Keller, R. Kind, K. Klinge, P. Kolinsky, K. Komminaho, E. Kozlovskaya, F. Krüger, T. Larsen, M. Majdański, J. Málek, G. Motuza, O. Novotný, R. Pietrasiak, Th Plenefisch, B. Råužek, S. Sliaupa, P. Środa, M. Świeczak, T. Tiira, P. Voss, and P. Wiejacz (2016). “Phase velocities of Rayleigh and Love waves in central and northern Europe from automated, broad-band, interstation measurements”. In: *Geophysical Journal International* 204.1, pp. 517–534. ISSN: 1365246X. DOI: 10.1093/gji/ggv462.

Susan Beck and George Zandt (2007). *Lithospheric Structure and Deformation of the Flat Slab Region of Argentina*. DOI: 10.7914/SN/ZL_2007. URL: https://www.fdsn.org/networks/detail/ZL{_}2007/.

Susan Beck, George Zandt, and Lara Wagner (2010). *Central Andean Uplift and the Geodynamics of the High Topography*. DOI: 10.7914/SN/ZG_2010. URL: https://www.fdsn.org/networks/detail/ZG{_}2010/.

Susan Beck, Terry Wallace, and George Zandt (2000). *Slab Geometry in the Southern Andes*. DOI: 10.7914/SN/YC_2000. URL: https://www.fdsn.org/networks/detail/YC{_}2000/.

Tassinari, Colombo C.G. and Moacir J.B. Macambira (1999). “Geochronological provinces of the Amazonian Craton”. In: *Episodes* 22.3, pp. 174–182. ISSN: 0705-3797. DOI: 10.18814/epiiugs/1999/v22i3/004. URL: http://www.episodes.org/journal/view.html?doi=10.18814/epiiugs/1999/v22i3/004.

Thiede, David S. and Paulo M. Vasconcelos (2010). “Paraná flood basalts: Rapid extrusion hypothesis confirmed by new 40Ar/39Ar results”. In: *Geology* 38.8, pp. 747–750. ISSN: 1943-2682. DOI: 10.1130/G30919.1. URL: http://pubs.geoscienceworld.org/geology/article/38/8/747/130356/Paran{\'{a}}-flood-basalts-Rapid-extrusion-hypothesis.

Timkó, M, L Wiesenberg, L Fodor, S Lebedev, T Meier, and Working Group (2022). “Crustal and upper mantle 3D Vs structure of the Pannonian Region from joint earthquake and ambient noise Rayleigh wave tomograpahy”. In: *in press*.

Turner, Simon, Marcel Regelous, Simon Kelley, Chris Hawkesworth, and Marta Mantovani (1994). “Magmatism and continental break-up in the South Atlantic: high precision40Ar-39Ar geochronology”. In: *Earth and Planetary Science Letters* 121.3-4, pp. 333–348. ISSN: 0012821X. DOI: 10.1016/0012-821X(94)90076-0. URL: https://linkinghub.elsevier.com/retrieve/pii/0012821X94900760.

Universidad de Chile (2012). *Red Sismologica Nacional*. DOI: 10.7914/SN/C1. URL: https://www.fdsn.org/networks/detail/C1/.

Universidade de Sao Paulo, USP (2017). *Vale SA Network*. DOI: 10.7914/SN/VL. URL: https://www.fdsn.org/networks/detail/VL/.

University of Puerto Rico (1986). *Puerto Rico Seismic Network & Puerto Rico Strong Motion Program*. DOI: 10.7914/SN/PR. URL: https://www.fdsn.org/networks/detail/PR/.

VanDecar, John C., David E. James, and M. Assumpção (1995). “Seismic evidence for a fossil mantle plume beneath South America and implications for plate driving forces”. In: *Nature* 378, pp. 25–31.

Vdovin, Oleg, José A. Rial, Anatoli L. Levshin, and Michael H. Ritzwoller (1999). “Group-velocity tomography of South America and the surrounding oceans”. In: *Geophysical Journal International* 136.2, pp. 324–340. ISSN: 0956540X. DOI: 10.1046/j.1365-246X.1999.00727.x. URL: https://academic.oup.com/gji/article/136/2/324/694089.

Vilotte, Jean-Pierre and RESIF (2011). *Seismic network XS:CHILE MAULE aftershock temporary experiment (RESIF-SISMOB)*. DOI: 10.15778/RESIF.XS2010. URL: https://seismology.resif.fr/networks/{\#}/XS{_}{_}2010.

Vinnik, L. P., L. I. Makeyeva, A. Milev, and A. Yu. Usenko (1992). "Global patterns of azimuthal anisotropy and deformations in the continental mantle". In: *Geophysical Journal International* 111.3, pp. 433–447. ISSN: 0956540X. DOI: 10.1111/j.1365-246X.1992.tb02102.x. URL: https://academic.oup.com/gji/article-lookup/doi/10.1111/j.1365-246X.1992.tb02102.x.

Vos, Denise de, Hanneke Paulssen, and Andreas Fichtner (2013). "Finite-frequency sensitivity kernels for two-station surface wave measurements". In: *Geophysical Journal International* 194.2, pp. 1042–1049. ISSN: 1365-246X. DOI: 10.1093/gji/ggt144. URL: http://academic.oup.com/gji/article/194/2/1042/599995/Finitefrequency-sensitivity-kernels-for-twostation.

Weston, J, E R Engdahl, J Harris, D Di Giacomo, and D A Storchak (2018). "ISC-EHB: reconstruction of a robust earthquake data set". In: *Geophysical Journal International* 214.1, pp. 474–484. ISSN: 0956-540X. DOI: 10.1093/gji/ggy155. URL: https://academic.oup.com/gji/article/214/1/474/4978439.

Weyler, G. (1962). *Projeto Pantanal: Final report of drill holes in the Pantanal Matogrossense.* Tech. rep. Petrobrás, Ponta Grossa, Brazil, p. 27.

Wiesenberg, L., C. Weidle, A. El-Sharkawy, M. Timkó, S. Lebedev, and T. Meier (2022). "Measuring the phase of ambient noise cross correlations: anisotropic Rayleigh and Love wave tomography across the Oman Mountains". In: *Geophysical Journal International* 231.2, pp. 1233–1251. ISSN: 1365246X. DOI: 10.1093/gji/ggac232.

Wilken, D. and W. Rabbel (2012). "On the application of Particle Swarm Optimization strategies on Scholte-wave inversion". In: *Geophysical Journal International* 190.1, pp. 580–594. ISSN: 0956540X. DOI: 10.1111/j.1365-246X.2012.05500.x.

Yao, H, R. D. van der Hilst, and M. V. de Hoop (2006). "Surface-wave array tomography in SE Tibet from ambient seismic noise and two-station analysis - I. Phase velocity maps". In: *Geophysical Journal International* 166.2, pp. 732–744. ISSN: 0956540X. DOI: 10.1111/j.1365-246X.2006.03028.x.

Zhang, X., H. Paulssen, S. Lebedev, and T. Meier (2009). "3D shear velocity structure beneath the Gulf of California from Rayleigh wave dispersion". In: *Earth and Planetary Science Letters* 279.3-4, pp. 255–262. ISSN: 0012821X. DOI: 10.1016/j.epsl.2009.01.003. URL: https://linkinghub.elsevier.com/retrieve/pii/S0012821X09000132.

Zhou, Longquan, Jiayi Xie, Weisen Shen, Yong Zheng, Yingjie Yang, Haixia Shi, and Michael H. Ritzwoller (2012). "The structure of the crust and uppermost mantle beneath South China from ambient noise and earthquake tomography". In: *Geophysical Journal International* 189.3, pp. 1565–1583. ISSN: 0956540X. DOI: 10.1111/j.1365-246X.2012.05423.x. URL: https://academic.oup.com/gji/article-lookup/doi/10.1111/j.1365-246X.2012.05423.x.